

# MOVPE growth of InN and InGaN with different surface orientations

vorgelegt von  
Master of Science in Nano-wissenschaft und -technologie

Duc V. Dinh

aus Thai Binh, Vietnam

Von der Fakultät II - Mathematik und Naturwissenschaften

der Technischen Universität Berlin

zur Erlangung des akademischen Grades

Doktor der Naturwissenschaften

Dr. rer. nat.

genehmigte Dissertation

Promotionsausschuss:

Vorsitzender: Prof. Dr. Michael Lehmann

Berichter/Gutachter: Prof. Dr. Nicolas Grandjean

Berichter/Gutachter: Prof. Dr. Michael Kneissl

Tag der wissenschaftlichen Aussprache: 12 September 2012

Berlin - 2012

- D 83 -

**Parts of this work have been already published:**

Duc V. Dinh, M. Pristovsek, R. Kremzow, and M. Kneissl, “Growth of semipolar  $(10\bar{1}\bar{3})$  InN on  $m$ -plane sapphire using metal-organic vapor phase epitaxy”, [physica status solidi - rapid research letters](#) **4**, 127 (2010).

Duc V. Dinh, M. Pristovsek, S. Solopow, D. Skuridina, and M. Kneissl, “Comparison study of  $N$ - and  $In$ -polar  $\{0001\}$  InN layers grown by MOVPE”, [physica status solidi \(c\)](#) **9**, 977 (2012).

S. Ploch, T. Wernicke, Duc V. Dinh, M. Pristovsek, and M. Kneissl, “Surface diffusion and layer morphology of  $(11\bar{2}2)$  GaN grown by metal-organic vapor phase epitaxy”, [Journal of Applied Physics](#) **111**, 033526 (2012).

Duc V. Dinh, D. Skuridina, S. Solopow, M. Frentrup, M. Pristovsek, P. Vogt, M. Kneissl, F. Ivaldi, S. Kret, and A. Szczepańska, “Growth and characterizations of semipolar  $(11\bar{2}2)$  InN”, [Journal of Applied Physics](#) **112**, 013530 (2012).

Duc V. Dinh, D. Skuridina, S. Solopow, M. Pristovsek, P. Vogt, and M. Kneissl, “Role of nitridation on the growth and the polarity of InN by metal-organic vapor phase epitaxy”, [Journal of Crystal Growth](#) (*submitted*).

Duc V. Dinh, S. Solopow, M. Pristovsek, and M. Kneissl, “Evolution of indium rich InGaN layers during direct growth on nitridated sapphire in metal-organic vapor phase epitaxy”, [Japanese Journal of Applied Physics](#) (*submitted*).

# Contents

<b>1</b>	<b>Introduction</b>	<b>1</b>
<b>2</b>	<b>Overview of material properties</b>	<b>5</b>
2.1	Structural properties of III-Nitrides . . . . .	5
2.2	Material properties of InN and related alloys . . . . .	9
2.2.1	Bandgap and electrical properties . . . . .	9
2.2.2	Surface electron accumulation . . . . .	10
<b>3</b>	<b>Heteroepitaxy of III-nitrides</b>	<b>13</b>
3.1	MOVPE growth process: General considerations . . . . .	14
3.2	Modes of layer growth . . . . .	17
3.3	Precursors for III-nitride epitaxy in MOVPE . . . . .	18
3.3.1	Group-III molecular sources . . . . .	19
3.3.2	Ammonia . . . . .	21
3.4	Substrates for III-nitride epitaxy . . . . .	22
3.4.1	Sapphire . . . . .	23
3.5	MOVPE setup and growth procedures . . . . .	26
3.5.1	<i>In-situ</i> monitoring by ellipsometry . . . . .	26
3.5.2	InN on sapphire . . . . .	27
3.5.3	InN on GaN templates . . . . .	29
<b>4</b>	<b>Sapphire nitridation</b>	<b>31</b>
4.1	Nitridation mechanism . . . . .	34
4.2	Nitridation in MOVPE . . . . .	35
4.2.1	<i>In-situ</i> monitoring of nitridation . . . . .	35
4.3	Surface properties of the nitridation layer . . . . .	37

4.4	Effects of nitridation on InN growth . . . . .	39
4.5	Chapter summary . . . . .	43
<b>5</b>	<b>Polar (0001) InN with N- and In-polarity</b>	<b>45</b>
5.1	Polarity determination . . . . .	45
5.1.1	KOH wet-etching . . . . .	46
5.1.2	Valence band emission in X-ray photoelectron spectroscopy . . .	47
5.2	Polarity control of InN by sapphire nitridation . . . . .	49
5.3	Comparisons of N- and In-polar InN . . . . .	54
5.3.1	Polarity . . . . .	54
5.3.2	Crystallinity . . . . .	55
5.3.3	Surface morphology and growth modes . . . . .	61
5.3.4	Optical properties . . . . .	67
5.4	Chapter summary . . . . .	71
<b>6</b>	<b>Semipolar (10<math>\bar{1}</math>3) InN</b>	<b>73</b>
6.1	Crystallinity and in-plane relationship . . . . .	73
6.2	Surface morphology and surface diffusion . . . . .	78
6.2.1	Effects of the nitridation on the surface morphology of InN . . .	80
6.2.2	Surface diffusion . . . . .	82
6.3	Optical properties . . . . .	84
6.4	Chapter summary . . . . .	86
<b>7</b>	<b>Semipolar (11<math>\bar{2}</math>2) InN</b>	<b>89</b>
7.1	<i>In-situ</i> growth monitoring . . . . .	89
7.2	Crystallinity and in-plane relationship . . . . .	91
7.3	Surface morphology and surface diffusion . . . . .	97
7.4	Defects and micro-structure . . . . .	102
7.5	Polarity . . . . .	106
7.6	Chapter summary . . . . .	108
<b>8</b>	<b>Polar (0001) In<sub>x</sub>Ga<sub>1-x</sub>N</b>	<b>109</b>
8.1	Effect of group-III input flow rate . . . . .	111
8.1.1	Crystalline properties . . . . .	111
8.1.2	Surface morphology and polarity determination . . . . .	116

## CONTENTS

---

8.2	Evolution of $\text{In}_{0.5}\text{Ga}_{0.5}\text{N}$ morphology and crystallinity . . . . .	117
8.3	Effect of growth temperature . . . . .	119
8.4	Chapter summary . . . . .	121
	<b>Summary</b>	<b>123</b>
	<b>Acknowledgments</b>	<b>127</b>
	<b>Bibliography</b>	<b>129</b>

## CONTENTS

---

# Chapter 1

## Introduction

The history of electric light began just about 130 years ago. In 1879, an American inventor, Thomas Edison, discovered that “giving a low current electricity runs through a metallic filament wire inner a vacuum environment could generate visible lights”. This invention has changed the world by establishing home-used electric lamps, the so-called incandescent light bulbs or filament lamps. Despite new development and creation filament lamps, they are still very similar to the early design. Their principle of black body radiation source requires about 95% of the electrical energy to be wasted by infrared light.

In the twentieth century, the first light-emitting diode (LED) was developed by a Russian, Oleg V. Losev [1] based on the discovery in 1907 of the British experimenter, Henry J. Round, about electro-luminescence [2]. In 1960, the first ruby laser diode (LD) was demonstrated by an American physicist, Theodore H. Maiman [3]. Shortly after the first practical semiconductor laser based on GaAs was demonstrated [4–12]. In 1962, the first practical visible-spectrum (red) LED based on GaAsP was developed by Nick Holonyak Jr. [6]. Rapid advances in science and technology with a strong hand-shake between research and application lead to the replacement of the light bulbs with the semiconductor-based LEDs. LEDs are nowadays broadly applied to areas such as LED-based television, LED-based traffic lights, and memory storage system. For example, different compact optical discs are used for media storage, such as CD disc (using a 780 nm wavelength laser diode), DVD disc (using a 650 nm wavelength), and Blu-ray disc (using a 405 nm wavelength). “Save energy” is a message throughout

---

the world today and LED-based light is one of the best solution for that. Their high efficiency drives the LED's revolution

Epitaxial thin-film growth techniques are the backbone of the developments of LEDs and opto-electronic devices. LEDs with different colors (emission wavelengths) covering the full range from ultra-violet to ultra-infrared have been realized by several different material-system-based LEDs such as phosphors (e.g., YAG:Ce), II-VI semiconductor compounds (like CdTe, CdS, and CdSe), silicon carbide (SiC), III-V semiconductor compounds (like GaAsP and InAsP), and III-Nitride semiconductor compounds (AlN, GaN, and InN).

Among the different material systems aforementioned, no efficient blue LED was available until 1994, when the first high-brightness blue LED based on InGaN was demonstrated by the Japanese scientist Shuji Nakamura [13]. Remarkable breakthroughs of the III-nitride-based devices have been achieved in the last 20 years, not only in high brightness red-blue-green-white LEDs and LDs but also in electronic devices such as high power and high frequency devices. It is clear that the nitride-based emitters will gradually replace the traditional home-used light bulbs.

Among the III-nitrides, the band-gap of InN was believed to be 1.9 eV [14, 15]. Only in 2002 it was discovered to be about 0.7 eV [16, 17], and now most people agree on the InN band-gap of 0.65 eV [18]. Thus III-nitrides and their ternary alloys (InGaN and InAlN) cover the spectral range from deep ultra-violet to visible and near infra-red regions by varying the indium contents of InGaN or InAlN alloys. In the recent 5 years, the lack of external efficiency of pure green LED and LD was a big focus of III-nitride research. Only in 2009, OSRAM and SORAA companies demonstrated green LD based on InGaN [19, 20]. Another idea is to apply III-nitrides to solar cells to absorb the spectrum of the whole sun by multi-junction quantum well solar cells [21, 22].

Most III-nitrides are grown on polar *c*-plane, especially commercial LEDs and LDs. To obtain higher efficiencies, research on III-nitrides based devices grown in other orientations such as semipolar and nonpolar has attracted much interest due to the reduction/suppression of built-in electrostatic fields in the polar direction [23]. The first LEDs on nonpolar GaN were made in 2004 [25] and semipolar in 2005 [26]. However, growth of semipolar and nonpolar III-nitrides is still challenging, limiting the performance of devices [27]. Free-standing semipolar and nonpolar GaN substrates are very

## Chapter 1. Introduction

---

expensive. Compared to GaN, growth of InN is even more challenging and its properties are less well-known. Furthermore, there is no free-standing bulk InN substrate. Due to those challenges, InN-based devices are still under basic research.

The growth procedure development for the high quality layers is not only critical for fundamental scientific studies but also for establishing devices. Obtaining higher growth rates of InN is one critical issue (up to now, just few hundred nanometer per hour growth rate is still a world record). Compared to GaN, most studies of InN are focused on *c*-plane (0001), only very little about growth and properties of InN with semi- and non-polar surface orientations are known.

Consequently, the aim of this work is to study the growth procedure and properties of InN and InGaN layers grown by MOVPE with different growth orientations. *In-situ* and *ex-situ* characterization techniques have been combined to investigate properties of InN.

The state of the art of InN and InGaN will be summarized in the two first chapters (Chapters 1 and 2). The experimental setup and MOVPE growth techniques will be described in Chapter 3. Nitridation process of sapphire substrates will be investigated in Chapter 4. The following chapters are related to the growth of different InN surface orientations, such as polar (0001) and (000 $\bar{1}$ ) InN (Chapter 5), semipolar (10 $\bar{1}$  $\bar{3}$ ) and (11 $\bar{2}$ 2) InN (Chapters 6 and 7). Chapter 8 will be related to growth and characterizations of (0001) In<sub>*x*</sub>Ga<sub>1-*x*</sub>N layers directly on sapphire.

---

## Chapter 2

# Overview of material properties

### 2.1 Structural properties of III-Nitrides

III-nitride semiconductor compounds (binary: AlN, GaN, and InN; and ternary: InAlN and InGaN) crystallize in either the wurtzite (hexagonal, 2H) or the zincblende (cubic, 3C) crystal structure (Fig. 2.1), each of them have different properties. The wurtzite phase is stable, and the zincblende phase is only metastable. Wurtzite structure consists of two embedded hexagonal atom stacks, noted as *A* and *B* stacks (Fig. 2.1). They stack on each other to form *ABABAB...* sequences along the [0001] direction, also called a *Hexagonal Closest Packings* (HCP). Cubic structure shows different stacking sequences, *ABCABC...*, as called a *Face Centered Cubic* (FCC). Figure 2.2 shows the unit cell model of the wurtzite III-nitride crystal structures. Table 2.1 shows the lattice constants of III-nitrides at room temperature. In this thesis, only the wurtzite crystal structure of III-nitrides is discussed.

All wurtzite III-nitrides have the same  $P6_3mc$  space group symmetry (Hermann-Mauguin notation). Thus, the structure of wurtzite III-nitrides is anisotropic, which results in the different properties in both directions, i.e., thermal and optical properties. The wurtzite structure has two different lattice constants,  $a_w$  and  $c_w$ , as shown in Table 2.1 and Fig. 2.2.

Generally, growth of III-nitrides is performed at high temperature on a homo-substrate or foreign substrate (e.g., sapphire). For example, growth of InN is usually performed at 500-600°C using metal-organic vapor phase epitaxy (MOVPE), and at 400-500°C using molecular beam epitaxy (MBE). For hetero-epitaxial growth, there

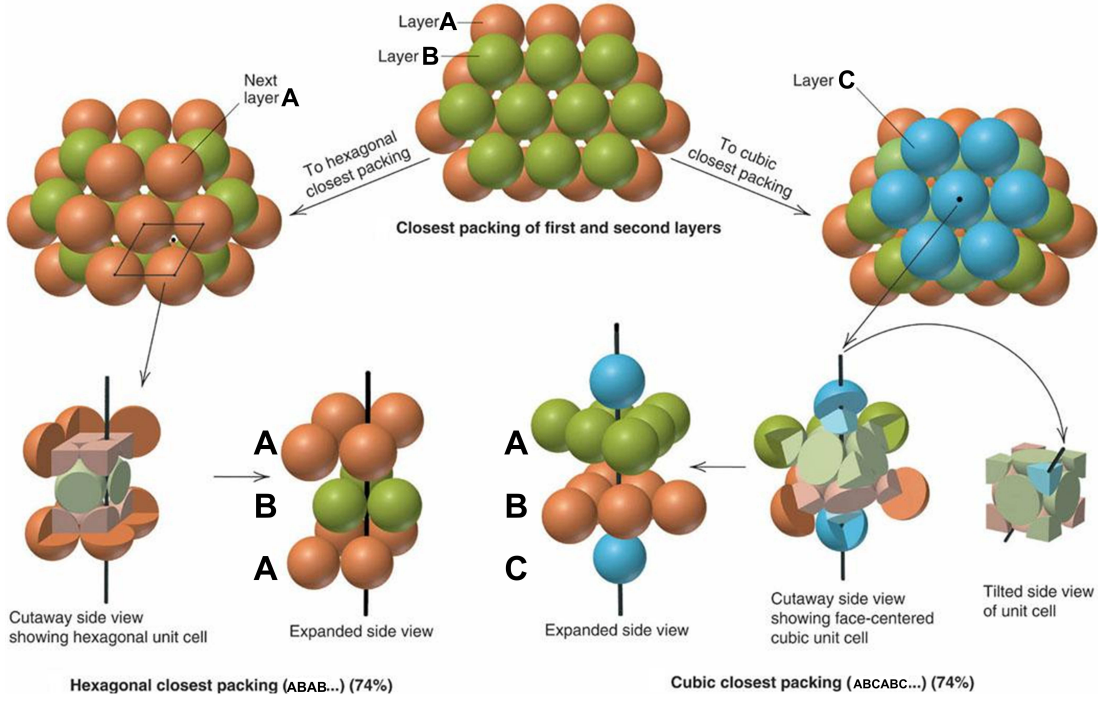


**Figure 2.1:** Atom stacks of hexagonal closest packing (HCP) and cubic closest packing (FCC) structures [28].

are always lattice and thermal expansion mismatches between layer and substrate (Table 2.2). Both must be taken into account to calculate the lattice mismatch at growth temperature since they strongly affect growth and quality of the epitaxial layers. Also during cooling process after growth, different thermal expansion coefficients lead to a strained layer.

To indicate the direction, axis, or planes of the wurtzite crystal structure, a modified Miller-Bravais notation  $\{hkil\}$  is employed, where  $i = -(h + k)$ . When  $h = k = i = 0$  and  $l = 1$ , then this (0001) plane is called a  $c$ -plane, and the perpendicular direction to this

Materials	Wurtzite		Zincblende
	$a_w$	$c_w$	$a_z$
AlN	3.112	4.982	4.360
GaN	3.189	5.186	4.500
InN	3.545	5.703	4.980

**Table 2.1:** Lattice constants at room temperature of III-nitrides with the different crystal structures [29].

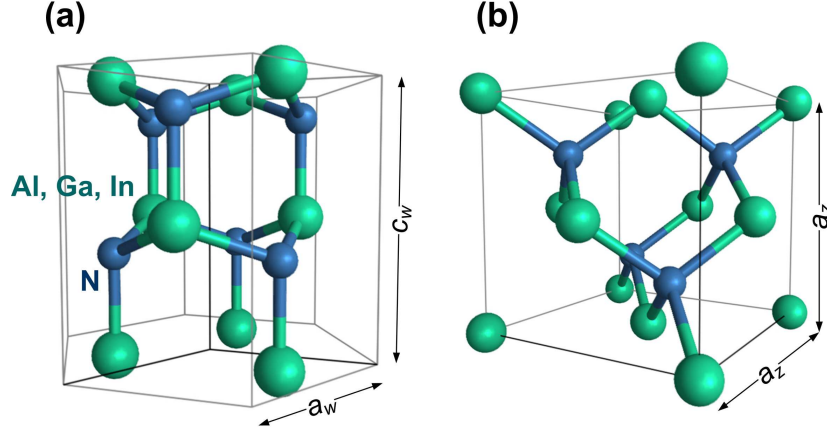


**Figure 2.2:** Unit cell of III-nitrides with (a) wurtzite and (b) zincblende crystal structures.

plane is called a  $c$ -direction ( $[0001]$ ) (Fig. 2.3).

“Polarity” is a term that indicates either nitrogen (N) or group-III (Al, Ga, or In) atoms lying at the topmost of the bare layer surface (i.e., a surface with the least number of broken bonds). “Polarity” term is also called “face”, e.g., group-III-polarity/face (Fig. 2.3(a)) or N-polarity/face (Fig. 2.3(b)). The polarity of III-nitrides grown on hetero-epitaxial substrate depends on growth technique and parameter. Polarity control of III-nitrides is an important issue, on which surface morphology, electrical and optical properties, as well as chemical and thermal stability of III-nitrides strongly depend. For instance, spontaneous polarization field is highest in the  $[000\bar{1}]$  direction, i.e., pointing from the group-III-face to the N-face shown in Fig. 2.3 [30]. Additionally, group-III-polar III-nitrides have higher chemical and thermal stability than N-polar III-nitrides.

The  $c$ -plane of III-nitrides is also called the “polar” plane. In contrast to the polar  $c$ -plane, other crystal planes are called non- and semi-polar planes (Fig. 2.4). It is

Materials	$\parallel a$ -axis ( $10^{-6} \text{ K}^{-1}$ )	$\parallel c$ -axis ( $10^{-6} \text{ K}^{-1}$ )
AlN [31]	4.15	5.27
GaN [31]	5.59	3.14
InN [32]	3.80	2.90
Sapphire [33]	5.22	5.92

**Table 2.2:** Thermal expansion coefficient parameters at room temperature of the wurtzite III-nitrides.

## 2.1. Structural properties of III-Nitrides

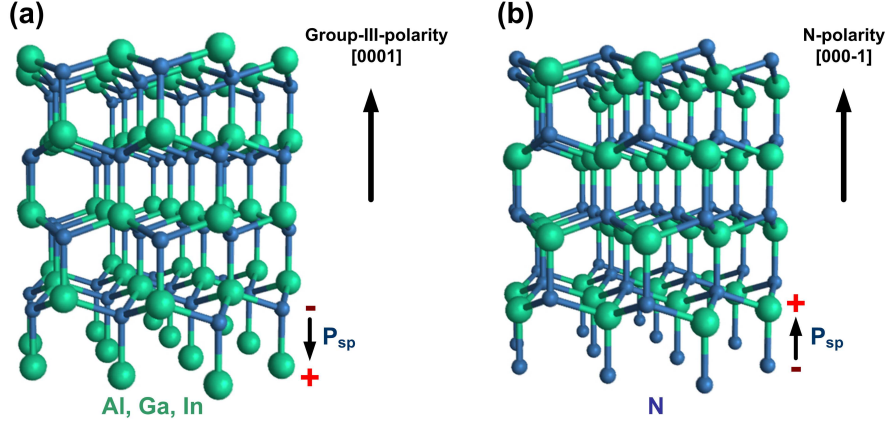


**Figure 2.3:** III-nitrides ( $2 \times 2 \times 2$  unit cells) with the different polarities: (a) group-III polarity (+ $c$ - or  $[0001]$  direction) and (b) N-polarity ( $-c$ - or  $[000\bar{1}]$  direction).  $P_{sp}$  vectors indicate the directions of the spontaneous piezoelectric field in both the polarities.

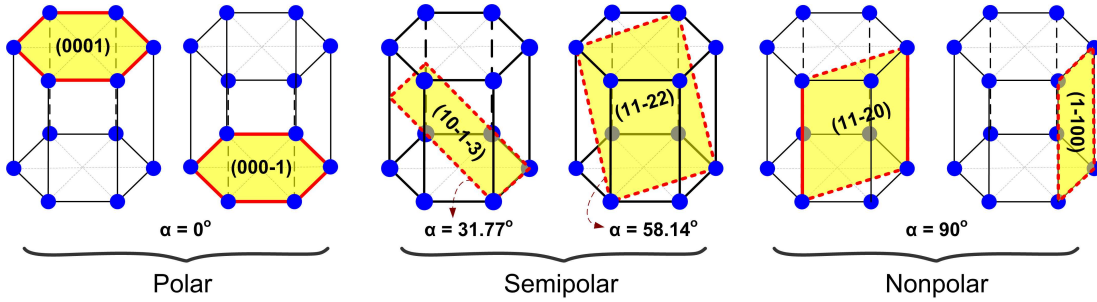


**Figure 2.4:** III-nitrides with different surface orientations. The  $\alpha$  angles were calculated for InN with respect to the  $c$ -plane InN ( $\alpha = 0^\circ$ ).

well-known that semi- and non-polar planes exhibit smaller spontaneous piezoelectric field along growth direction compared to  $c$ -plane [23]. A nonpolar plane corresponds to  $l = 0$ , e.g.,  $a$ -plane  $(11\bar{2}0)$  and  $m$ -plane  $(1\bar{1}00)$ . A nonpolar plane inclines  $90^\circ$  to the  $c$ -plane. Planes in between are called semipolar ( $h$  or  $k$  are nonzero, and  $l \neq 0$ ), e.g., semipolar  $(10\bar{1}3)$  and  $(11\bar{2}2)$  planes. A semipolar plane inclines between  $0$ - $90^\circ$  to the  $c$ -plane.

In contrast to the polar structure of III-nitrides, the semi- and non-polar structures have two-fold surface symmetry instead of the six-fold surface symmetry of the  $c$ -plane, which strongly affect their properties, i.e., morphological and structural properties. Growth of high quality semi- and non-polar III-nitrides is much more challenging than polar III-nitrides due to the hard control of the growth orientation and very high defect density in the layers.

## 2.2 Material properties of InN and related alloys

### 2.2.1 Bandgap and electrical properties

Among III-nitrides, InN has the smallest effective electron mass, leading to the highest mobility and the highest saturation velocity as shown in Table 2.3. The effective electron mass of InN [35] is 2 and 5 times smaller than those of GaN [36] and AlN [37], respectively. The peak drift velocity of InN is higher than GaN (30%) and AlN (60%) [37]. Furthermore, theoretical calculations of the electron transport characteristics of InN show a superior value compared to those of the other III-nitrides over a wide range of temperature (15 - 500 K) [42]. A model of the electron transport in bulk wurtzite InN was demonstrated to check the impact of the transient electron transport on the performance of proposed InN-based devices [43]. The model showed that InN-based devices would have an extremely high speed of the transient electron transport with a high cut-off frequency up to thousands of giga-hertz frequency (GHz), e.g., 2500 GHz, 130 GHz, and 10 GHz for 0.1  $\mu\text{m}$ , 1  $\mu\text{m}$ , and 10  $\mu\text{m}$  device thickness, respectively [43]. This makes InN very promisingly for high-speed and high-performance heterojunction field electron transistors (HFETs), which would operate at near tetra-hertz region (THz) [43, 44].

Varying In-content of In(Ga,Al)N gives a tunable bandgap energy of In(Ga,Al)N from 0.65 - 3.4 - 6.12 eV (near infrared (InN) over ultraviolet (GaN) to deep ultraviolet (AlN) region). Thus, In(Ga,Al)N can be applied not only for solid-state emitting devices but also for high efficiency energy conversion systems such as solar cells [21, 22].

Parameters	InN	GaN	AlN
Bandgap (eV)	0.65 [18]	3.4	6.12 [24]
Electron mass ( $\times m_0$ ) ( $m_0 = 9.1 \times 10^{-31}$ kg)	0.11 [35]	0.20 [36]	0.48 [37]
Peak drift velocity ( $\times 10^7$ cm/s)	4.2 [37]	2.9 [37]	1.7 [37]
Electron mobility ( $\text{cm}^2/\text{Vs}$ ) (theoretical)	4400 [38]	1000 [38]	300 [38]
Electron mobility ( $\text{cm}^2/\text{Vs}$ ) (experimental)	3500 [39]	900 [40]	50 [41]

**Table 2.3:** Material properties of III-nitrides at room temperature.

## 2.2. Material properties of InN and related alloys

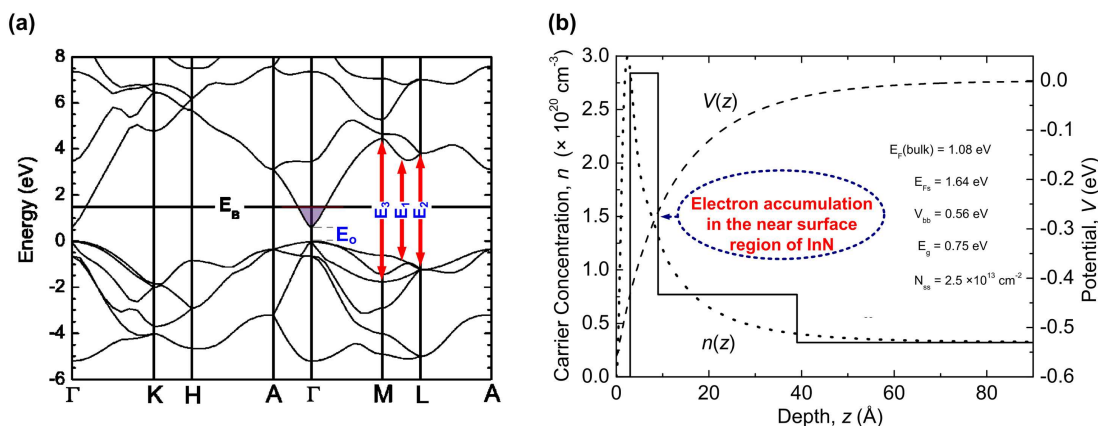


**Figure 2.5:** (a) The wurtzite InN energy band structure calculated using density functional theory within the local density approximation incorporating self-interaction corrections [46]. Conduction band minimum at the  $\Gamma$ -point is *much* lower with respect to the branch-point energy ( $E_B$ ) than the conduction band edge at other points in  $k$ -space. Critical points like  $E_0$ ,  $E_1$ ,  $E_2$ , and  $E_3$  are shown. (b) The layered charge profile used in the high-resolution electron-energy-loss spectroscopic simulations (solid line) and the corresponding smooth charge profile  $n(z)$  calculated by solving the Poisson equation within the modified Thomas-Fermi approximation (dotted line) [47]. A maximum electron density of  $\sim 2.8 \times 10^{20} \text{ cm}^{-3}$  and a bulk carrier concentration of  $3.2 \times 10^{19} \text{ cm}^{-3}$  occur in the near surface, indicating the presence of an intrinsic electron accumulation layer on the clean InN surface.

However, after one decade when the first single crystalline wurtzite InN was produced [16, 17], InN-based devices are still unavailable due to the lack of high quality layers and insufficient thickness. Additionally, it is very challenging to produce In-rich InGaN and InAlN due to the miscibility of the alloys [45].

### 2.2.2 Surface electron accumulation

In a compound semiconductor, at a certain energy, called the branch-point energy, the valence band (VB) and conduction band (CB) states change their character from predominantly VB-like (or donor-like) to mostly CB-like (or acceptor-like). “Surface electron accumulation” is a term that indicates a phenomenon of a low  $\Gamma$ -point conduction band minimum (CBM) in the band structure of a semiconductor with respect to the branch-point energy (Fig. 2.5 of Refs. 46 and 47). Surface electron accumulation on the compound semiconductors has attracted much attention since a high surface electron density implies a great technological importance, i.e., for the formation of non-alloyed low resistance Ohmic contacts [48].

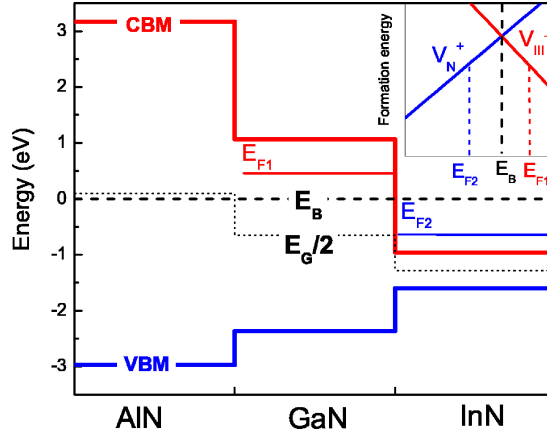


**Figure 2.6:** Conduction band minimum (CBM) and valence band maximum (VBM) of relaxed III-nitrides with respect to the branch point energy ( $E_B$ ) [59].  $E_F$  indicates the bulk Fermi levels of III-nitrides. Group-III vacancies:  $V_{III}^-$ , and N vacancies:  $V_N^+$ . The midgap energy at the  $\Gamma$ -point is thin dotted line.

Surface electron accumulation was observed to be an intrinsic property of InN with different surface orientations (polar [46, 47], semipolar [49], and nonpolar [49, 50]). Surface electron accumulation was also observed in In-containing III-nitride alloys such as InGaN [51] and InAlN [52]. For InGaN and InAlN alloys, a transition from electron accumulation (inversion) to electron (hole) depletion for  $n$ -type material was observed when In-rich layers were changed into Ga-rich InGaN ( $x_{In} = 0.29$ ) [51] and Al-rich InAlN ( $x_{In} = 0.59$ ) layers [52]. Surface electron accumulation was not only observed in InN and related alloys, but also in other In-containing semiconductors such as InAs [53–55], InSb [53], and  $In_2O_3$  [56].

The main reason of the appearance of the electron accumulation on the surface of polar InN (and related alloys) was attributed to In-In metallic bonds, leading to occupied surface states above the CBM [57]. The phenomenon of the surface electron accumulation on the surface of  $c$ -plane InN was observed by high resolution electron energy loss spectroscopy [46, 47]. From that phenomenon, an intrinsic surface electron accumulation layer was found to exist, and its existence was explained in term of the particularly low  $\Gamma$ -point CBM in InN (Fig. 2.5 of Refs. 46 and 47). Electron accumulation was a consequence of ionized donor type surface states pinning the surface Fermi level above the CBM [46, 47]. Recently, a native electron accumulation layer was found on the surface of  $n$ -type InN by scanning tunneling spectroscopy [58]. Calculations of

## 2.2. Material properties of InN and related alloys

---

energy positions of the  $\Gamma$ -point, the CBM, and VB maximum of III-nitrides with respect to the branch-point energy showed that the CBM lies far below the branch-point energy, and would be a reason for the appearance of the electron accumulation on the surface of InN layer (Fig. 2.6 of Ref. 59).

## Chapter 3

# Heteroepitaxy of III-nitrides

The growth of high quality epitaxial layers (i.e., smooth morphology, low defect density, and low unintentional impurities) is the back-bone of fundamental study and device fabrication. The word “*epitaxy*” is derived from the ancient Greek words: “*epi*” meaning “*upon*”, and “*taxis*” meaning “*arrangement*”. Thus, “*epitaxy*” means that the arrangement of atoms on an ordered substrate.

There are two different types of substrates, homo-epitaxy and hetero-epitaxy. Homo-epitaxy means that layer and substrate are of the same material. If the layer and the substrate are of different materials, then the substrate is called hetero-substrate (or foreign substrate) and the growth process is called hetero-epitaxy (e.g., GaN on sapphire substrate).

There are several techniques for epitaxy (Table 3.1), such as Vapor-Phase Epitaxy (VPE), Liquid-Phase Epitaxy (LPE), Molecular-Beam Epitaxy (MBE), Hydride-Vapor-Phase Epitaxy (HVPE), and Metal-Organic Vapor-Phase Epitaxy/Chemical-Vapor-Deposition (MOVPE or MOCVD). Among those techniques, MOVPE technique is the most used method and suitable for industrial mass-production of semiconductor nanostructures. Since 1968, after the first report on MOVPE growth [60], the MOVPE method has highly developed and evolved into a leading growth technique for III-V (i.e., GaAs, AlAs, and InAs) and III-nitride (AlN, GaN, and InN) compound semiconductor materials and their ternary alloys (i.e., InGaAs and InGaN). After the delivery of MOVPE system based on a rotating susceptor, the layer homogeneity over the wafer substrate has significantly improved. There are two different MOVPE systems with horizontal and vertical reactors. Nowadays, A majority of industrial MOVPE systems

### 3.1. MOVPE growth process: General considerations

---

Techniques	Strengths	Weaknesses
LPE	Simple High purity	Scale economics Inflexible Non-uniformity
HVPE	Well developed Large scale	Complex process/reactor Control difficult Hazardous sources
MBE	Simple process Uniform Abrupt interfaces <i>In-situ</i> monitoring	Expensive (capital) Low throughput
MOVPE	Higher flexibility Abrupt interfaces Simple reactor High purity	Expensive reactants Accurately control parameters Hazardous precursors

**Table 3.1:** Overview of epitaxy techniques [63].

is based on the horizontal laminar flow reactors and can perform a growth process on multi-wafers at the same time, i.e., 216×2-inch wafers or 24×6-inch wafers. Up to now, diameter of substrate wafer can reach to 8-inch in a 5×8-inch MOVPE system [61, 62].

This chapter will give a brief introduction about the MOVPE growth for III-nitrides. Further information can be found in Ref. 63.

### 3.1 MOVPE growth process: General considerations

Compared to MBE technique, where growth is mainly controlled by the kinetics of the surface processes via the reaction of the impinging species on the topmost atomic layers (growth conditions far from thermodynamic equilibrium) [64], MOVPE growth is governed by the diffusion processes [63]. MOVPE growth is conducted under near thermodynamic equilibrium conditions that relies on vapor transport of precursors in a heated zone [63]. A carrier gas (i.e., Ar, H<sub>2</sub>, or N<sub>2</sub>) is used to help the precursor transportation. In order to create these near equilibrium conditions, a substrate is typically located on a heated susceptor in the heated zone. Most of the MOVPE systems are based on the cold-wall reactors, where precursors are being delivered to the heated substrate by the carrier gas.

In MOVPE, growth occurs via the decomposition of the precursors over the heated

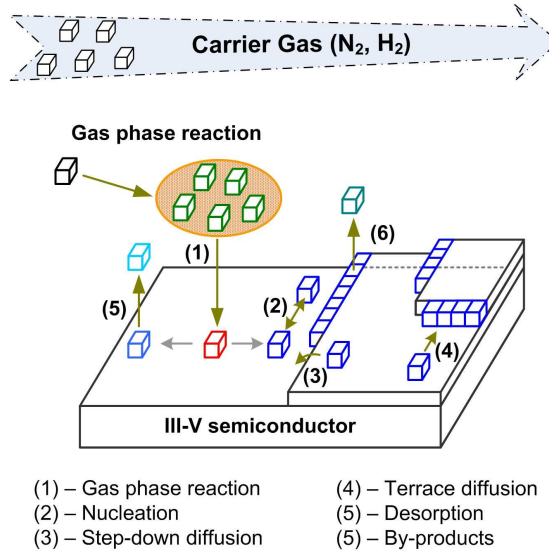


**Figure 3.1:** Surface processes involved in epitaxial layer growth.

substrates. During growth, there are numbers of reactions involving both homogeneous and heterogeneous reactions of the precursors as well as growth related surface processes, such as adsorption and desorption of the chemical species, and surface migration (nucleation and diffusion). The reactions during growth might be more complex due to the incomplete decomposition of the precursors. The appearance of many different decomposed products occurs during the growth process [63]. Basically, there are six reaction steps involving gas phase and surface reactions during an MOVPE growth process shown in Fig. 3.1.

(1) The carrier gas will transport the precursor molecules from the sources to the heated zone of the reactor where they will undergo gas phase decomposition. The resulting species diffuse through the boundary layer to the growing surface and physisorb onto the surface. At this moment, the species can either desorb or react with other surface species on the surface. The species can diffuse on the surface and incorporate into the layer (2, 3). There are two different diffusion processes, (3) terrace and (4) step-down diffusions. In principle, the terrace diffusion is more facile than the step-down diffusion and generally atoms are bound tighter at the bottom of a step [65]. Furthermore, the step-down diffusion is kinetically only significant at very high temperature [65]. During the growth process, (5) desorption and (6) by-products processes are simultaneously occurred. Due to the energetically instability, the species can be

### 3.1. MOVPE growth process: General considerations

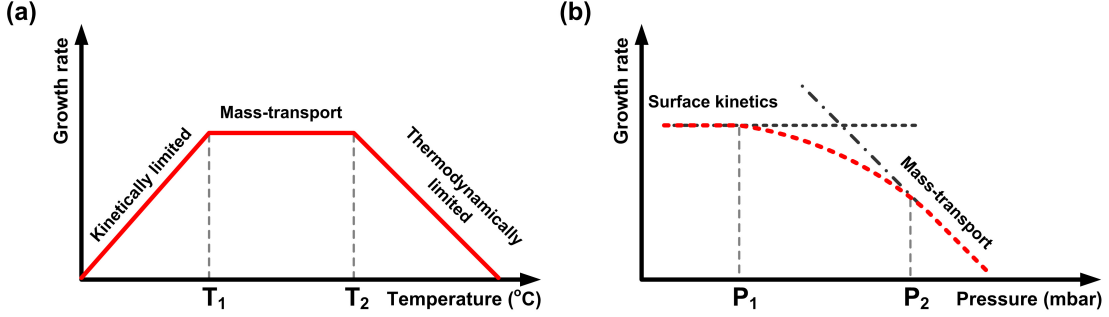


**Figure 3.2:** The effects of (a) substrate temperature and (b) reactor pressure during the MOVPE process on growth rate of layer [63].

desorbed from the surface. The gaseous by-products that desorb from the sample surface and diffuse in the carrier gas away from the deposition zone towards the reactor exhaust.

Those six steps occur simultaneously during the MOVPE growth process (Fig. 3.1). For different material systems and purposes of growth process, both different series and parallel reactions should be considered for the rate of overall reaction. For the complex MOVPE system, the overall reaction rate in the reactor is controlled by: *thermodynamics*, *kinetics*, *hydrodynamics*, and *mass transport* (Fig. 3.2 and Ref. 63). The thermodynamics determines the driving force which both causes and controls the direction of the reaction for the overall growth process. The kinetics defines the rates of change in the concentration of reactants in a chemical reaction. The hydrodynamics indicates the flow dynamics including fluid flow, heat transfer, and chemical transport of species in a typical MOVPE reactor. The hydrodynamics is strongly dependent on the reactor configuration and total system pressure, i.e., hydrodynamics occurs differently in horizontal and vertical MOVPE reactors. Overall, the thermodynamics, the kinetics, as well as the hydrodynamics and the mass transport must be understood not only to control the MOVPE growth process but also to develop new generation of the MOVPE system.

Generally, MOVPE growth is performed at temperatures similar to HVPE growth but much higher than used by MBE technique for III-nitrides. Because of the dependence on thermal decomposition of precursors, the MOVPE growth process strongly depends on growth temperature and the amount of precursors. At very high growth temperature, desorption (and etching) is dominating. If growth temperature is very

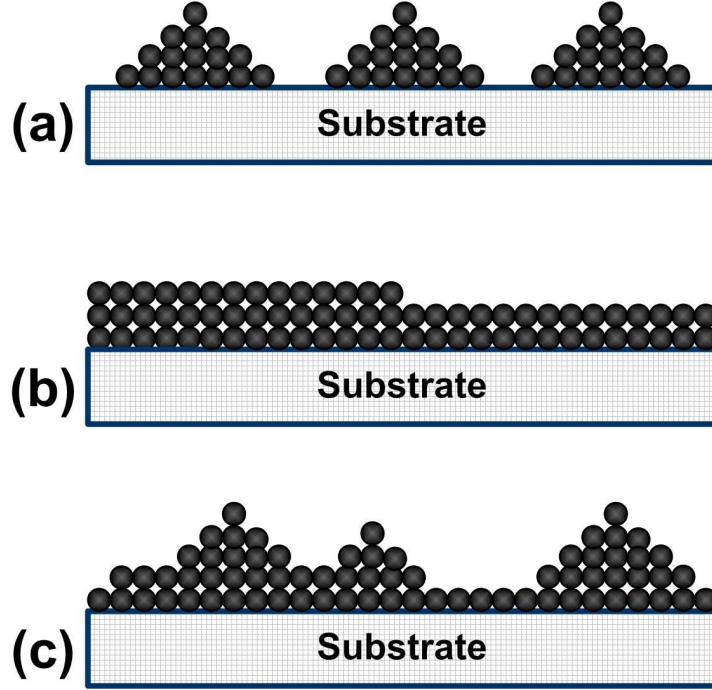


**Figure 3.3:** Growth modes of epitaxial layer: (a) Volmer-Weber [68], (b) Frank-van der Merve [69], and (c) Stranski-Krastanow [70].

low, the decomposition of precursors is less, and hence reducing growth rate. Figure 3.2 shows how substrate temperature and reactor pressure during the MOVPE process affect growth rate of layer. For example, if substrate temperature  $T_s < T_1$ , growth rate depends mainly on change of temperature but rarely on pressure; in mid-range of temperature ( $T_1 < T_s < T_2$ ), growth rate does not depend appreciably on temperature but increases with increasing pressure; and, if  $T_s > T_2$ , growth rate increases slowly, probably due to the homogeneous reactions in the gas phase, causing a depletion of reactants, or surface re-evaporation at that high temperature (Fig. 3.2(a)).

## 3.2 Modes of layer growth

Properties of epitaxial layer (i.e., morphology and structure) are strongly depended on growth conditions (e.g., temperature, precursor, and substrate). All of them contribute to different morphologies and structures of the grown layers. Depending on the growth conditions, the growth process of the layer might be followed different growth modes. The growth of epitaxial layers (homo- or hetero-generous) on a single crystal surface

### 3.3. Precursors for III-nitride epitaxy in MOVPE

---

depends significantly on the interaction strength between atoms and the surface. While it is possible to grow epi-layers from a liquid solution (e.g., in LPE), most epitaxial growth occurs via a vapor phase technique (e.g., MOVPE, HVPE, and MBE). There are three main growth modes shown in Fig. 3.3, which govern epitaxy [68–71].

The first growth mode, Volmer-Weber [68, 71], occurs normally when layer was grown on lattice-mismatched substrate (e.g., InN/GaN), leading to the formation of large islands of crystal (three-dimensional structure (3D)). When atoms reach to the substrate surface, adatom-adatom interactions are stronger than the interactions between the atoms with the surface. The atoms prefer to aggregate each other instead of attaching to the substrate, leading to the formation of 3D adatom clusters or islands. Layer based on the Volmer-Weber growth mode shows a very rough surface with 3D structure.

When layer and substrate are relatively lattice-matched (e.g., GaN/GaN), atoms attach preferentially to surface sites resulting in atomically smooth, and fully formed layers. This layer-by-layer growth is two-dimensional (2D), indicating that complete layers form prior to growth of subsequent layers. This growth mode is called a layer-by-layer growth or 2D growth mode, discovered by Frank-van der Merwe [69, 71].

A combination (transition) of the two first growth modes (layer-plus-island growth) is called Stranski-Krastinov [70, 71], when atoms reach to the substrate surface, they not only form a 2D layer but also aggregate to form a 3D structure on top of the pseudomorphic 2D layer. This transition from the layer-by-layer to island-based growth occurs at a critical layer thickness which is strongly dependent on the chemical and physical properties of the substrate and the layer (i.e., surface energies and lattice parameters). The Stranski-Krastanow growth mode can be observed during the growth of semiconductor nanostructures, especially quantum dots.

### 3.3 Precursors for III-nitride epitaxy in MOVPE

III-nitride semiconductors consist of group-III elements (Al, Ga, or In) and group-V element (N). III-group alkyls denote as  $R_3-M$ , where R is an organic radical, typically methyl ( $\cdot\text{CH}_3$ ) or ethyl ( $\cdot\text{C}_2\text{H}_5$ ); and M represents the metallic group-III (Al, Ga, or In). The group-V precursor is binary hydrogen compounds (e.g., ammonia  $\text{NH}_3$ ). Overview of reactions during III-nitride growth is illustrated in Fig. 3.4. The reaction

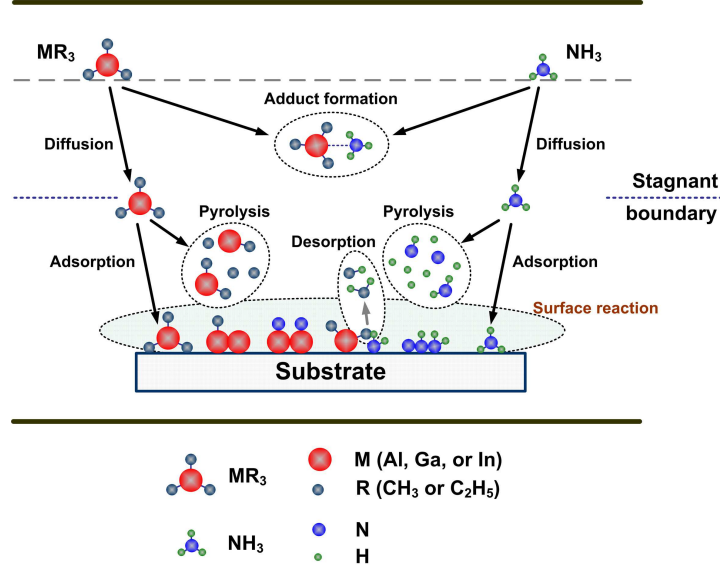


Figure 3.4: Reactions during growth of III-nitrides.

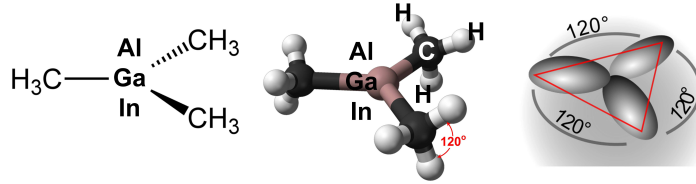


Figure 3.5: Group-III-methyl molecules [63].

in the MOPVE system can be simply described in Eqn. 3.1. The details about the decomposition of the group-III precursors and  $\text{NH}_3$  will be discussed later.



### 3.3.1 Group-III molecular sources

For III-nitride growth, there are few different precursors for group-III sources such as trimethyl-aluminum/-gallium/-indium ( $\text{Al-/Ga-/In-(CH}_3)_3$  or TMAI/TMGa/TMIn) and tri-ethyl-gallium ( $\text{Ga-(C}_2\text{H}_5)_3$  or TEGa). Tri-ethyl-aluminum/-indium (TEAl/TEIn) are very unstable and do not exist in reality for growth [63]. Basically, the bonding in group-III-alkyl molecules has the same hybridized  $sp^2$  configuration. That configuration forms a planar trigonal molecule with three ligands separated by angles of  $120^\circ$ . Since

### 3.3. Precursors for III-nitride epitaxy in MOVPE

in one group-III-alkyl molecule consists of 3 alkyl groups, one unfilled  $p$ -orbital (due to the lack of one pair electron) exists perpendicular to the plane of molecule that causes the group-III alkyls be electron acceptors. Thus, group-III alkyls can be considered as an *acid* group. According to the main material systems will be discussed in this thesis, only chemical properties of TMAI, TMIIn, TEGa, and TMGa precursors will be mainly described.

For the MOVPE growth of III-nitrides, the stability of the group-III precursors is very important since it decides which growth temperature is necessary for epitaxy. Table 3.2 shows the metal-ligand bond strength, the energy needed to break the first carbon-metal bond, of the different group-III alkyls. Among the group-III alkyls, TMIIn has the smallest carbon-metal bond strength, leading to the decomposition of TMIIn at lower temperature compared to TMAI and TMGa. TEGa has smaller bond strength and lower melting point than TMGa, therefore TEGa is less stable than TMGa and decomposes at lower temperatures. Pyrolysis thermal decomposition of the group-III alkyls in the heated reactor can only go either by radiative decomposition ( $\text{NH}_3$ , TMGa, and TMIIn) or via  $\beta$ -hydride elimination reaction of TEGa (decomposed mainly into Ga,  $\text{C}_2\text{H}_4$ , and  $\text{H}_2$ ) [66]. Details for the pyrolysis of the group-III precursors can be found in Ref. 63. For example, the pyrolysis process of TMIIn (similar to TMAI and TMGa) in  $\text{N}_2$  environment may be considered in terms of the following mechanisms (Eqn. 3.2 and Ref. 67). Since the decomposition of  $\text{NH}_3$  (see next section) will produce  $\cdot\text{H}$  atoms, the reaction between the  $\cdot\text{H}$  and the decomposed production of TMIIn might occur as well (Eqn. 3.3). This process would enhance TMIIn decomposition further.

Precursors	TMAI	TMGa	TEGa	TMIIn	$\text{NH}_3$
Bond strength (kcal/mole)	65	60	57	47	97
Melting point ( $^\circ\text{C}$ )	15	-15.8	-82.5	88	-77.73
Boiling point ( $^\circ\text{C}$ )	126	55.8	143	135.8	-33.34

**Table 3.2:** Physical properties of group-III precursors and  $\text{NH}_3$  [63].

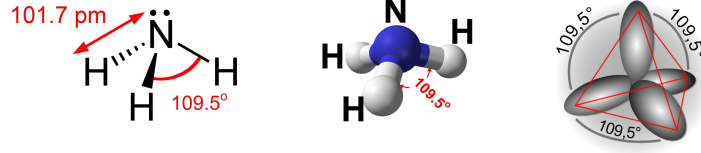
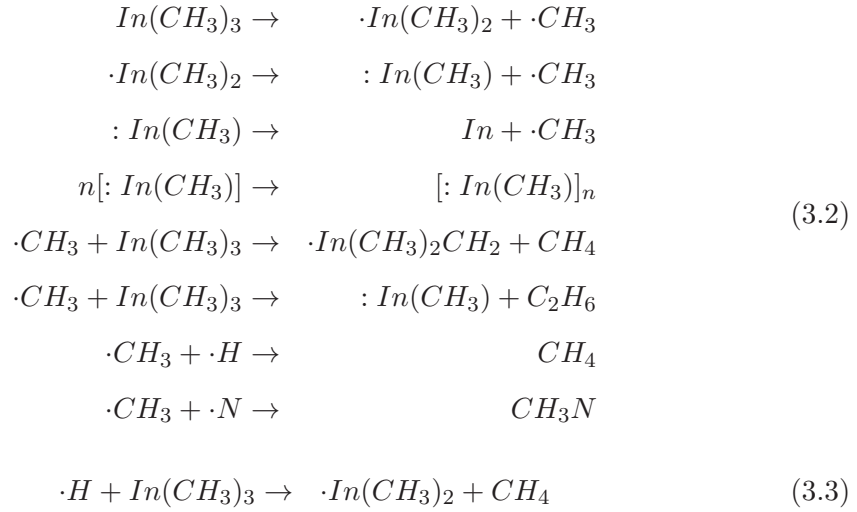
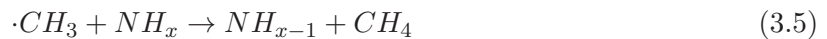
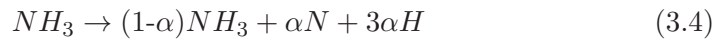


**Figure 3.6:** Molecular structure and hybridized  $sp^3$  configuration of ammonia [63].



### 3.3.2 Ammonia

Similar to other group-V precursors (like  $\text{AsH}_3$  and  $\text{PH}_3$ ),  $\text{NH}_3$  is a hybridized  $sp^3$  forming a tetragonal bonding configuration with angles of  $109.5^\circ$  [63].  $\text{NH}_3$  can be considered as a *base*, because it can donate a pair of electrons (Fig. 3.6). In contrast to the group-III precursors, the bond strength of  $\text{NH}_3$  is very high ( $\sim 97$  kcal/mole), therefore high temperatures are needed to break N-H<sub>3</sub> bond (Table 3.2).  $\text{NH}_3$  decomposition process can be simply described in Eqn. 3.4. Furthermore, during the growth process of III-nitrides, since TMIIn (and TMGa, TEGa, etc.) will be supplied together with  $\text{NH}_3$ , addition reaction might be occurred (Eqn. 3.5 and Fig. 3.4)



The decomposition rate of  $\text{NH}_3$  increases exponentially with increasing temperature

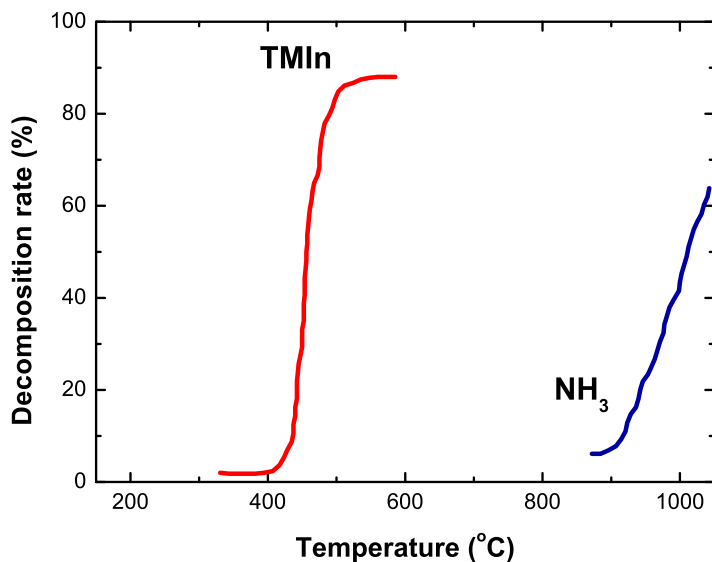


**Figure 3.7:** Decomposition rates of  $\text{NH}_3$  [72, 73] and  $\text{TMIIn}$  [77] as functions of temperature.

shown in Fig 3.7 [73, 74]. The decomposition rate of  $\text{NH}_3$  below  $900^\circ\text{C}$  is less than 10%, and at  $500\text{-}600^\circ\text{C}$  the rate is just about 0.5-3.5%, respectively [72, 75]. In fact, the pyrolysis thermal decomposition of  $\text{NH}_3$  is complex and produces several different N-species, such as  $\cdot\text{NH}_2$ ,  $\text{N}_2\text{H}_2$ ,  $:\text{NH}$ , even some of them react again with H-atoms to re-form  $\text{NH}_3$ . Further information about the  $\text{NH}_3$  decomposition can be found in Ref. 76.

### 3.4 Substrates for III-nitride epitaxy

Generally, growth of III-nitrides is performed at high temperature on a homogeneous or inhomogeneous substrate (e.g., sapphire). For example, growth of  $\text{InN}$  is usually conducted at  $500\text{-}600^\circ\text{C}$  in MOVPE and at  $400\text{-}500^\circ\text{C}$  in MBE. There are always thermal expansion and lattice mismatches between layer and foreign substrates (Table 3.3). The thermal expansion coefficient (TEC) parameters of III-nitrides and substrate have to be considered together with their lattice mismatches since they strongly affect growth process and quality of epitaxial layers. Due to different properties between substrates and III-nitrides, suitable growth procedures and growth parameters should be chosen not only to grow but also to improve quality of epitaxy. Table 3.3 shows the ther-

Materials	Symmetry (Space group)	Lattice constants ( $\text{\AA}$ )	Lattice mismatch (%)			TEC ( $\times 10^{-6} \text{ K}^{-1}$ )
			InN	GaN	AlN	
Al <sub>2</sub> O <sub>3</sub> (0001)	Rhombohedral (R $\bar{3}c$ )	$a_o=4.758$ $c_o=12.991$	29.8	16.0	13.2	7.30 8.50
Silicon (111)	Cubic (FdR $\bar{3}m$ )	$a=5.430$	8.0	-16.9	-18.9	3.59
InN	Wurtzite (P6 <sub>3</sub> mc)	$a_o=3.545$ $c_o=5.703$	–	-10.0	-16.0	3.80 2.90
GaN	Wurtzite (P6 <sub>3</sub> mc)	$a_o=3.189$ $c_o=5.186$	10.0	–	-2.4	5.59 3.17
AlN	Wurtzite (P6 <sub>3</sub> mc)	$a_o=3.112$ $c_o=4.982$	16.0	2.4	–	4.15 5.27

**Table 3.3:** Material parameters of III-nitrides and different substrates [29].

mal expansion coefficients and lattice mismatches at room temperature of the wurtzite III-nitrides and substrates. Lattice mismatch is calculated using the formula:  $(a_{\text{layer}} - a_{\text{substrate}})/a_{\text{substrate}}$ , where  $a_{\text{layer}}$  and  $a_{\text{substrate}}$  are the in-plane lattice parameters of epitaxial layer and substrate, respectively.

Beside lattice mismatch and thermal expansion parameters, other parameters should be taken into account when grow III-nitrides are thermal stability and the polarity of substrate. Thermal stability of substrates is very important since III-nitrides are normally grown at high temperatures. An easily decomposed substrate at high temperature might be a source for unintentionally contaminations in the epitaxial layers since elements can diffuse from the substrate into the layer. Lastly, the polarity of substrate is very important for III-nitride epitaxy, leading to growth of different polarity of epitaxial layer. III-nitrides having different polarities shows different thermal stabilities, different amount of contaminations, and different defects as well, i.e., group-III-polar layer is more thermal stable and more chemically inert than group-V-polar layer.

### 3.4.1 Sapphire

Despite the high lattice and thermal mismatches between sapphire and III-nitrides (Table 3.3), sapphire is still most widely used substrate due to a low-cost production, large size (up to 4-inch wafer), strong thermal stability, and easy handling. The melting point of sapphire is about 2040°C [29]. Sapphire actually has a trigonal structure, however, it can be considered as a rhombohedral structure having a strong anisotropic struc-

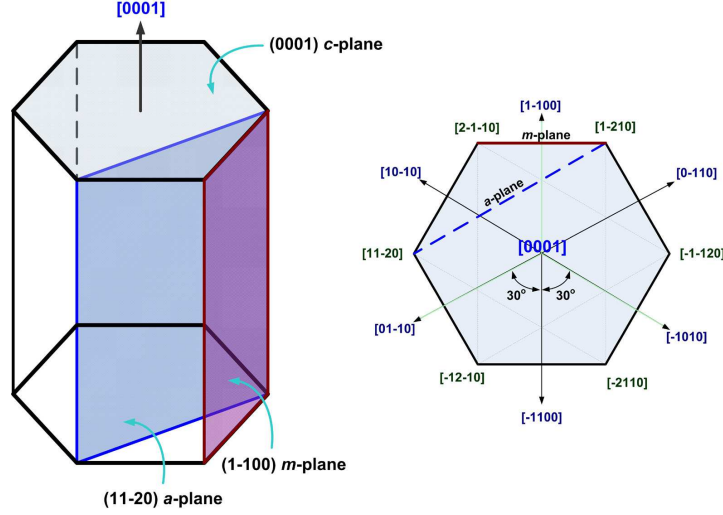


Figure 3.8: Structure of sapphire and relative planes.

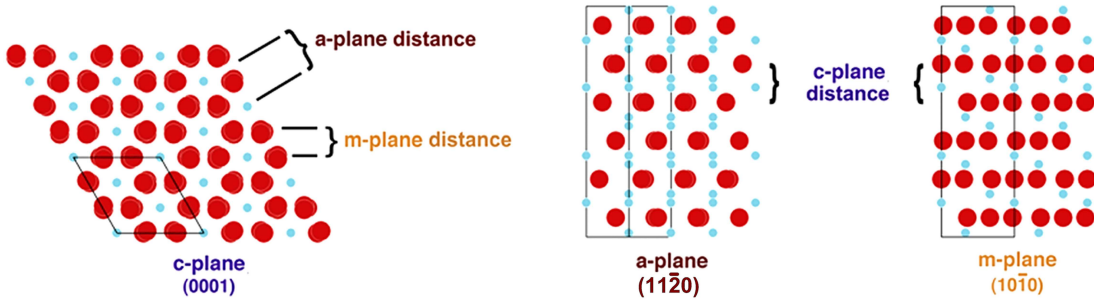


Figure 3.9: Atomic structures of  $a$ -( $11\bar{2}0$ ),  $c$ -( $0001$ ), and  $m$ -( $1\bar{1}00$ ) surfaces of sapphire [78].

ture (Table 3.3 and Fig. 3.8). Furthermore, bandgap of sapphire is about 9.0 eV [29], which permits an excellent optical transmission with very little absorption for III-nitride based light emitting devices. To date, several surface oriented sapphire substrates are used to grow III-nitrides, such as  $a$ -plane ( $11\bar{2}0$ ),  $c$ -plane ( $0001$ ),  $m$ -plane ( $1\bar{1}00$ ), and  $r$ -plane ( $10\bar{1}2$ ) sapphire.

Control growth orientation of III-nitrides is very important since on which structure, morphology, electrical and optical properties strongly depend. Generally, III-nitride layers grown on  $c$ -plane sapphire will have the  $[0001]$   $c$ -growth-direction, while other growth directions of III-nitrides might be achieved on other planes of sapphire. However, due to different crystal structures between III-nitrides and the other planes of sapphire, it is very difficult to control semi- and non-polar growth orientations of

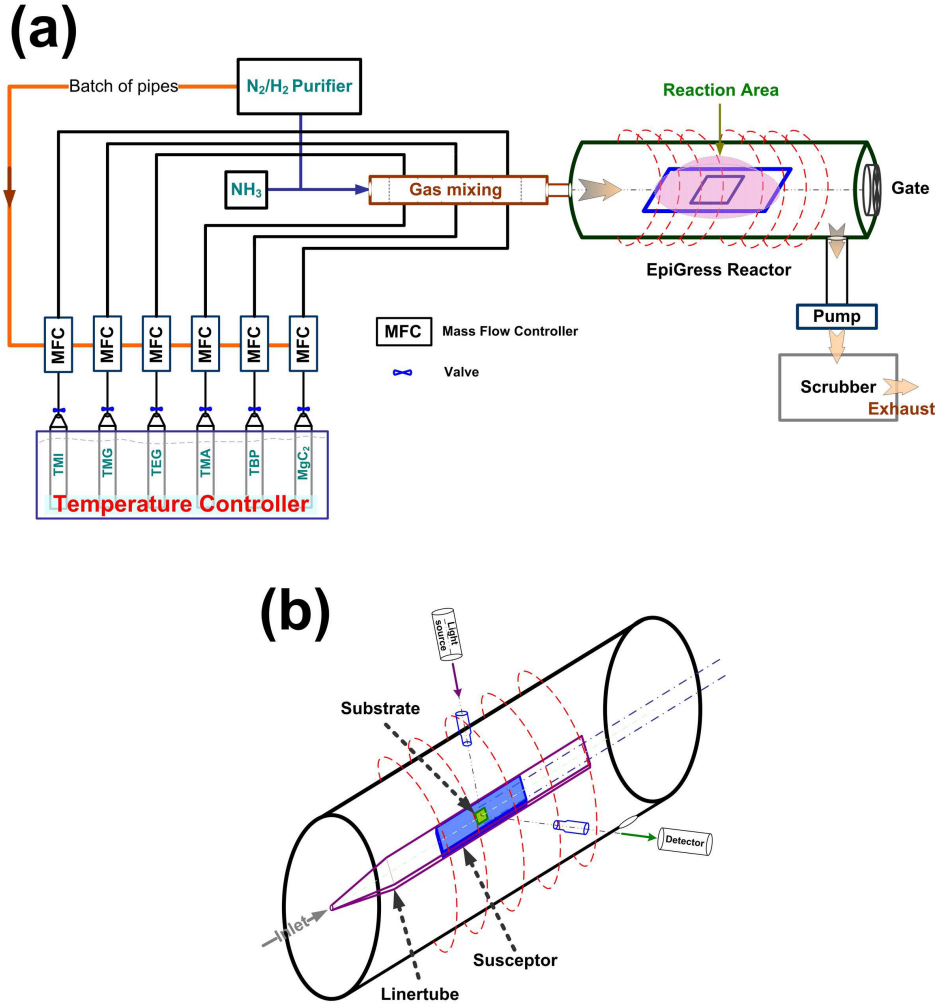


Figure 3.10: (a) EpiGress MOVPE system and (b) the MOVPE reactor.

III-nitrides on sapphire. Generally, to grow III-nitride layers directly on sapphire substrate, a nitridation process is employed. Details about the sapphire nitridation will be discussed in next chapter.

In contrast to sapphire substrate, the other group III-nitrides are good candidates for substrate selections since they are having the same wurtzite crystal structures, much smaller lattice and thermal mismatches compared to sapphire (Table 3.3). Generally, the overgrown layer on the other III-nitride substrates reproduces the crystal orientation and the polarity of the substrates, i.e., In-polar (0001) InN on Ga-polar (0001) GaN.

However, production/preparation of III-nitride substrates is difficult. Due to the

cost of free-standing III-nitride substrates, III-nitride based substrates are commonly deposited on sapphire (e.g., GaN template on sapphire). Since the growth of semi- and non-polar III-nitride templates on sapphire is still itself challenging, those are often produced on other bulk substrates.

## 3.5 MOVPE setup and growth procedures

In this thesis, all experiments (InN, GaN, and InGaN epitaxy) were performed in a double-wall horizontal MOVPE reactor system, EpiGress VP50RP system (Fig. 3.10) produced in 1983 by EPIQUIP. The EpiGress MOVPE system is fitted with an *in-situ* ellipsometric spectroscopy (SE). The *in-situ* SE is mainly used to monitor growth process (Fig. 3.10(b)). Bare sapphire or GaN/sapphire template was used as substrate (about  $2 \times 2 \text{ cm}^2$  or quarter of 2-inch wafer), the substrate was put on a fixed graphite susceptor. The susceptor will be loaded to center of a quartz liner-tube. External radio-frequency generator is used to control temperature via a thermo-couple. Carrier gas is either hydrogen ( $\text{H}_2$ ) or nitrogen ( $\text{N}_2$ ) with a flux of 31/min. The reactor pressure was kept constant at 100 mbar.

### 3.5.1 *In-situ* monitoring by ellipsometry

Compared to other techniques (e.g., X-ray diffraction, AFM...), SE is a versatile and powerful optical technique. By using SE, many fundamental physical parameters can be extracted from layer such as morphology, crystal quality, and chemical composition. Further information about SE can be found in Ref. 79. In this thesis, the *in-situ* SE is mainly used to monitor the growth process and to extract layer thickness. The energy range is of 1.6-6.5 eV.

SE measures the change of polarization upon reflections or transmission. The polarization state of the incident light (with an angle of incident of  $\phi$ ) upon the sample consists of *s*-component (or *s*-polarization), which perpendiculars to plane of incidence or parallel to the surface of sample, and *p*-component, which parallels to plane of incidence (Fig. 3.11). The amplitudes of the *s*- and *p*-components are  $r_s$  and  $r_p$ , respectively. Complex reflection ratio ( $\rho$ ) can be calculated as:

$$\rho = \frac{r_p}{r_s} = \tan \Psi \times e^{i\Delta}, \quad (3.6)$$

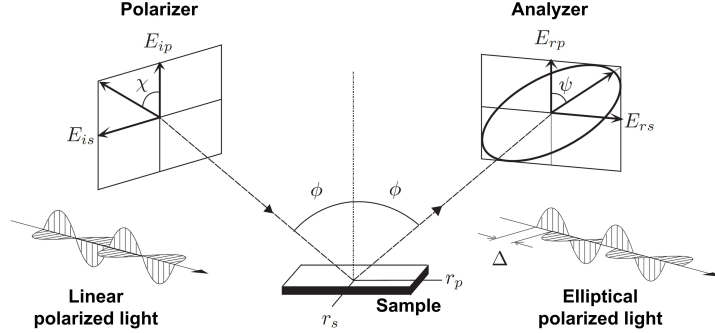


**Figure 3.11:** Schematic illustration of ellipsometric spectroscopy.

where  $\Delta$  is the phase shift.  $\tan\Psi$  is sensitive to surface chemistry since it is directly affected by a change in  $|r_p/r_s|$ .  $\cos\Delta$  is sensitive to layer roughness and layer thickness. Pseudo-dielectric function can be described as:

$$\langle\epsilon\rangle = \sin^2\phi\left(1 + \tan^2\left(\frac{1 - \rho}{1 + \rho}\right)\right). \quad (3.7)$$

Pseudo-dielectric function can be simply described as:  $\langle\epsilon\rangle = \langle\epsilon_1\rangle + i\langle\epsilon_2\rangle$ . Where  $\langle\epsilon_1\rangle$  and  $\langle\epsilon_2\rangle$  are the real and imaginary parts of the pseudo-dielectric function, respectively. The imaginary part  $\langle\epsilon_2\rangle$  plotted as a function of photon energy (in eV unit) can give positions of inter-band transition energies (or critical points) of Brillouin zone of material, where the transition probability is maximum. For example, in 1.6-6.5 eV photon energy range, typically  $E_1$  ( $\sim 4.9$  eV),  $E_2$  ( $\sim 5.3$  eV), and  $E_3$  ( $\sim 6.1$  eV) inter-band transition energies of wurtzite InN can be observed by  $\langle\epsilon_2\rangle$  spectrum as shown in Fig. 3.12(b) [80]. These three inter-band energy transitions of InN can be seen in the energy band structure of wurtzite InN in Fig. 2.5). Intensity of the imaginary part  $\langle\epsilon_2\rangle$  is strongly affected by thickness, defects, and roughness of the layer. For example, the intensities of the inter-band energy transitions of InN shown in Fig. 3.12(b) indicate that InN on *m*-plane sapphire (Fig. 6.5) is much rougher than InN on *c*-plane sapphire (Figs. 5.3 and 5.14).

### 3.5.2 InN on sapphire

InN was grown on quarters of 2-inch sapphire wafers. In order to remove residual contaminations, sapphire substrate was degreased sequentially by acetone and iso-propanol solvents for 10 min, and then rinsed in de-ionized water prior to growth.

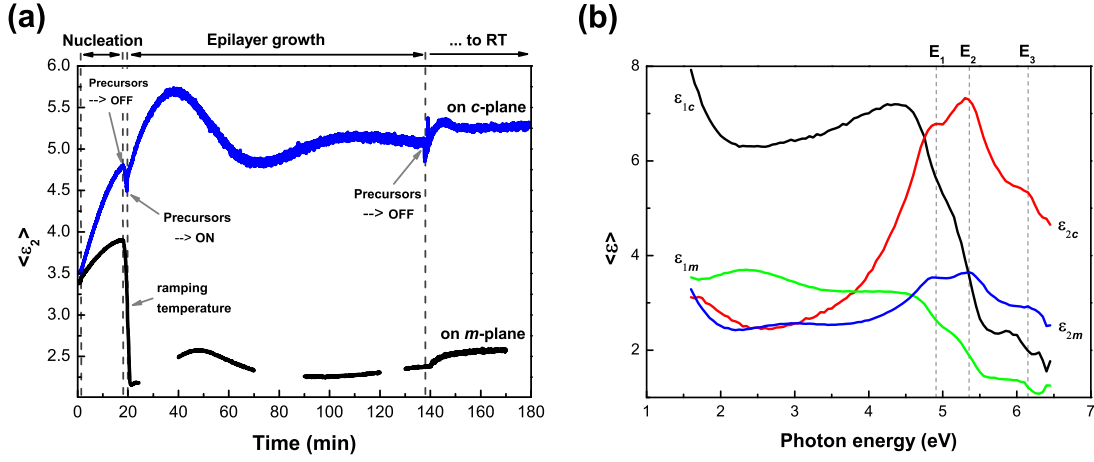


**Figure 3.12:** (a) Ellipsometric transients ( $\langle \epsilon_2 \rangle$ ) during InN growth on  $c$ -plane (0001) and  $m$ -plane ( $1\bar{1}00$ ) sapphire. The transients were recorded during InN nucleation at  $500^\circ\text{C}$ , during InN epilayer at  $560^\circ\text{C}$ , and after growth during cooling to room temperature (RT). And (b) real ( $\langle \epsilon_{1c/m} \rangle$ ) and imaginary ( $\langle \epsilon_{2c/m} \rangle$ ) parts of the pseudo-dielectric functions of InN on  $c$ - and  $m$ -plane sapphire. The spectra were *in-situ* recorded after growth at room temperature with an angle of incidence of  $67.5^\circ$ . The pseudo-dielectric function of InN on  $m$ -plane sapphire was recorded along the  $[0001]_{\text{sapphire}}$  direction.

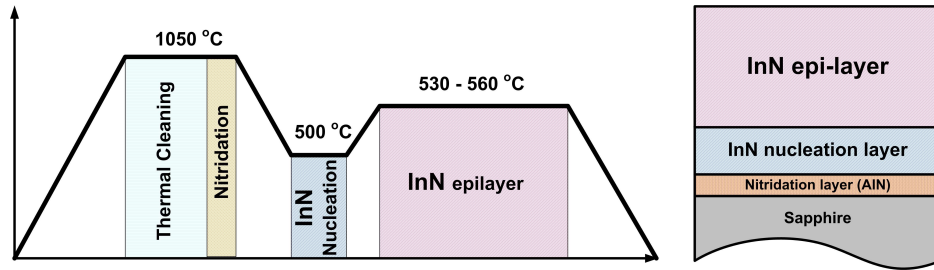


**Figure 3.13:** Growth diagram of InN on sapphire.

For InN growth, TMIIn and  $\text{NH}_3$  were used as In- and N-sources, respectively. Reactor pressure was kept at 100 mbar for all processes. Growth diagram of InN on sapphire is shown in Fig. 3.13, including a 3-step growth mode. (1) Nitridation: the sapphire substrate was first annealed at  $1050^\circ\text{C}$  under  $\text{H}_2$  carrier gas for 10 min; then, the gas was switched to  $\text{N}_2$  to nitridate the substrate at the same temperature with 1-3 l/min  $\text{NH}_3$ . (2) Nucleation:  $\text{NH}_3$  was used as N-source with a flow rate of 1 l/min. The InN nucleation process was performed at  $500^\circ\text{C}$  for 20 min with a V/III ratio of  $\sim 22000$ . (3) InN epilayer: the epilayer was grown at  $520$ - $560^\circ\text{C}$  with a V/III ratio of 12000-15000.

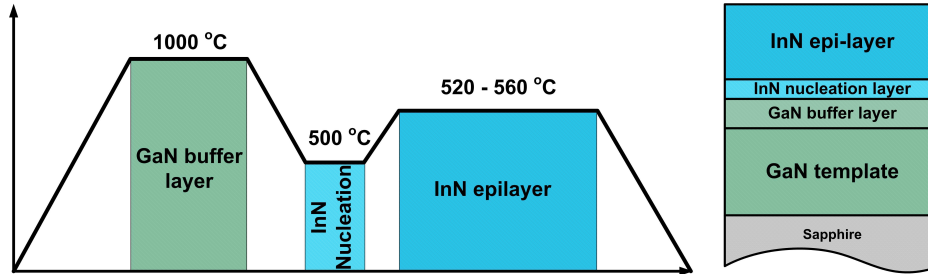


Figure 3.14: Growth diagram of InN on GaN.

### 3.5.3 InN on GaN templates

To remove surface oxides and residual contaminations, GaN template was degreased by acetone and iso-propanol, and rinsed in de-ionized water. Afterwards, the template was etched by  $\text{H}_2\text{SO}_4 : \text{H}_2\text{O}_2 : \text{H}_2\text{O}$  (3 : 1 : 1) solution, and then rinsed in de-ionized water.

Growth diagram of InN on GaN template is shown in Fig. 3.14. (1) Before InN growth on GaN template, a GaN buffer growth step at 980-1000°C was performed instead of the nitridation process. TMGa was chosen as Ga-source,  $\text{NH}_3$  was used with a flow rate of 1 l/min, and a V/III ratio of 1600 was chosen. The GaN buffer growth was performed under  $\text{H}_2$  carrier gas for 15 min to get a thickness of 150-200 nm. (2) After the GaN buffer growth, the carrier gas was switched to  $\text{N}_2$ , and the template was cooled to 500°C to deposit the InN nucleation layer for 20 min at a V/III ratio of  $\sim 22000$ . (3) Following the nucleation, the sample was heated to 520-560°C to grow the InN epilayer with a V/III ratio of 12000-15000.

### **3.5. MOVPE setup and growth procedures**

---

## Chapter 4

# Sapphire nitridation

For the epitaxially growth of III-nitride semiconductors on foreign substrates (i.e., sapphire and  $\text{LiAlO}_2$ ), an initial nitridation process is commonly employed to improve the growth. The nitridation is an exposure of substrate surface at high temperature (normally higher than room temperature) to a nitrogen source (e.g.,  $\text{NH}_3$ ), leading to an incorporation of N-atoms into the surface of substrate to form a very thin nitrogen containing layer (1 - 2 nm) (e.g.,  $\text{AlN}$  and/or  $\text{AlN}_x\text{O}_y$  layer on sapphire [81, 82]).

Despite the large lattice and thermal expansion mismatches between sapphire and III-nitrides (Table 3.3), sapphire is still the mostly used substrate for III-nitride growth. The sapphire nitridation is very important not only to improve crystallinity [83, 84] and surface morphology [84], but also to improve electrical and optical properties of III-nitrides [83, 85]. For example, short nitridation (1 - 2 min at  $1050^\circ\text{C}$ ) of *c*-plane sapphire leads to a reduction of screw dislocation density and electron carrier concentrations of epitaxially grown  $\text{InN}$  layers [83]. However, III-nitrides grown on bare sapphire (without nitridation) have metastable rotations [86]. Thus, in the following sections, I will focus on the nitridation on sapphire substrate.

Due to the different lattice and thermal mismatches between III-nitrides and sapphire (Table 3.3), nitridation is employed to reduce those differences. Indeed, a thin  $\text{AlN}$  layer might improve the nucleation process. An optimized nitridation (time and temperature) is significant to improve surface morphology of the epitaxial layers. At a certain temperature, longer nitridation times lead to the growth of thicker and rougher nitridation layers, which can be contributed to the growth of rougher epitaxial layers (i.e., three-dimensional morphology). Very short nitridation time might be insufficient

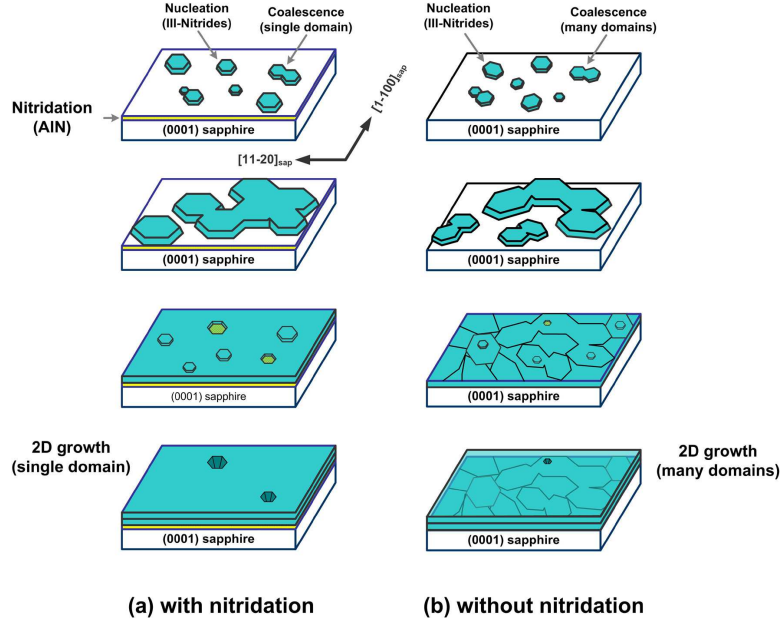


**Figure 4.1:** Proposed growth of III-nitride layers grown on sapphire (a) with and (b) without nitridation.

to produce a full coverage of the nitrogen containing layer at the sapphire surface, which might result in the growth of layer with metastable domains. Figure 4.1 shows proposed epitaxial layers grown directly on sapphire with and without nitridation. Growth without sapphire nitridation commonly causes many rotated crystallite domains (or metastable domain rotations), while after the sapphire nitridation the epitaxial layer does not exhibit rotated domains [86].

Sapphire with different surface orientations such as  $c$ -plane (0001),  $m$ -plane ( $1\bar{1}00$ ), and  $r$ -plane ( $10\bar{1}2$ ) is commonly used for III-nitride growth. In fact, different sapphire substrates, which have different surface symmetries and in-plane lattice constants, lead to the growth of different orientations of III-nitrides, sometimes even lead to the growth of random growth orientations. Sapphire with  $m$ - or  $r$ -orientation is commonly used as substrate to produce nonpolar (e.g.,  $m$ -plane) and semipolar (e.g., ( $10\bar{1}3$ ) or ( $11\bar{2}2$ ) plane) III-nitrides. Controlling the growth orientation of III-nitrides on differently oriented surface sapphire substrates is a big challenge. Generally, III-nitrides grown on  $c$ -plane sapphire will have the  $c$ -growth orientation; however, layers grown on other surface oriented sapphire substrates might have more than one growth orientation. Since nitridation is very crucial to control for the growth orientation of III-nitrides.

Sapphire	Lattice constant ( $\text{\AA}$ )	Surface energy ( $\text{J m}^{-2}$ )
$c$ -plane (0001)	$a_o=4.758$ $c_o=12.991$	1.98 ( $S_a = 19.53 \text{\AA}^2$ )
$r$ -plane ( $10\bar{1}2$ )	$a_o=4.758$ $c'=15.384$	2.04 ( $S_a = 24.27 \text{\AA}^2$ )
$a$ -plane ( $11\bar{2}0$ )	$a_o=8.241$ $c_o=12.991$	2.34 ( $S_a = 35.49 \text{\AA}^2$ )
$m$ -plane ( $1\bar{1}00$ )	$a_o=4.758$ $c_o=12.991$	2.56 ( $S_a = 61.46 \text{\AA}^2$ )

**Table 4.1:** Lattice constants of the surface unit cell [29] and surface energies [87] of sapphire with different surface orientations. The surface energies of sapphire were calculated for the certain surface areas ( $S_a$ ) by the generalized gradient approximation (GGA) [87]. The  $c'$ -axis parallels to the  $c$ -axis of sapphire.

By carefully optimizing the nitridation, single phase semi-/non-polar layers might be obtained.

Sapphire nitridation is normally performed at much higher temperatures by MOVPE (e.g., at  $1050^\circ\text{C}$ ) than by MBE (e.g., at  $400^\circ\text{C}$ ). The main reason for the difference in temperatures is derived from the different nitrogen sources in MOVPE ( $\text{NH}_3$ ) and in MBE (a radio frequency nitrogen plasma source). In MOVPE, higher nitridation temperatures are required to crack  $\text{NH}_3$ . However, epitaxial layers produced by both the methods are also strongly affected by the nitridation process.

The nitridation plays a key role in III-nitride polarity selection [88, 89]. After nitridating sapphire, a thin AlN layer will be formed on the topmost of sapphire, serving as a buffer layer for the epitaxial growth. The nitridation of  $c$ -plane sapphire affects the polarity of epitaxial III-nitrides in MOVPE and in MBE. By controlling the polarity of the nitridation layer, one can control the polarity of the epitaxial III-nitride layers. Direct measurement of the polarity of the nitridation layer is difficult since the layer is very thin to perform any known method for polarity determination. The only way is to measure the polarity of the epitaxial layer that corresponds to the polarity of the nitridation layer. So far, the polarity control of III-nitrides on sapphire was mostly done by varying the nitridation temperature. Nitridation at higher temperatures (e.g.,  $400^\circ\text{C}$  -  $500^\circ\text{C}$ ) in MBE usually produces group-III polarity, while nitridation at lower temperatures results in N-polarity. In contrast to MBE, the nitridation in MOVPE was mostly performed at much higher temperatures (e.g.,  $\sim 1000^\circ\text{C}$ ), leading to the growth

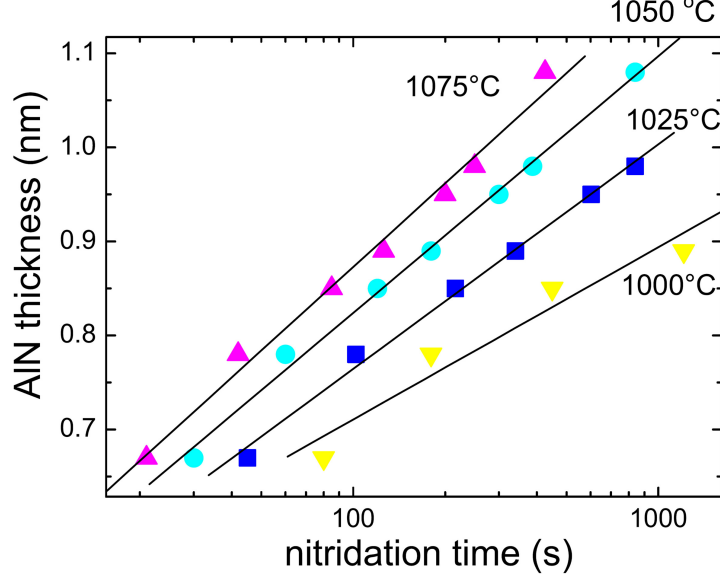


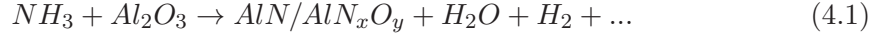
**Figure 4.2:** Thickness of nitridation layers on *c*-plane sapphire as functions of nitridation time and temperatures [92].

of N-polarity (e.g., N-polar InN [88] and N-polar GaN [89]), while nitridation at lower temperatures (e.g.,  $\sim 900^\circ\text{C}$ ) results in the growth of group-III polarity (e.g., In-polar InN [88]).

Additionally, due to the different growth conditions, the polarity and the crystal structure of nitridation layer formed by MOVPE and MBE are different. By using MBE, the nitridation layer on *c*-plane sapphire showed a cubic phase, having an in-plane relationship of  $[11\bar{2}]_{\text{AlN}} \parallel [11\bar{2}0]_{\text{sapphire}}$  and  $[111]_{\text{InN}} \parallel [0001]_{\text{sapphire}}$  [90]. The nitridation layer on *c*-plane sapphire in MOVPE showed a wurtzite phase [91], having an in-plane relationship of  $[1\bar{1}00]_{\text{AlN}} \parallel [11\bar{2}0]_{\text{sapphire}}$  and  $[0001]_{\text{AlN}} \parallel [0001]_{\text{sapphire}}$ .

## 4.1 Nitridation mechanism

Up to date, nitridation was mostly investigated for *c*-plane sapphire using different methods, which are mostly sensitive to surface chemistry such as X-ray photoelectron spectroscopy (XPS) [81, 82] or *in-situ* ellipsometry (SE) [92]. In an MOVPE reactor, the sapphire nitridation is performed by introducing  $\text{NH}_3$  to the reactor at high temperature. Chemically, the reaction can be simply described as followed:



However, as discussed in the previous chapter, the pyrolysis of  $NH_3$  is complex and might produce many byproducts, i.e., N-, H-, and  $NH_x$ -radicals. For simple use, the term “N-species” will be later used for N- and  $NH_x$ -radicals. Overall, the sapphire nitridation is based on the following processes: (1) N-species diffuse into sapphire surface, (2) the N-species will substitute O-atoms of sapphire, and (3) bind to Al-atoms to form AlN and/or  $AlN_xO_y$  [81, 82, 93].

Due to the low decomposition rate of  $NH_3$  (e.g., less than 10% at 800°C [72]), the nitridation process in the MOVPE system strongly depends on temperature. For *c*-plane sapphire the nitridation layer thickness increases exponentially with nitridation time and temperature as determined by simulations from the *in-situ* SE. The thickness of nitridation layer was about 1 nm (about 2-3 monolayers) for 2 min at 1050°C (Fig. 4.2 of Ref. 92).

## 4.2 Nitridation in MOVPE

Before nitridation, the sapphire substrates were degreased in acetone and iso-propanol for 10 min, then the substrates were rinsed in de-ionized water. After loading into the reactor, the substrates were thermally cleaned at 1050°C under 3l/min hydrogen gas ( $H_2$ ) for 10 min.

Commonly, as-received sapphire surface is oxidized due to exposure and hence has O-termination. It is well-known that sapphire tends to be terminated by an Al-atomic layer in reductive atmosphere, i.e. under  $N_2$  or  $H_2$  condition [94, 108]. Thus, it is expected that after the thermal cleaning at 1050°C under  $H_2$  the O-terminated surface was completely removed and changed to the stable Al-terminated surface (or Al-polarity).

### 4.2.1 *In-situ* monitoring of nitridation

The nitridation process of different sapphire surfaces was monitored using the *in-situ* SE (Fig. 4.3).  $\tan \Psi$  transient, which is most sensitive to surface chemistry [79], was used to monitor the changes on the layer surface.  $\cos \Delta$  transient is sensitive to surface roughness and layer thickness [79].  $\tan \Psi$  showed a similar trend for the nitridation process independent of substrate orientation or temperature. Figure 4.3 shows transients

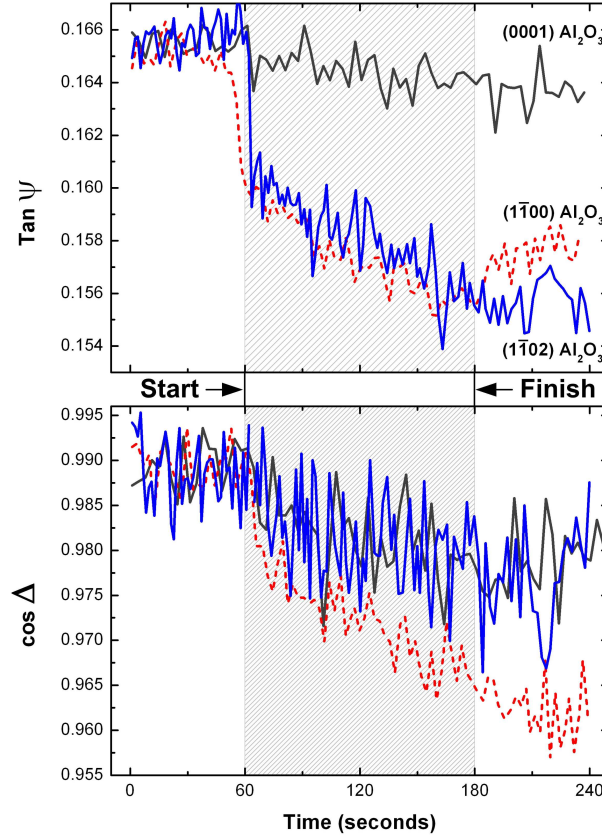


**Figure 4.3:** *In-situ* ellipsometric transients (at 5 eV) during 2 min nitridation at 1050°C on *a*-, *c*-, and *m*-plane sapphire. The spectra were taken with an incident angle of  $\sim 67.5^\circ$ . “Start” and “Finished”: switching on and off  $\text{NH}_3$ , respectively.

of the nitridation processes on sapphire substrates with different surface orientation at 1050°C.  $\tan \Psi$  changed similar after introducing  $\text{NH}_3$ , indicating the formation of a nitridation layer for all samples.

The nitridation processes were faster on *a*- and *m*-plane sapphire than on *c*-plane sapphire. This can be seen best in the  $\cos \Delta$  transients (Fig. 4.3 (bottom)). One reason is due to the difference between the number of Al-atoms of different sapphire surfaces (i.e., about  $2.6 \times 10^{15}$  atoms/cm<sup>2</sup> on the *a*-plane sapphire surface and  $2.2 \times 10^{15}$  atoms/cm<sup>2</sup> on the *c*-plane sapphire surface). Thus, more Al-atoms are exposed on the surfaces to N-species, which enhances the rate of reactions. Also, the faster nitridation compared to *c*-plane sapphire might be related to the different dangling bonds at all the surfaces. The surface with higher dangling bond density will be able to adsorb more N-species. In fact, Al-terminated atoms at the *a*- and *m*-plane

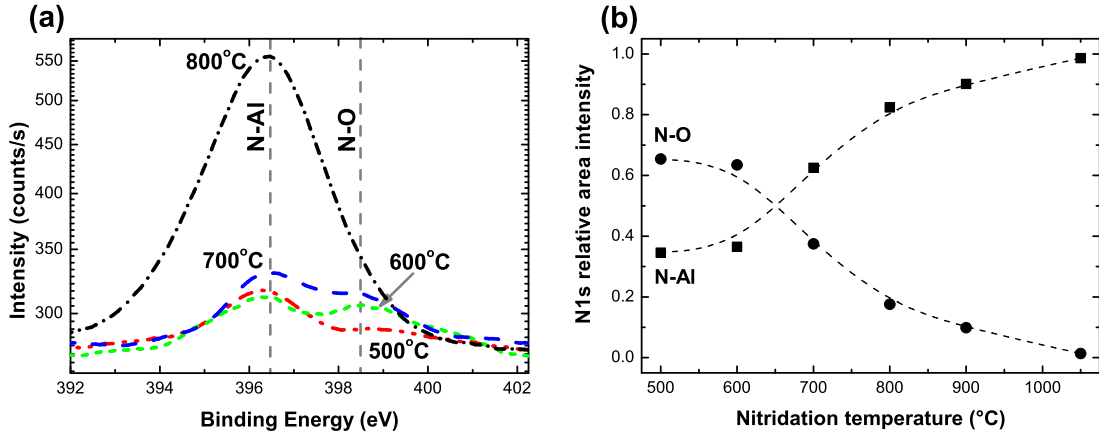


**Figure 4.4:** (a) The N 1s XPS results of *c*-plane sapphire substrates after 2 min nitridation at different temperatures. The XPS spectra were normalized to Al(KLL) Auger transition at 1387.3 eV kinetic energy. The XPS spectra were measured by Daria Skuridina at Technical University of Berlin.

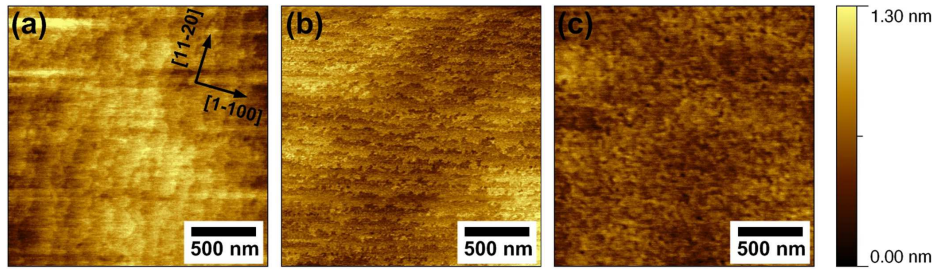


**Figure 4.5:**  $2\ \mu\text{m} \times 2\ \mu\text{m}$  AFM images of *c*-plane sapphire substrates nitridated at different temperatures (a) 700°C, (b) 800°C, and (c) 1050°C for 2 min.

surfaces of sapphire have two dangling bonds since they bond only to two O-atoms underneath, compared to one dangling bond of Al-terminated atoms at the *c*-plane surface, which are bound to the three O-atoms underneath.

### 4.3 Surface properties of the nitridation layer

To investigate N-incorporation into the *c*-plane surface of sapphire, we analyzed the N 1s core level emission of the nitridation layers by XPS (measured by Daria Skuridina at Technical University of Berlin). For this, a series of *c*-plane sapphire substrates was thermally cleaned at 1050°C, and then nitridated at different temperatures from 500°C to 1050°C for 2 min (see AFM images ( $2\ \mu\text{m} \times 2\ \mu\text{m}$ ) of the samples in Fig. 4.5). After

### 4.3. Surface properties of the nitridation layer

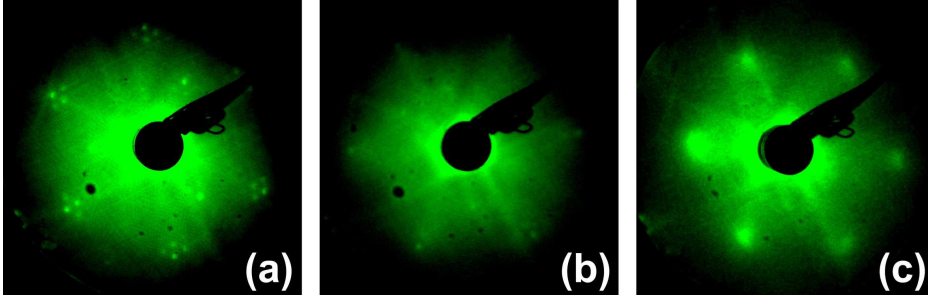


**Figure 4.6:** LEED patterns of sapphire nitridated at different temperatures (a) 500°C, (b) 800°C, and (c) 1050°C for 2 min. The LEED patterns were measured at a beam energy of  $\approx 103$  eV by Daria Skuridina at Technical University of Berlin.

transferring the samples to an ultra-high vacuum (UHV) chamber, they were annealed at 350°C for 10 min to remove contaminations. XPS measurements were performed for all samples at normal emission parallel to the  $[0001]_{\text{sapphire}}$  direction. Monochromated  $\text{AlK}\alpha$  ( $h\nu = 1486.7$  eV) radiation was used as an X-ray source.

The valence band spectra of the nitridation layers consist of two main components N-Al (at  $\sim 397.9$  eV) and N-O (at  $\sim 399.6$  eV). Figure 4.4 shows the XPS spectra and relative area intensities of the N 1s XPS peaks of N-Al and N-O as functions of sapphire nitridation temperatures. The relative area intensity of the N 1s XPS peak of N-Al increases with increasing nitridation temperatures, while the relative area intensity of the N 1s XPS of N-O decreases. The significant domination of N-O peak below 800°C indicates that at those temperatures no full nitridation was achieved.

Low energy electron diffraction (LEED, measured by Daria Skuridina at Technical University of Berlin) directly performed after the annealing shows  $1 \times 1$  hexagonal patterns (Fig. 4.6). From the calculations performed on the LEED patterns, a lattice constant of  $\sim (0.32 \pm 0.06)$  nm was found, which is in good agreement with the  $a$ -lattice constant of AlN [29]. This lattice constant indicates the growth of nearly relaxed AlN single crystal on sapphire with a wurtzite structure. In-plane relationship of AlN with respect to  $c$ -plane sapphire is  $[1\bar{1}00]_{\text{AlN}} \parallel [11\bar{2}0]_{\text{sapphire}}$  and  $[0001]_{\text{AlN}} \parallel [0001]_{\text{sapphire}}$ .

The additional spots in the LEED pattern of the 500°C nitridated sample might be due to the growth of amorphous  $\text{AlN}_x\text{O}_y$  at that low temperature. Furthermore, the spots of the LEED patterns of the samples nitridated at higher temperatures are weaker and more diffuse than the spots of the lower nitridated temperature samples, indicating an increase of surface roughness of the nitridation layers with increasing

		Rough surface		Smooth surface		Many orientations					
Temp. (°C)	Sapphire	1050	1000	900	850	800	750	700	650	600	500
(11-20) a-plane	(000-1)	(000-1)	(000-1)	(000-1)	(000-1)	(000-1)	(000±1)	(000±1)	(000+1)	(000+1)	(000+1)
(0001) c-plane	(0001-)	(000-1)	(000-1)	(000-1)	(000-1)	(000-1)	(000-1)	(000-1)	(000-1)	(000+1)	(000+1)
(10-10) m-plane	(10-1-3) semipolar	many	many	many	many	many	many	many	many	many	many
(10-12) r-plane	many	many	many	many	(11-20) a-plane	many	many	many	many	many	many

**Figure 4.7:** The effects of nitridation temperature on the growth orientation, the surface morphology, and the polarity of InN layers grown on differently oriented sapphire substrates. The nitridation time was 2 min.

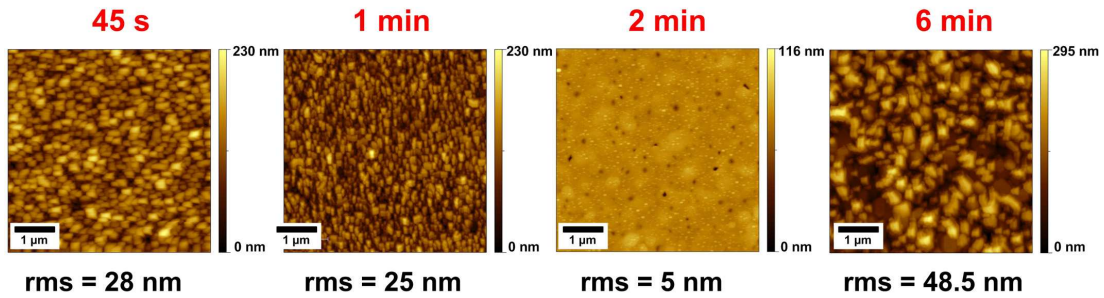


**Figure 4.8:**  $5\ \mu\text{m} \times 5\ \mu\text{m}$  AFM images of the InN layers grown on *c*-plane sapphire nitridated at  $1050^\circ\text{C}$  for 45 s to 6 min.

nitridation temperature. However, all the nitridated *c*-plane sapphire samples showed root-mean square (RMS) values smaller than  $0.2\ \text{nm}$  ( $2\ \mu\text{m} \times 2\ \mu\text{m}$ ), as shown in Fig. 4.5.

#### 4.4 Effects of nitridation on InN growth

The nitridation affects the properties of the grown layer (i.e., crystallinity, electrical and optical properties) which are mainly determined by defects (i.e., their type and density), crystallite grain size, and morphology. The effects of nitridation time from 30 s to 10 min at  $1050^\circ\text{C}$  on electrical properties of InN showed that a shorter nitridation time ( $\leq 2\ \text{min}$ ) resulted in a lower density of screw dislocations, leading to higher electron mobilities and lower carrier concentrations of InN [83].

The effects of nitridation temperature on InN layers grown on sapphire substrates

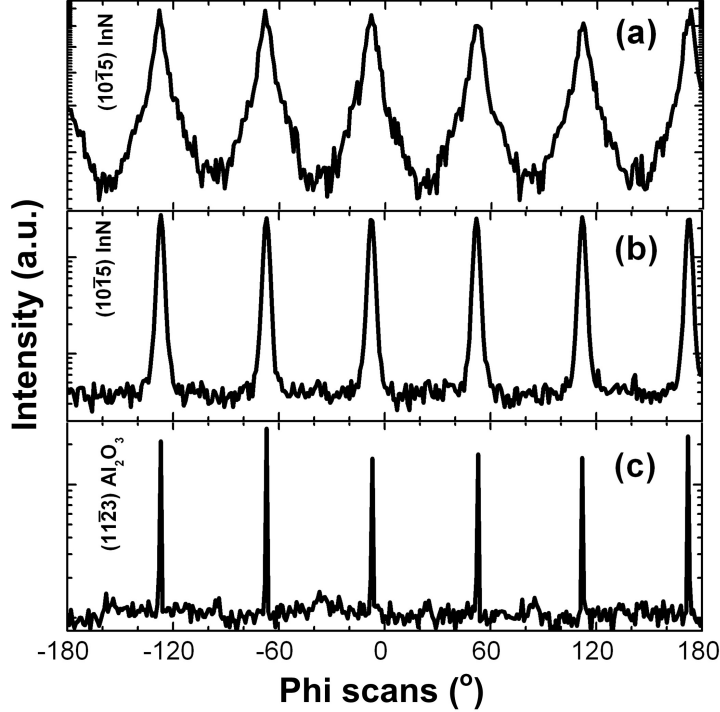


**Figure 4.9:** XRD  $\phi$ -scans of (c) the  $\{11\bar{2}3\}$  reflection of  $c$ -plane sapphire and of the  $\{10\bar{1}5\}$  reflection of InN layers grown on  $c$ -plane sapphire nitridated at (a) 1050°C and (b) 600°C.

with different surface orientations showed strong effects not only on the growth orientation but also on the surface morphology and the polarity of InN layers (Fig. 4.7). Sapphire nitridation time strongly affects the surface morphology and the growth orientation of InN layers, a shorter nitridation time (about 2 min) leads to a growth of smoother layer, while a longer time (about 4 min) leads to a growth of rougher layer (Fig. 4.8).

The crystallinity and in-plane orientation of InN layer can be checked by several methods, such as by using X-ray diffraction (XRD) or by using electron transmission microscopy to examine the structural properties of layer and substrate. Figure 4.9 shows skew-symmetric XRD  $\phi$ -scans of the  $\{10\bar{1}5\}$  reflection of  $c$ -plane InN layers grown on sapphire nitridated at 1050°C (Fig. 4.9(a)) and at 600°C (Fig. 4.9(b)) with respect to the  $\{11\bar{2}3\}$  reflection of sapphire (Fig. 4.9(c)). Six sharp  $\phi$ -scan peaks of the  $c$ -plane InN layers with exactly 60° intervals confirm a single-domain wurtzite structure with the six-fold symmetry.

As shown in Fig. 4.11(a), N-atoms will bind to the Al-atoms of the sapphire surface

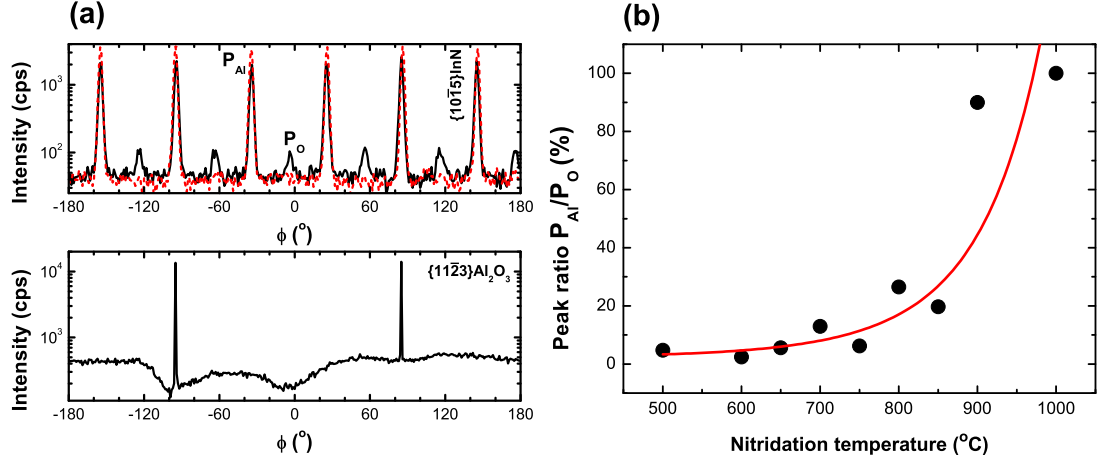


**Figure 4.10:** (a) XRD  $\phi$ -scans of the  $\{10\bar{1}5\}$  reflection of InN layers grown on  $a$ -plane sapphire nitridated (top) at 800 $^\circ C$  (black solid-line) and at 1000 $^\circ C$  (red dashed-line) and of the  $\{11\bar{2}3\}$  reflection of  $a$ -plane sapphire (below). (b) Peak ratios of  $P_{Al}/P_O$  plotted as a function of nitridation temperature.

forming a unit cell rotated by 30 $^\circ$  to the unit cell of sapphire [96], leading to a relationship of  $[1\bar{1}00]_{InN} \parallel [11\bar{2}0]_{sapphire}$  and  $[0001]_{InN} \parallel [0001]_{sapphire}$ . The 30 $^\circ$  rotation of  $c$ -plane InN with respect to  $c$ -plane sapphire occurs to reduce the lattice constant mismatch; the mismatch would be 30% without this rotation (Table 3.3).

The effects of nitridation on the crystallite rotation can be even more significant when growing InN layers on  $a$ -plane sapphire (Fig. 4.10(a)). When the nitridation on  $a$ -plane sapphire is incomplete (i.e., at  $\leq 850^\circ C$ ) two crystallite domains rotated by 30 $^\circ$  to each other are observed. The stronger one (noted as  $P_{Al}$ ) is  $[1\bar{1}00]_{InN} \parallel [0001]_{sapphire}$  and  $[11\bar{2}0]_{InN} \parallel [1\bar{1}00]_{sapphire}$  (right-hand side in Fig. 4.11(b)), and the weaker one (noted as  $P_O$ ) is  $[11\bar{2}0]_{InN} \parallel [0001]_{sapphire}$  and  $[1\bar{1}00]_{InN} \parallel [1\bar{1}00]_{sapphire}$  shown left-hand side in Fig. 4.11(b). A full nitridation (at  $\geq 900^\circ C$ ) produces only a single domain of InN with  $[1\bar{1}00]_{InN} \parallel [0001]_{sapphire}$  and  $[11\bar{2}0]_{InN} \parallel [1\bar{1}00]_{sapphire}$  (the  $P_{Al}$  peaks). The ratio of  $P_{Al}/P_O$  peak intensity increases with increasing nitridation temperatures (Fig. 4.10(b)), above 900 $^\circ C$  nitridation temperature, the layer is single phase with only  $P_{Al}$  rotation.

The full width at half maximum (FWHM) values of the  $\{10\bar{1}5\}$  reflection of  $c$ -plane InN is also related to the in-plane alignment of crystal structures. The narrower FWHM relates to the better in-plane alignment of the InN samples. Indeed, the FWHM values of the  $\{10\bar{1}5\}$  reflection of the InN layers grown on  $c$ - and  $a$ -plane sapphire decrease with increasing nitridation temperatures (Fig. 4.12).

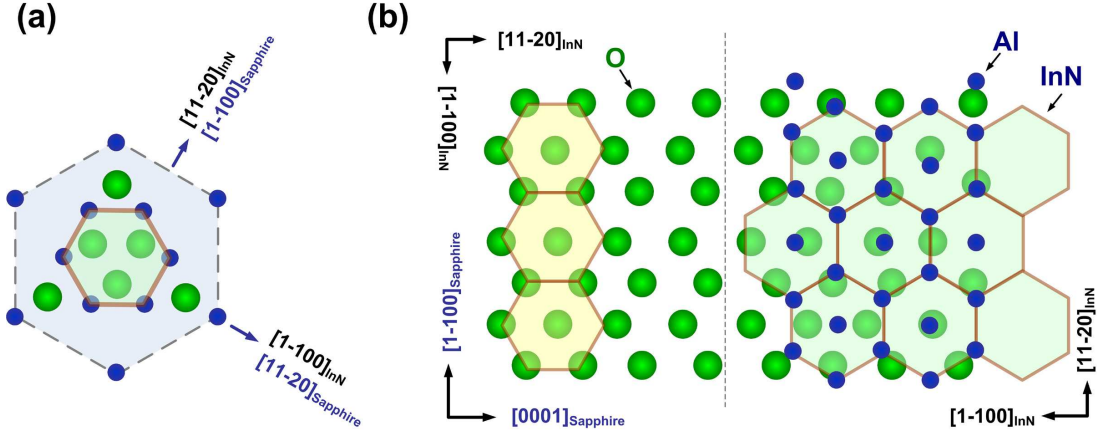


**Figure 4.11:** Resulting in-plane atomic structures of InN on (a) *c*-plane and (b) *a*-plane sapphire. The unit cell of InN on *c*-plane sapphire was rotated by 30° with respect to the unit cell of sapphire. In case of InN on *a*-plane sapphire (b), InN unit cells might have two different rotations, which are rotated by 30° with respect to each other.

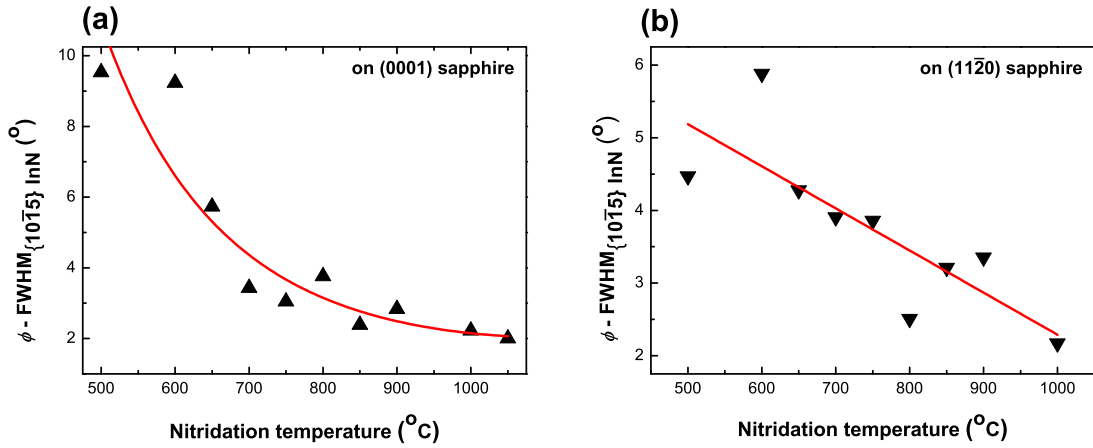


**Figure 4.12:** FWHM values of XRD  $\phi$ -scans of the  $\{10\bar{1}5\}$  reflection of InN layers grown (a) on *c*-plane sapphire ( $\Delta$ ) and (b) on *a*-plane sapphire ( $\nabla$ ) as functions of nitridation temperature. The FWHM values of the InN layers grown on *a*-plane sapphire were estimated from the peak P<sub>Al</sub> (Fig. 4.10(a)).

### 4.5 Chapter summary

Sapphire nitridation with ammonia at different temperatures was studied by *in-situ* ellipsometry (SE), X-ray photoelectron spectroscopy (XPS), and low-energy electron diffraction (LEED). LEED patterns showed the formation of wurtzite AlN on the surface of nitridated *c*-plane sapphire substrates. The N-incorporation into the sapphire surface drastically increases with increasing nitridation temperatures as confirmed by SE and XPS.

The effects of nitridation on InN layers simultaneously grown on *c*- and *a*-plane sapphire substrates nitridated from 500 - 1050°C for 2 min were investigated. InN layers grown on *c*-plane sapphire had only one crystallite rotation of  $[1\bar{1}00]_{\text{InN}} \parallel [11\bar{2}0]_{\text{sapphire}}$  and  $[0001]_{\text{InN}} \parallel [0001]_{\text{sapphire}}$ . This indicates the *c*-plane InN unit cell was rotated 30° with respect to the *c*-plane sapphire unit cell.

In contrast, InN layers simultaneously grown on *a*-plane sapphire had two different crystallite rotations dependent on nitridation temperatures. Nitridation below 900°C led to growth of InN layers with  $[11\bar{2}0]_{\text{InN}} \parallel [0001]_{\text{sapphire}}$  and  $[1\bar{1}00]_{\text{InN}} \parallel [1\bar{1}00]_{\text{sapphire}}$  ( $P_{\text{O}}$  rotation), and  $[1\bar{1}00]_{\text{InN}} \parallel [0001]_{\text{sapphire}}$  and  $[11\bar{2}0]_{\text{InN}} \parallel [1\bar{1}00]_{\text{sapphire}}$  ( $P_{\text{Al}}$  rotation). The formation of two crystallite rotations is due to the *c*-plane InN unit cell matches to both O-hexagons of the *a*-plane sapphire surface to form  $P_{\text{O}}$  rotation and Al-hexagons to form  $P_{\text{Al}}$  rotation. Nitridation above 900°C, only  $P_{\text{Al}}$  rotation remains.

For both InN layers grown on *c*- and *a*-plane sapphire, it was found that 2 min nitridation at 1050°C led to the best InN layers (smoothest surface morphology and lowest twist angle). The nitridation temperatures above 800°C for 2 min improved the surface morphology of the InN layers, while lower nitridation temperatures resulted in incomplete nitridation leading to rougher surface morphology.

## 4.5. Chapter summary

---

## Chapter 5

# Polar (0001) InN with N- and In-polarity

InN layers with different polarities (N-(000 $\bar{1}$ ) and In-(0001) polarity) have different growth (e.g., growth rate and growth window) as well as material properties (e.g., surface morphology and electrical property). This chapter deals with the growth of *c*-plane InN layers on different substrates such as *a*-plane (11 $\bar{2}$ 0), *c*-plane (0001) sapphire, and *c*-plane GaN templates deposited on *c*-plane (0001) sapphire. Polarity determination, polarity control of the layers grown directly on sapphire, and the material properties of the InN layers with the different polarities will be compared.

### 5.1 Polarity determination

To enhance the performance of III-nitride based devices, smooth interfaces in heterostructures are needed. For example GaN and AlN, Ga-/Al-polar layers show smoother surface morphology than N-polar layers [97, 98]. In contrast to GaN and AlN, N-polar InN layer shows smoother surface morphology than In-polar layer.

Similar to GaN and AlN, there are several different methods which are used to determine the polarity of InN layers, such as high-resolution transmission electron microscopy (HR-TEM) [99], convergent beam electron diffraction (CBED) [100, 101], chemical wet-etching (i.e., using potassium hydroxide (KOH) solution [101]), and coaxial impact collision ion scattering spectroscopy (CAICISS) [102]. Since the surface of InN is very easily etched in hydrogen environment, the polarity of InN layer can be

determined by hydrogen-irradiation [103]. Recently, a sensitivity of valence band (VB) X-ray photoelectron spectroscopy (XPS) spectra to the polarity of InN was found, the peak-height in valence band of InN [104]. And XPS results showed good agreements with KOH wet-etching and CBED results [101, 104]. In this thesis, chemical KOH wet-etching and XPS are the main methods used for polarity determination of InN.

### 5.1.1 KOH wet-etching

Chemical KOH wet-etching for the polarity determination of III-nitride layers is a destructive, simple, and fast method. By comparing changes in thickness and surface morphology of III-nitride layers before and after wet-etching, one can derive the polarity of the layers. In principle, group III-polar layers are more inert to chemical wet-etching than N-polar layers. For example, In-polar InN layer will be etched slowly in KOH solution, resulting in unchanged thickness and surface morphology, while N-polar InN layer will be etched fast, resulting in a major change of layer thickness and surface morphology.

The KOH solution decomposes to  $K^+$  cations and  $OH^-$  anions at room temperature. Thus, KOH serves as a source of  $OH^-$ , a highly nucleophilic anion that attacks and breaks the covalent bonds of III-nitride materials.

In contrast to GaN and AlN, the growth of InN is normally performed at a much lower temperature (i.e., 400-600°C), and with a much higher V/III ratio (i.e., 15000-25000). Due to the very low decomposition rate of  $NH_3$  at that temperature range, the growth process is still based on an In-rich growth condition, leading to an In-terminated surface (or In-adlayers on the surface) for all samples with different polarities. The In/N ratio on the layer surface containing In-adlayers is certainly larger than 1.

To etch an InN layer,  $OH^-$  anions have to break In-N bond. When an InN layer is being etched in KOH solution,  $OH^-$  easily removes the surface In-adlayers. As aforementioned, the different polarities mean In-/N-atoms on the topmost of the bare-layer surface. In- and N-atoms have different signs of electron charge, a positive charge for In-atom and a negative charge for N-atom. When an InN layer has In-polarity, this means that each topmost In-atom will bond to three underneath N-atoms, leading this bonding configuration to have a triple negative charge (Fig. 5.1(a)). When  $OH^-$  anions reach the surface of an In-polar InN layer, the surface will repel  $OH^-$  anions due to the same negative charge, resulting in an unchanged surface morphology. In the case of

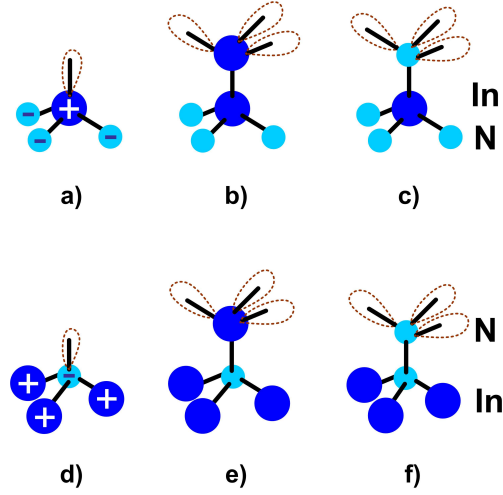


**Figure 5.1:** Dangling bond setups of In-polar InN layers with (a) bare surface, (b) In-terminated surface, and (c) N-terminated surface. And the dangling bond setups N-polar InN layers with (d) bare surface, (e) In-terminated surface, and (f) N-terminated surface. The dashed lines indicate dangling bonds.

an N-polar InN, each atop N-atom bonds to three underneath In-atoms, resulting in a triple positive charge (Fig. 5.1(d)). Thus,  $\text{OH}^-$  anions will be attracted to the surface and break In-N bonds.

Despite the fast polarity determination, KOH wet-etching method can be only used to check the polarity of polar  $c$ -plane InN and is very indirect, especially enhanced etching at defects can lead to mis-interpretations. To check the polarity of other growth orientations of InN layers, such as semi- and non-polar orientations, one has to use another method. In this thesis, XPS is used as an alternative method to check the polarity of InN layers with different surface orientations. Compared to KOH wet-etching method, XPS method is a non-destructive technique. Furthermore, XPS gives an additional information about the sample such as elemental composition, as well as chemical and electronic states.

### 5.1.2 Valence band emission in X-ray photoelectron spectroscopy

Due to the energies of the detected electrons, XPS measures the surface with a maximum depth of  $\sim 10$  nm [105]. The valence band (VB) spectrum (within a range of binding energy from 0 eV to 10 eV) of polar InN consists of two dominating peaks (Fig. 5.2) at  $\sim 3.5$  eV (noted as peak A) and  $\sim 6.5$  eV (noted as peak B). Different back-

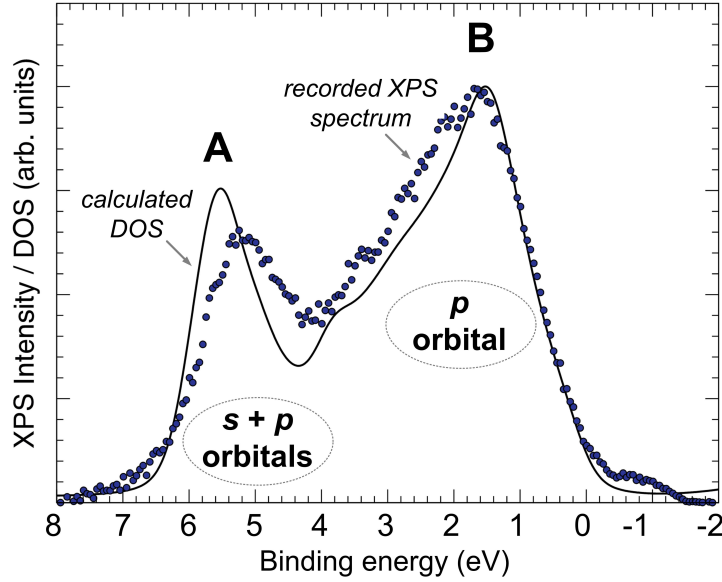


**Figure 5.2:** Valence band spectra of wurtzite InN: calculated DOS (solid line) and recorded spectrum ( $\circ$ ) [106].

ground doping, defects, and surface accumulations can cause the slight shifts of those peak positions. The peak A mainly results from the  $p$ -like VB states, while the peak B has a partially contribution of the  $s$ -like states besides the  $p$ -states [107]. The relative intensities of the peaks A and B (or peak ratio of  $R_{A/B}$ ) were correlated with the polarity of the polar InN layer [104]. If the peak intensity of peak A (or B) is higher (or lower) than that of peak B (or A), then the layer has an N-polar orientation ( $R_{A/B} = 1.2$  [104]) (or an In-polar orientation,  $R_{A/B} = 0.78-0.8$  [104]). InN layer with mixed polarity (including both N- and In-polar orientations for one sample) exhibits similar peak intensities of the peaks A and B ( $R_{A/B} = 0.98$  for  $\sim 50\%$  mixed polarity estimated by KOH wet-etching [101, 104]).

All the XPS spectra in this thesis were measured at normal emission (measured by Daria Skuridina at Technical University of Berlin), parallel to the  $[0001]_{\text{InN}}$  direction (in-plane wave vector  $k_{\parallel[0001]} = 0$ ). Monochromated  $\text{AlK}_{\alpha}$  ( $h\nu = 1486.7 \text{ eV}$ ) radiation was used as an X-ray source. Before recording the XPS spectra, all InN samples were annealed at  $450^{\circ}\text{C}$  for 10 min under ultra-high vacuum (UHV) environment to desorb contaminations (oxides, carbon,...) from the surface. The energy scale of the InN samples was calibrated using the Fermi-edge of the molybdenum sample plate that was in a direct contact with the measured sample ( $E_{\text{F}} = 0 \text{ eV}$ ).

As mentioned before, In-adlayers always exist on the surface of an as-grown InN layer. However, the XPS measurements were performed using a high energy of the incident X-rays ( $h\nu = 1486.7$  eV) and thus high kinetic energy of ejected valence band (VB) photoelectrons ( $> 1$  keV). Hence, the photoelectron escape depth is relatively large, allowing the features of the bulk density-of-state to dominate the XPS spectra over the surface related features.

Due to the different configurations of dangling bonds, In- and N-polar InN layers show different surface states, but all the surface states were found to be located above the conduction band maximum (CBM) of InN [57]. This phenomenon differs from the surface states of polar GaN, where the surface states of GaN are below the CBM of GaN [57]. Since In-adlayers are present on the surfaces of all InN samples (without any treatment), the In-adlayers serve as electron accumulations that lead to Fermi-level pinning. First-principles calculations based on density functional theory (DFT) showed occupied surface states at 0.6 eV for In-polar (0001) InN ( $2\times 2$  unit cells), and at 0.3 eV for N-polar (0001) InN ( $2\times 2$  unit cells) [57].

## 5.2 Polarity control of InN by sapphire nitridation

The polarity of InN layer grown on foreign substrates, especially on the other group III-nitrides such as GaN and AlN, is strongly depended on the polarity of the substrates. For example, InN layer grown on Ga-/N-polar GaN (or Al-/N-polar AlN) templates (either free-standing layers or those layers grown on other substrates, i.e., sapphire) will have the same polarity as the templates.

Controlling the polarity of InN layer grown directly on sapphire is a little bit difficult since sapphire is not a member of the group III-nitrides. Due to the differences between the lattice constants of III-nitrides and sapphire as shown in Table 3.3, a nitridation process is generally employed in order to reduce the strain effects between III-nitrides and sapphire. The effects of *c*-plane sapphire nitridations on the growth of *c*-plane InN layers have been investigated at 1050°C for 45 s up to 6 min. The best quality of *c*-plane InN layer was produced for 2 min of sapphire nitridation (Section 4.4). To investigate the effect of nitridation temperature on the polarity of *c*-plane InN layers, all the InN layers were grown on *a*- and *c*-plane sapphire substrates after nitridated at different

## 5.2. Polarity control of InN by sapphire nitridation

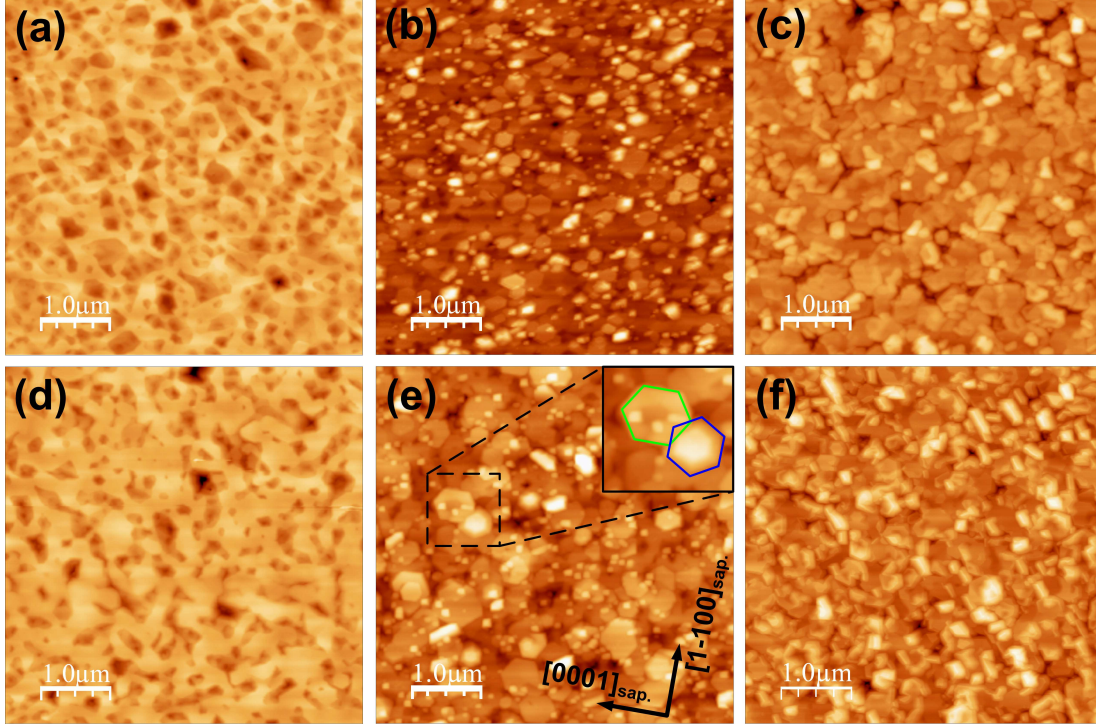


**Figure 5.3:**  $5\ \mu\text{m}\times 5\ \mu\text{m}$  AFM images of the InN samples ( $\approx 250\ \text{nm}$ ) grown directly on  $c$ -plane sapphire (top) and on  $a$ -plane sapphire (bottom) nitridated at  $900^\circ\text{C}$ ,  $750^\circ\text{C}$ , and  $600^\circ\text{C}$ , respectively. The  $Z$ -height scale is  $200\ \text{nm}$ . The *inset* of (e) shows two crystallite structures rotating  $30^\circ$  with respect to each other.

temperatures for 2 min nitridation. The growth parameters of the InN layers on  $a$ - and  $c$ -plane sapphire nitridated at different temperatures were shown in Section 3.5.

Atomic force microscopy (AFM) performed in contact mode (Fig. 5.3) was used to investigate morphology changes on the InN layers dependent on nitridation temperatures. The InN layers on  $a$ - and  $c$ -plane sapphire substrates showed a similar surface morphology. The morphology of the InN layers changed from a flat (above  $800^\circ\text{C}$  nitridation), over a mixture between flat and hexagonal facets ( $700^\circ\text{C}$  -  $750^\circ\text{C}$  nitridation), to grainy (below  $650^\circ\text{C}$  nitridation) as shown in Fig. 5.3.

Hexagonal crystallite structures rotated  $30^\circ$  with respect to each other were observed in the InN layers on  $a$ -plane sapphire nitridated below  $900^\circ\text{C}$  shown in the *inset* of Fig. 5.3(e). These are the rotated domains that were identified by XRD (Section 4.4 and Fig. 4.10(a)). Due to the atomic arrangement on the surface of  $a$ -plane sapphire, two distinct hexagonal bonding matrices rotated by  $30^\circ$  are formed and mainly deter-

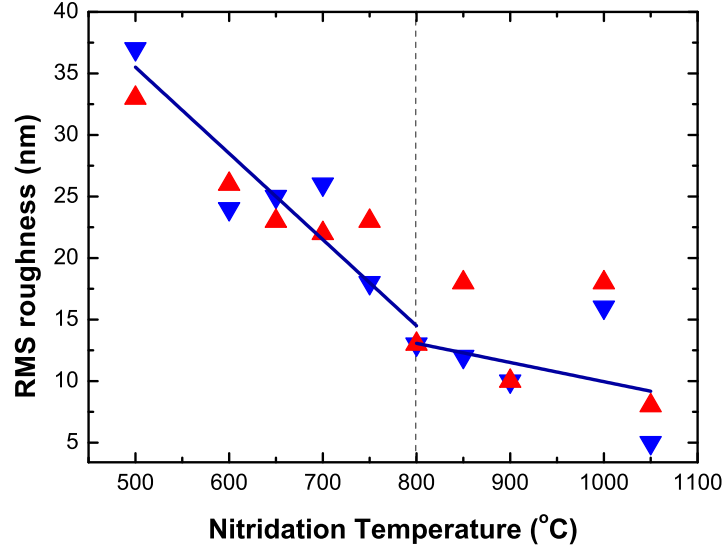


**Figure 5.4:** RMS values for a scan area of  $5\ \mu\text{m}\times 5\ \mu\text{m}$  of the InN layers grown on *a*-plane (▽) and *c*-plane (△) sapphire as a function of nitridation temperatures. Two different trend lines occur with an intersection at 800°C nitridation.

mined by the nitridation (see Section 4.4 and Fig. 4.11(b)).

For the range of nitridation temperatures from 1050°C to 500°C, the root-mean square roughness (RMS) values increased from 5 nm to 38 nm for a scan area of  $5\ \mu\text{m}\times 5\ \mu\text{m}$ . The RMS values of the InN layers on *a*- and *c*-plane sapphire plotted as functions of nitridation temperatures are shown in Fig. 5.4. The RMS values show two different trend lines, at 500-800°C and at 800-1050°C. The intersection at 800°C nitridation indicates the morphology of the InN layers was switched from grainy to flat morphology.

The VB XPS spectra of the InN samples on *c*-plane sapphire nitridated at temperatures from 600°C-1000°C are shown in Fig. 5.5. The InN layers on *c*-plane sapphire nitridated above 800°C showed a higher amplitude of the peak A than that of the peak B (leading to a peak ratio of  $R_{A/B} = 1.10-1.20$ ), which indicates N-polarity. Nitridating sapphire below 650°C resulted in the growth of In-polar InN layers (peak A < peak B and  $R_{A/B} = 0.80-0.90$ ). The InN layer grown on non-nitridated sapphire also showed In-polarity. The transition occurs for the samples with a nitridation between 700°C-750°C, when amplitude of the peak at  $\sim 6.8\ \text{eV}$  drops, leading to intensities of the peak A  $\approx$  peak B with  $R_{A/B} = 0.97-1.08$ . This transition (called as a mixed-polar window) was presumed to be the growth of mixed-polar InN layers (including both N- and In-polarity). The ratios of the peak A/peak B as a function of nitridation temper-

## 5.2. Polarity control of InN by sapphire nitridation

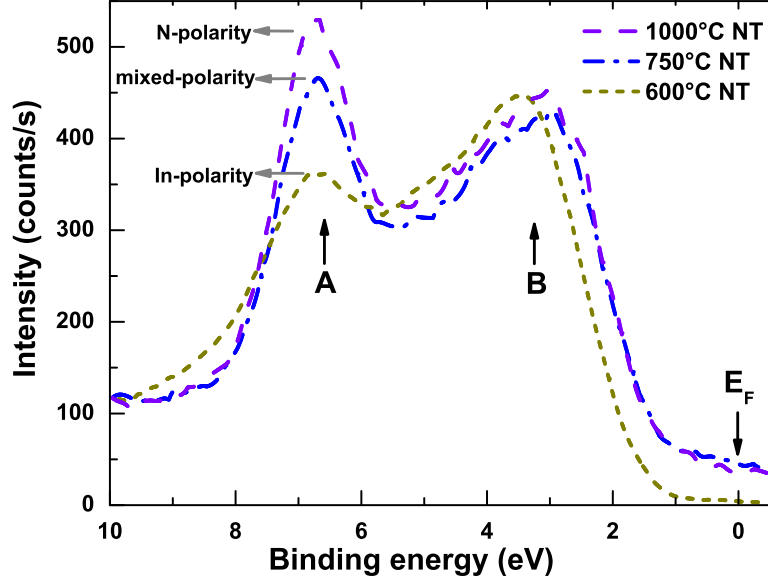


**Figure 5.5:** Valence band spectra of the InN layers grown directly on *c*-plane sapphire at different nitridation (NT) temperatures. The spectra were normalized on the right peak (noted as B). All the spectra were measured at the normal surface, parallel to the  $[0001]_{\text{InN}}$  direction. The energy scale of the InN layers was calibrated using the Fermi-edge of the molybdenum sample plate ( $E_F = 0 \text{ eV}$ ). The XPS spectra were measured by Daria Skuridina at Technical University of Berlin.

ature of the InN layers grown on *a*- and *c*-plane sapphire shown in Fig. 5.6 shows the same trends as the RMS roughness values (Fig. 5.4).

For the InN layers grown simultaneously on *a*-plane sapphire with *c*-plane sapphire, the VB spectra showed similar shapes and number of components (peaks A and B) to the InN layers grown on *c*-plane sapphire. The  $R_{A/B}$  ratio of 1.13 (Fig. 5.6) was found for the InN layer grown on *a*-plane sapphire nitridated at  $700^\circ\text{C}$ , indicating the growth of an N-polar InN layer. For the InN layer grown on *a*-plane sapphire nitridated at  $600^\circ\text{C}$ , the  $R_{A/B}$  ratio was found to be 0.92 (Fig. 5.6), this indicates the growth of an In-polar InN layer. Since those ratios do not lie in the mixed-polar window of the InN layers on *c*-plane sapphire, a mixed-polar window for the InN layers on *a*-plane sapphire was presumed to be in the nitridation range of  $600^\circ\text{C}$  -  $700^\circ\text{C}$ .

As mentioned in Section 4.2, the nitridation was faster on *a*-plane than on *c*-plane sapphire due to the higher density of the dangling bonds of Al-atoms on the *a*-surface than that on the *c*-surface of sapphire. This explains why N-polar InN layers were produced on *a*-plane sapphire at  $50^\circ\text{C}$  lower nitridation temperature.

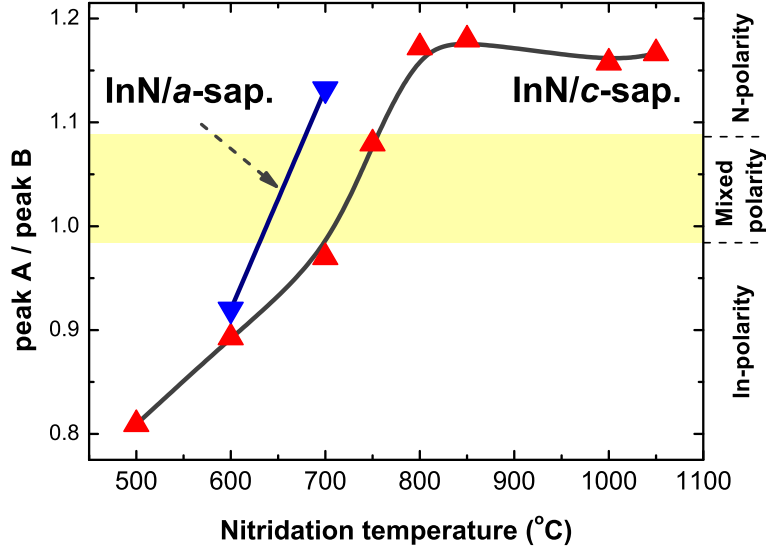


**Figure 5.6:** Ratio of the peak intensity of peak A/peak B from the VB spectra of the InN layers grown directly on *a*- ( $\nabla$ ) and *c*-plane ( $\Delta$ ) sapphire at different nitridation temperatures.

Density-functional theory calculations for *c*-plane AlN on *c*-plane sapphire showed a dependency of the polarity and the stability of AlN on growth conditions such as Al- and N-rich [108, 109]. Al-polar AlN is the most stable structure for Al-rich conditions, while N-polar AlN is the most stable structure for N-rich conditions. [109] Additionally, under N-/Al-deficient conditions, a polarity inversion might appear [109]. Recently, it was found that *c*-plane sapphire nitridated at 935°C produced N-polar AlN, while sapphire after a thermal annealing at 1070°C in hydrogen had Al-terminated surface [89].

In our case, the nitridation process at higher temperatures (e.g., 900°C) can be considered as an N-rich condition, due to increased decomposition of  $\text{NH}_3$ . This leads to the growth of N-polar AlN via nitridation. When the decomposition rate of  $\text{NH}_3$  is very low ( $< 750^\circ\text{C}$ ), the nitridation is not effective, the growth is under Al-rich condition, leading to the growth of Al-polar AlN (or  $\text{AlN}_x\text{O}_y$ ). A mixed polar AlN is produced when the decomposition rate of  $\text{NH}_3$  is increased, but the nitridation is still insufficient to produce the fully N-polar AlN. Since InN grown on GaN or AlN templates has the same polarity as the templates, i.e., In-polar InN on Ga-polar GaN. Therefore, the InN layers grown on the nitridated sapphire substrates reproduced the polarity of AlN layers by the nitridation. Overview about the effects of nitridation on the polarity of InN is summarized in Fig. 5.7.

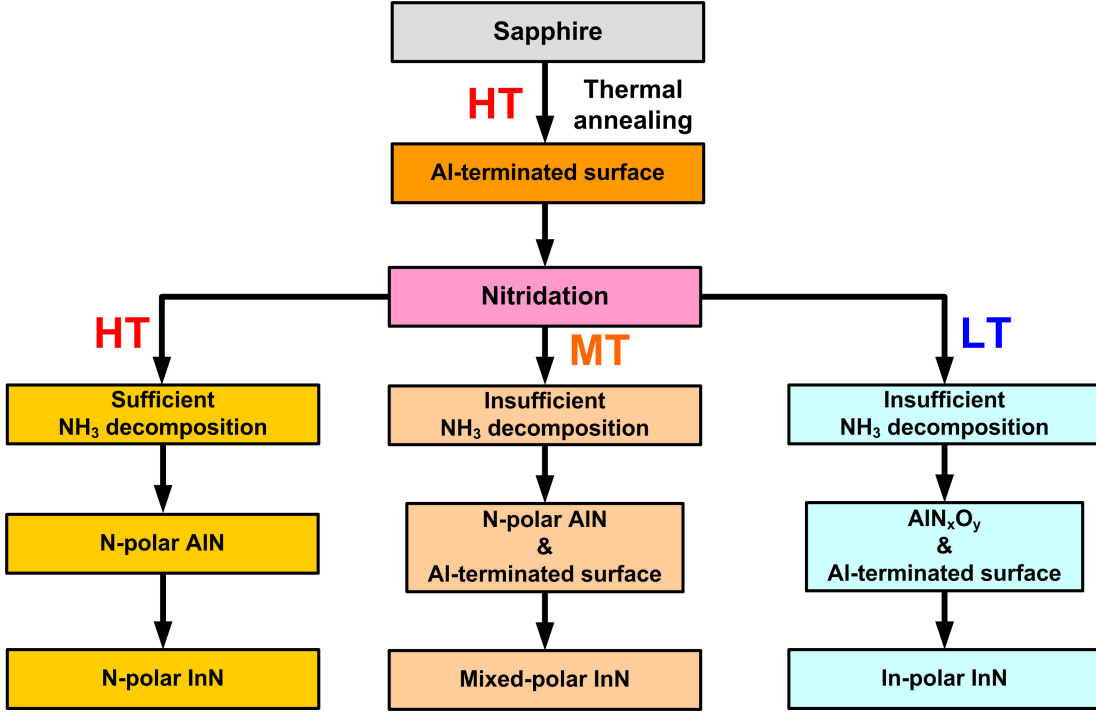


**Figure 5.7:** Flow chart of experimental observations on the polarity selection of InN layer on *c*-plane sapphire under different nitridation temperatures. HT, MT, and LT are high-, mid-, and low-temperature ranges, respectively.

Different surface morphologies of the InN layers grown at different nitridated temperatures might relate to the different polarities. In fact, N-polar InN layers showed a flat surface morphology, while In-polar layers showed a grainy morphology. The mixture of flat and hexagonal facets on the surface morphology were found for mixed-polar InN layers (Fig. 5.3).

## 5.3 Comparisons of N- and In-polar InN

### 5.3.1 Polarity

As mentioned in Section 5.1, the polarity of InN can be determined by XPS via a correlation of certain peak-heights in the InN valence band spectra. Using this technique, we determined that the InN layers ( $\sim 250$  nm) grown directly on nitridated sapphire (at  $1050^\circ\text{C}$  for 2 min) had N-polarity, and InN layers ( $\sim 300$  nm) grown on GaN had In-polarity, matching the Ga-polarity of GaN templates (Fig. 5.8). The growth param-

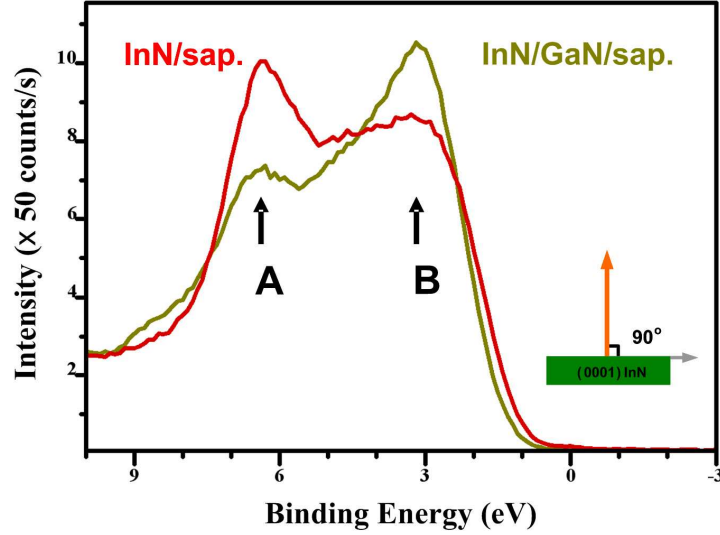


**Figure 5.8:** Valence band (VB) spectra of InN layers grown at 560°C measured at normal emissions. The spectra indicate the N-polar InN/sapphire and the In-polar InN/GaN template. The VB spectra were measured by Daria Skuridina at Technical University of Berlin.

eters of the InN layers on sapphire and the InN layers on GaN templates were shown in Section 3.5.

The polarities of the grown InN layers were additionally confirmed by KOH wet-etching (Fig. 5.9). The KOH wet-etching of the InN layer on sapphire resulted in the occurrence of small pyramid islands and holes after  $\approx 20$  min etching (Figs. 5.9(b) and (c)), while surface morphology of the InN layer on GaN template remains nearly unchanged even after  $\approx 60$  min etching (Figs. 5.9(d) and (e)). These results confirm that the In-polar InN layer is more inert and stable than the N-polar InN layer. This is in a good agreement with previous KOH wet-etching results for InN layers with the different polarities [101].

### 5.3.2 Crystallinity

Figure 5.10 shows the XRD  $\omega$ - $2\theta$  scans of the InN layers grown directly on *c*-plane sapphire and *c*-plane GaN templates. Metallic indium was found for all InN samples. The intensity of the (0002) InN reflection of the InN layers grown on GaN was as 5-6 times higher than the InN layers grown directly on sapphire, which is attributed to a higher growth rate of In-polar InN. Furthermore, full width at half maximum

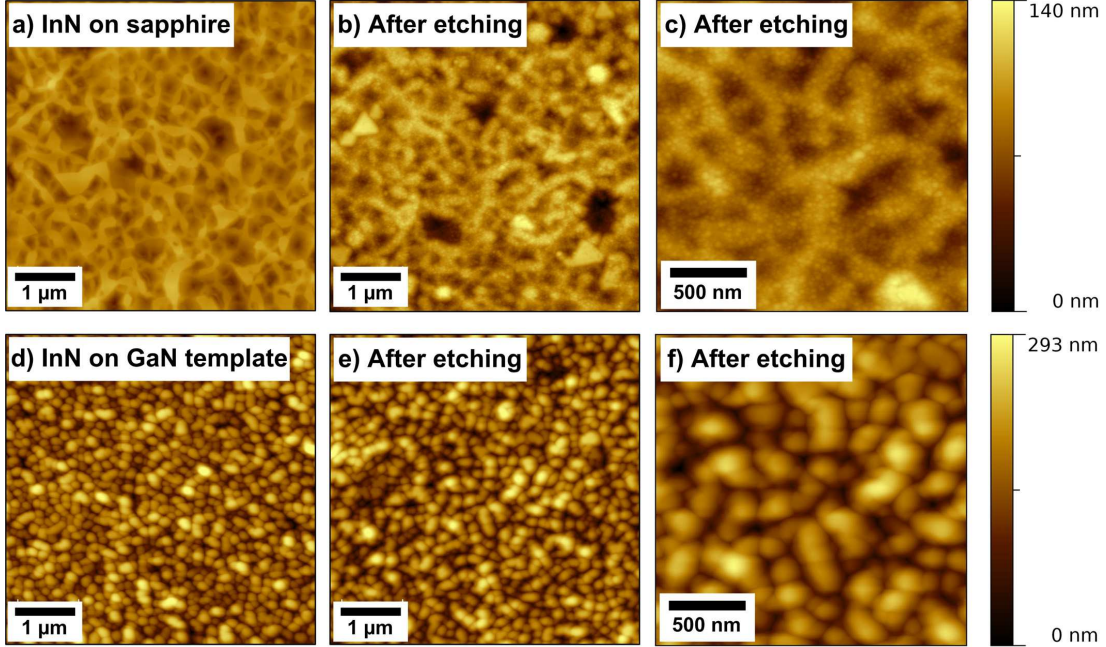


**Figure 5.9:** AFM images of (a) an as-grown InN layer ( $\approx 200$  nm) directly on sapphire, and after 30 min KOH wet-etching (b)- $5 \mu\text{m} \times 5 \mu\text{m}$  and (c)- $2 \mu\text{m} \times 2 \mu\text{m}$ , of an as-grown InN layer ( $\approx 300$  nm) on GaN template (d), after 30 min KOH wet-etching (e)- $5 \mu\text{m} \times 5 \mu\text{m}$  and (f)- $2 \mu\text{m} \times 2 \mu\text{m}$ .

(FWHM) of the symmetric (0002) InN reflection of the XRD  $\omega - 2\theta$  scans measured from the InN layers grown on sapphire decreased with increasing growth temperatures, corresponding to an improved crystallinity and increase of layer thickness. The increase of layer thickness with increasing growth temperatures might be related to the increase of surface diffusions, this will be discussed later.

In Fig. 5.10, the (0002) InN reflection of the XRD  $\omega - 2\theta$  scans of the InN layer on GaN template is shifted to the higher diffraction angle compared to no shift for the InN layer on sapphire. Table 5.1 shows the offset and FWHM values of (0002) InN reflection the InN layers grown on *c*-plane sapphire and *c*-plane GaN templates at different temperatures. The offset value of the (0002) InN reflection the InN layers was calculated as:  $\Delta = \omega_{\text{measure}} - \omega_{\text{reference}}$ . For reference, the lattice parameters were  $a = 3.545 \text{ \AA}$  and  $c = 5.703 \text{ \AA}$  for InN [29], giving an  $\omega_{\text{reference}} = 15.67^\circ$ . The shift to the higher diffraction angles of the (0002) InN reflection of the InN layers grown on GaN templates (Fig. 5.10) indicates the decrease of the InN *c*-lattice constant. Even though the reciprocal space maps show that the InN layers on GaN templates are fully relaxed,

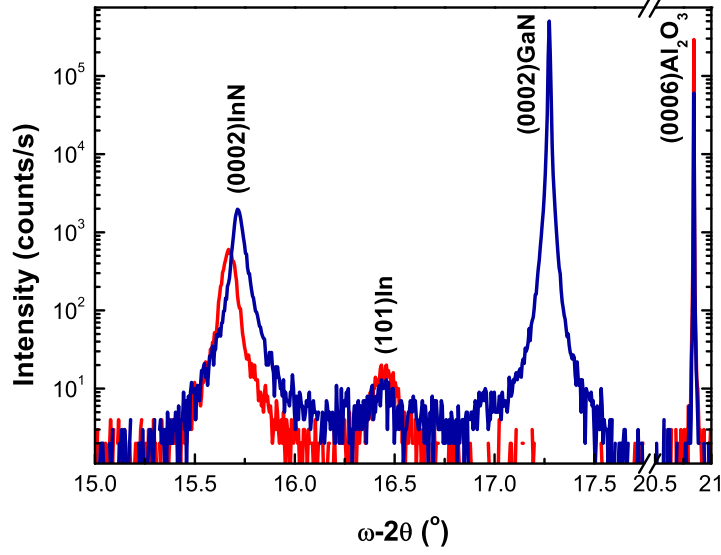


**Figure 5.10:** XRD  $\omega$ - $2\theta$  scans of the InN layer grown directly on  $c$ -plane sapphire and the InN layer on  $c$ -plane GaN at 550°C.

a residual stress is expected in the layers due to the differences of thermal expansion coefficient and lattice mismatch between InN and GaN (Table 3.3).

Raman scattering spectroscopy was carried out to further investigate the crystalline properties and stress of the InN layers by analyzing the optical phonon modes of InN. The Raman spectra were measured at Centre for Research on Ions, Materials and Photonics (CIMAP by Arantxa Vilalta-Clemente). Optical phonons consist of two different modes: longitudinal optical (LO) and transverse optical (TO) modes. Similar to wurtzite GaN and AlN (point group  $C_{6v}^4$ ), the wurtzite InN phonon modes ( $k=0$  group) are  $A_1 + E_1 + 2B_1 + 2E_2$ , where the  $A_1$ (LO),  $E_1$ (TO),  $E_2$ (high), and  $E_2$ (low) are Raman-active, and the two  $B_1$ (silent) are Raman-inactive [110]. The stress in the InN layers was analyzed by the  $E_2$ (high) phonon peak, which is not sensitive to

**Table 5.1:** Offset values ( $\Delta = \omega_{\text{measure}} - \omega_{\text{reference}}$ ) and the FWHM values of the (0002) InN reflection of the XRD  $\omega$ - $2\theta$  scans of the InN layers grown directly on sapphire or on GaN templates.

$T_{\text{growth}}$ (°C)	520	530	540	550	560
$\Delta_{\text{InN}/\text{Al}_2\text{O}_3}$ (°)	-	-0.003	0.002	0.002	0.007
FWHM (°)	-	0.061	0.071	0.058	0.040
$\Delta_{\text{InN}/\text{GaN}}$ (°)	-0.008	-0.178	-0.043	-0.043	-0.048
FWHM (°)	0.043	0.038	0.047	0.045	0.056

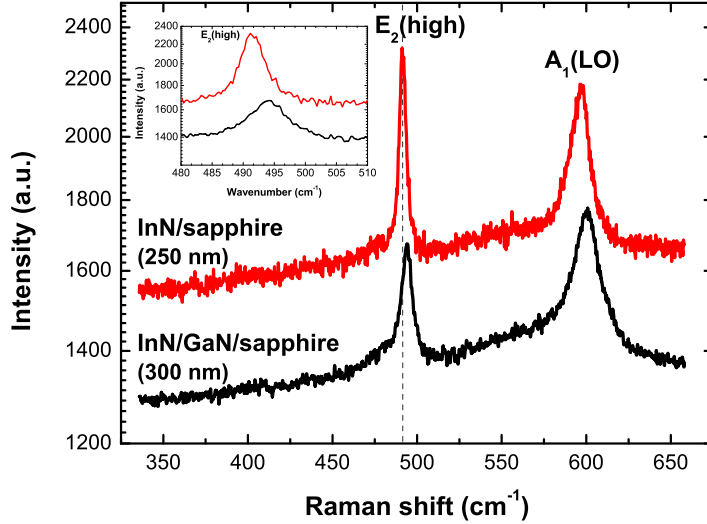


**Figure 5.11:** Raman spectra of the InN layer grown directly on *c*-plane sapphire and the InN layer on *c*-plane GaN template. The *inset* shows the  $E_2(\text{high})$  phonon peaks of the layers, indicating the blue-shift of the InN layer on GaN template compared to the InN layer on *c*-plane sapphire. The Raman spectra were measured by Arantxa Vilalta-Clemente at CIMAP, Caen, France.

any doping level of the GaN template due to its transverse optical character. In the presence of biaxial compressive stress, the  $E_2(\text{high})$  phonon mode will shift to the higher wavenumber with increasing the stress in layers. In contrast to the  $E_2(\text{high})$  mode, the  $A_1(\text{LO})$  mode is less affected by the compressive stress, but strongly affected by free carrier concentration through the coupling of the LO phonon longitudinal field with the plasmon macroscopic longitudinal field [111]. In particular the  $A_1(\text{LO})$  phonon peak shifts to a higher frequency with increasing the carrier concentration.

Figure 5.11 shows the backscattering Raman spectra of the InN layers grown on sapphire and on GaN template over a wavenumber range of 350 - 650  $\text{cm}^{-1}$  taken at room temperature. Only two phonon peaks were observed in that wavenumber range for both the InN layers grown on sapphire and on GaN template. The peaks at  $\sim 491 \text{ cm}^{-1}$  and  $\sim 596 \text{ cm}^{-1}$  refer to the  $E_2(\text{high})$  and  $A_1(\text{LO})$  modes, respectively. These frequencies are in good agreement with other Raman data for epitaxial InN layers [112, 113]. The sharp and strong  $E_2(\text{high})$  phonon peak in the Raman spectra at  $\sim 491 \text{ cm}^{-1}$  confirms that the InN layers have a wurtzite structure. This is in good agreement with the XRD result. No Raman peaks related to cubic InN were found, i.e., no TO mode at  $457 \text{ cm}^{-1}$  and no LO mode at  $588 \text{ cm}^{-1}$  of cubic InN lattice [113]. For strain-free

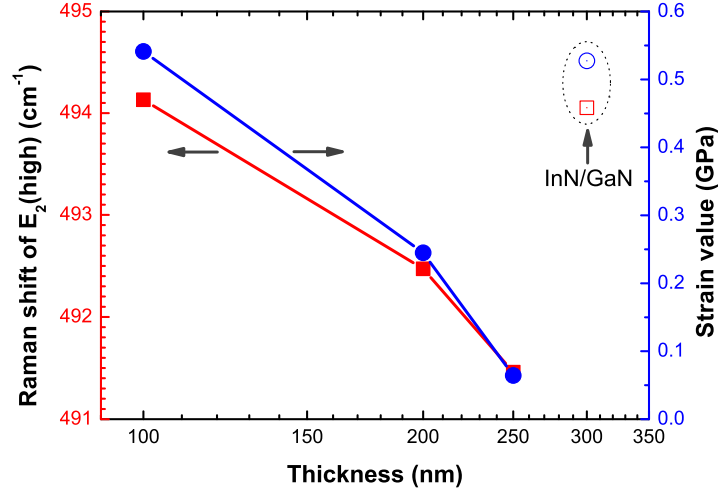


**Figure 5.12:** The shifts of the  $E_2(\text{high})$  phonon peaks and the in-plane strain values of the InN layers with different layer thicknesses grown directly on  $c$ -plane sapphire and  $c$ -plane GaN template.

InN, the  $E_2(\text{high})$  phonon peak ( $\omega E_2^{\text{strain-free}}$ ) was found at  $491.1 \text{ cm}^{-1}$  [112]. The  $E_2(\text{high})$  peak of the InN layer on sapphire was found at  $491.4 \text{ cm}^{-1}$  corresponding to a nearly free-strained layer. A slight shift of  $2.9 \text{ cm}^{-1}$  of the  $E_2(\text{high})$  mode of the InN layer on GaN template ( $494.3 \text{ cm}^{-1}$ ) confirms the residual stress in the InN layers in accordance with XRD. A compressive biaxial thermal stress is inevitably produced in the epitaxial layers perpendicular to the  $c$ -axis upon the cooling after the growth due to the differences in thermal expansion coefficient and lattice mismatch of InN, GaN, and sapphire (Table 3.3). However, it is expected that the InN layers on sapphire can themselves react to release the residual strain/stress by producing peeling-off areas (Fig. 5.19).

To investigate the effects of layer thickness on the strain state, a series of InN layers on sapphire with different layer thickness from 100-250 nm and an InN layer on GaN template with thickness of 300 nm were analyzed using Raman spectroscopy. Typical Raman spectra were shown in Fig. 5.11. For the InN layers grown on sapphire, the shift of the  $E_2(\text{high})$  phonon peak ( $\omega E_2^{\text{measured}}$ ) reduces with increasing layer thickness from  $494.1 \text{ cm}^{-1}$  (100 nm) to  $491.4 \text{ cm}^{-1}$  (250 nm). The in-plane residual strain ( $\sigma_{xx}$ ) of the InN layers was calculated by:

$$\sigma_{xx} = \frac{\omega E_2^{\text{measured}}(\text{cm}^{-1}) - \omega E_2^{\text{strain-free}}(\text{cm}^{-1})}{KH}, \quad (5.1)$$

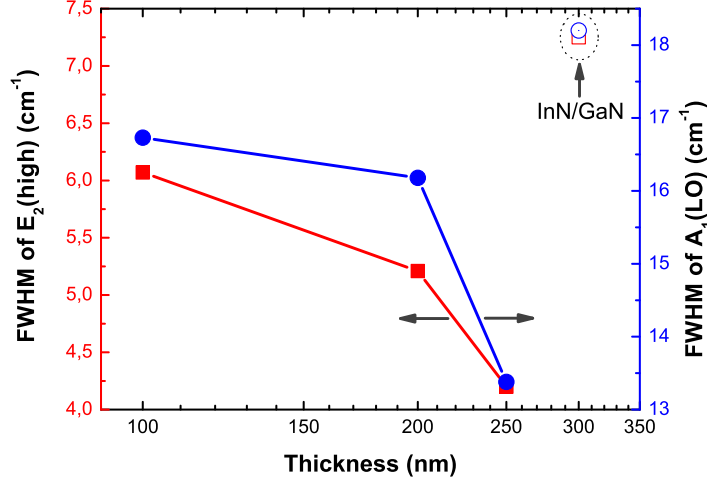


**Figure 5.13:** FWHM values of the  $E_2(\text{high})$  and the  $A_1(\text{LO})$  phonon peaks of the InN layers grown directly on  $c$ -plane sapphire and the InN layer grown on  $c$ -plane GaN template.

where  $K^H$  is the hydrostatic linear pressure coefficient which can be derived from the equation [114]:

$$K^H = -\frac{2a(C_{33} - C_{13}) + b(C_{11} + C_{12} - C_{13})}{C_{33}(C_{11} + C_{12}) - 2C_{13}^2}, \quad (5.2)$$

where  $C_{ij}$  are the stiffness constants of InN,  $a$  and  $b$  are the deformations of  $E_2(\text{high})$  phonon mode of InN. The  $K^H$  coefficient was calculated to be  $5.6 \text{ cm}^{-1}\text{GPa}^{-1}$  by using the stiffness constants:  $C_{11} = 271$ ,  $C_{12} = 124$ ,  $C_{13} = 94$ , and  $C_{33} = 200$  [115], and the deformations:  $a = -610 \text{ cm}^{-1}$  and  $b = -857 \text{ cm}^{-1}$  [112].

From Eqn. 5.1, the in-plane residual strain values of the InN layers were calculated and shown in Fig. 5.12. The reduction of the  $E_2(\text{high})$  peak shifts correlates to a reduction of the strain values of the InN layers on sapphire from 0.54 GPa to 0.06 GPa. Furthermore, the FWHM values of the  $E_2(\text{high})$  phonon peaks of the InN layers on sapphire also reduce with increasing layer thickness from  $6.0 \text{ cm}^{-1}$  to  $4.2 \text{ cm}^{-1}$ , indicating an increase of crystallinity (Fig. 5.13).

The InN layer on GaN template (300 nm) showed the same  $E_2(\text{high})$  peak shift and in-plane strain value as the InN layer on sapphire with the thickness of 100 nm (Fig. 5.12). Additionally, the FWHM value of the  $E_2(\text{high})$  phonon peak of the 300 nm InN layer on GaN template was found to be  $7.3 \text{ cm}^{-1}$ , even larger than that of the 100 nm InN layer on sapphire (Fig. 5.13). It means that even with thicker layers, the

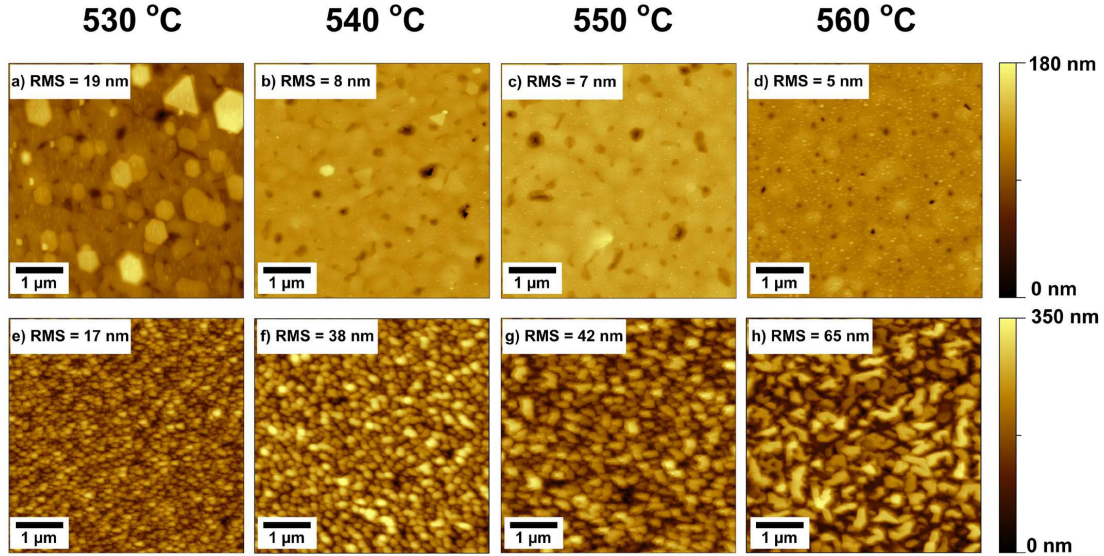


**Figure 5.14:**  $5\ \mu\text{m}\times 5\ \mu\text{m}$  AFM images and RMS roughness of the N-polar InN layers ( $\approx 200\text{-}250\ \text{nm}$ ) grown directly on *c*-plane sapphire (top) and the In-polar InN layers ( $\approx 300\text{-}350\ \text{nm}$ ) on *c*-plane GaN templates (bottom) grown at different temperatures.

crystallinity of InN layer on GaN template is worse than the one of thinner InN layers on sapphire.

### 5.3.3 Surface morphology and growth modes

The surface morphology of the as-grown InN samples were examined on  $5\ \mu\text{m}\times 5\ \mu\text{m}$  AFM images (Fig. 5.14). The InN layers grown on *c*-plane sapphire showed smoother morphology at higher growth temperatures, while the InN layers on *c*-plane GaN templates showed smoother morphology at lower growth temperatures. The smallest RMS roughness was 5 nm at the growth temperature of 560°C for the InN layer grown on sapphire, whereas at this growth temperature the RMS roughness of the InN layer grown on GaN was about 65 nm (Fig. 5.14). It is important to note that the RMS roughness value of the GaN templates was only about 1 nm for the same scan range, and hence could not cause the roughness of the In-polar InN layers. The high RMS roughness values of In-polar InN layers on GaN templates were comparable to those of In-polar InN layers on sapphire (Fig. 5.3).

Metallic indium droplets (small white dots on the AFM images shown in Fig. 5.14) with different shapes and sizes were observed on the surface of all InN samples, consis-

### 5.3. Comparisons of N- and In-polar InN

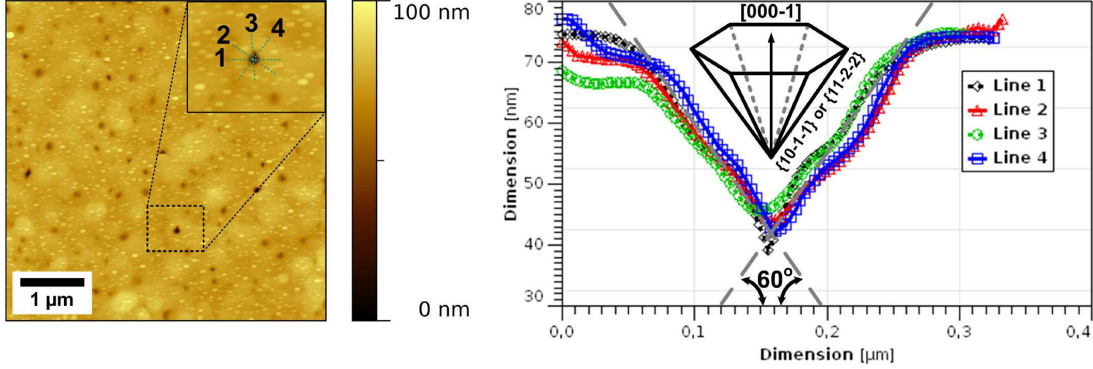


**Figure 5.15:** Line profiles of a pit on the surface of the InN layer grown directly on *c*-plane sapphire grown at 560°C (Fig. 5.14(d)). The line profiles across the pits shows an inverted pyramidal shape with the base angles of  $\sim 60^\circ$  (fit angle), indicating a V-pit with six  $\{10\bar{1}1\}$  or  $\{11\bar{2}2\}$  facets.

tent with the obtained metallic indium peaks on the XRD measurements (Fig. 5.10). Additionally, the InN layers grown directly on sapphire showed the presence of hexagonal islands (200-800 nm), likely related to the existence of the indium droplets that recrystallized into these islands.

A large number of hexagonal pits with different sizes (50-300 nm) and depths (40-100 nm) are observed on the surfaces of the InN layers grown on sapphire (Fig. 5.15). The line profiles across the pits indicate that the pits consist of six  $\{10\bar{1}1\}$  or  $\{11\bar{2}2\}$  facets (V-like pits). The appearance of the V-pits mainly is attributed to screw and mixed threading dislocations [116].

In the case of the InN layers grown on GaN templates, the line profiles cross the islands shows an isosceles trapezoidal or pyramidal shape with the base angles of  $\sim 60^\circ$ , corresponding to six  $\{10\bar{1}1\}$  or  $\{11\bar{2}2\}$  boundary facets (Fig. 5.16). With increasing growth temperature, the lateral size of the islands increases from about 100 nm to 400 nm. However, the islands did not fully coalesce even after a long growth time (300 nm thickness) at different growth temperatures.

Recently, the effect of polarity on the growth of InN layers grown on GaN templates by MOVPE was investigated [117]. The surface morphology of N-/In-polar InN layers on N-/Ga-polar GaN templates [117] showed similar features as observed here for the N-polar InN layers grown on sapphire and the In-polar InN layers grown on GaN templates. The growth mode of N-polar InN layers grown on N-polar GaN templates was signed to the Frank-van der Merwe, while the Volmer-Weber growth mode was

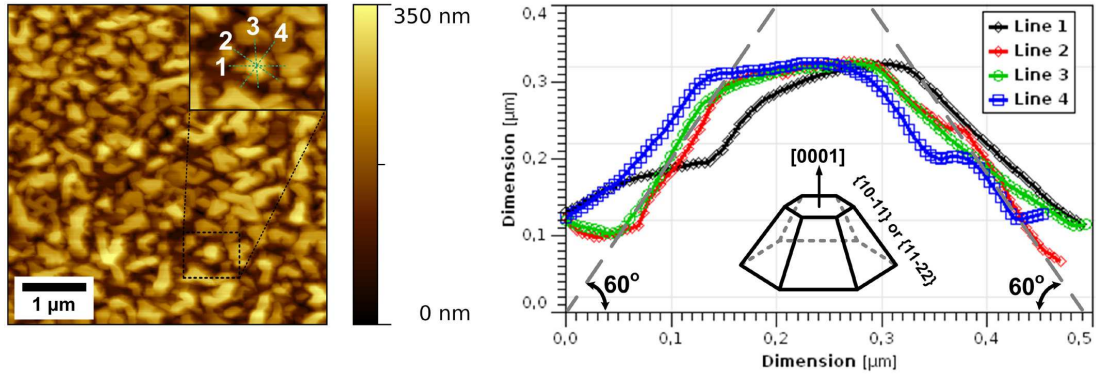


**Figure 5.16:** Line profiles of an island on the surface of the In-polar InN layer on *c*-plane GaN grown at 560°C (Fig. 5.14(h)). The line profiles across the islands shows an isosceles trapezoidal or pyramidal shape with the base angles of  $\sim 60^\circ$  (fit angle), corresponding to six  $\{10\bar{1}1\}$  or  $\{11\bar{2}2\}$  boundary facets bounding the island.

referred to In-polar InN layers grown on Ga-polar GaN templates [117, 118]. Those growth modes were associated with the differences in the surface bonding arrangements of atoms on the surfaces of N-/In-polar InN layers. For the growth modes in those cases, InN layers were assumed to be N-terminated [117]. However, the N-terminated surfaces are energetically always less stable than the corresponding In-terminated surfaces [103]. Furthermore, as mentioned before with the used growth conditions, indium droplets were found for both the InN layers grown on sapphire and the InN layers grown on GaN templates by AFM (Fig. 5.14) and XRD (Fig. 5.10). This confirms the existence of exceeding indium on the surface of both the InN layers and therefore an In-terminated surface. It means that the growth modes, Frank-van der Merwe for N-polar InN and Volmer-Weber for In-polar InN, were observed for the In-terminated surfaces meaning that surface termination does not have a critical effect on the growth modes.

Density-functional theory (DFT) calculations of the adatom kinetics of Ga-/In-atoms on the *c*-plane (0001) surface [119], and the nonpolar *a*-plane (11 $\bar{2}$ 0) and *m*-plane (1 $\bar{1}$ 00) surfaces [120, 121] showed a strong dependence on specific geometry and stoichiometry of these surfaces due to the different bonding properties of the weak metallic Ga-Ga/In-In bonds and the strong covalent Ga-N/In-N bonds. Furthermore, for all the GaN and InN surfaces, it was found that N-atoms have a very low diffusivity compared to Ga-/In-atoms.

The adatom diffusion on a layer surface is strongly depended on growth condition. Due to the very high equilibrium vapor pressure of nitrogen and the weak In-N bond,

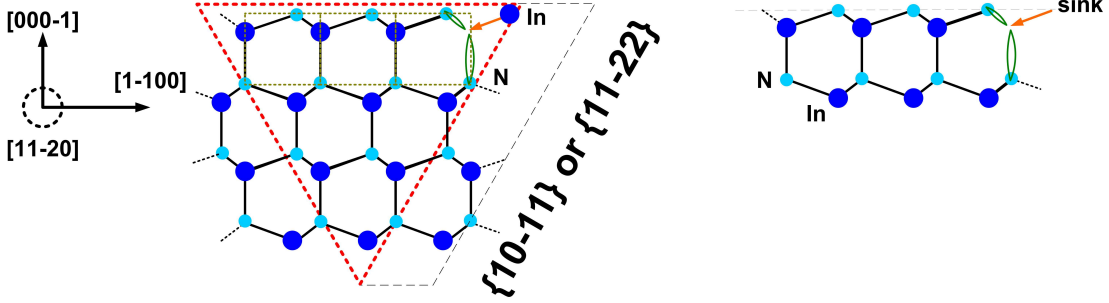


**Figure 5.17:** Growth mechanism of N-polar InN. In-atoms can be easily trapped into the sink consists of two N dangling bonds on the  $c$ -plane surface.

the growth of InN is normally performed at very low temperature (i.e., 400-600°C) compared to the growth temperature of GaN or AlN (i.e., 1000-1400°C). Additionally, at that temperature range, the decomposition rate of  $\text{NH}_3$  is very low (Fig. 3.7). Thus, even with a very high V/III ratio (i.e., V/III ratio = 15000), the InN growth is still under a very In-rich condition. The growth rate of N-polar InN layers on sapphire (about 100 nm/h) is normally lower than that of In-polar InN layers on GaN templates (about 150 nm/h).

The growth modes of  $c$ -plane InN layers on sapphire and GaN templates could be explained following growth models for InN layers with the different polarities on  $c$ -plane GaN templates [117]. For N-polar  $(000\bar{1})$  InN, the surface bonding arrangement of atoms on the surface was previously shown in Fig. 5.1(d). An individual N-atom at the N-polar InN surface has one dangling bond upward, and three dangling bonds inward which bond to three underneath In-atoms. After one In-atom bonds to one N-atom on the surface, the In-atom will have three free dangling bonds which can easily bond to three N-atoms (Fig. 5.1(e)). This creates a sink on the surface step that consists of two nitrogen dangling bonds, one from the atop N-adatom layer and one from the adjacent N-adatom layer (Fig. 5.17). This sink is expected to trap In-atom to form a lateral growth of the  $(000\bar{1})$  InN surface. Higher growth temperatures can enhance In-diffusion length on the  $(000\bar{1})$  surface, which can contribute to the change of surface morphology of the InN layers. In fact, the AFM images of the InN layers on sapphire (Fig. 5.14) confirm that the surface morphology of the InN layers gets smoother with increasing growth temperatures.

In the case of In-polar  $(0001)$  InN, the surface bonding of atoms and dangling bond configurations can be explained in Fig. 5.1(a). Since In-atoms are at the atop surface

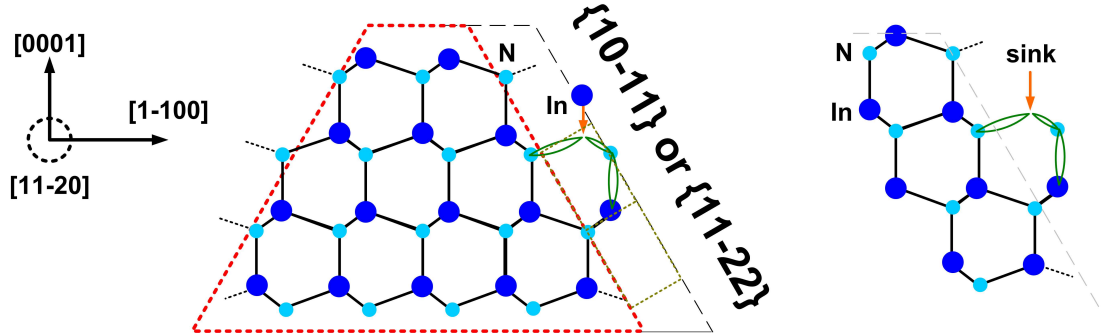


**Figure 5.18:** Growth mechanism of In-polar InN. Similar to N-polar InN, In-atoms can be easily trapped into the sink consists of two N dangling bonds on the  $(10\bar{1}1)$  or  $(11\bar{2}2)$  surface.

of InN layer which can bond to N-atoms; afterwards those bonds can create sinks to trap In-atoms. At the surface steps of In-polar InN, N-atoms can also bond to In-atoms. The two possibilities of trapping In-atoms are equal (at the surface steps and at the sink). Since In-atoms diffuse very fast on the (0001) surface due to the weak metallic In-In bond compared to the strong covalent In-N bond, this leads to a faster growth process in the perpendicular direction ( $[0001]_{\text{InN}}$ ) and a slower growth rate in the parallel direction ( $[1\bar{1}00]_{\text{InN}}$ ). However, as mentioned above, the initial growth of InN on GaN by MOVPE was attributed to the 3D Volmer-Weber growth mode [118]. When the growth rate along the  $[0001]$  direction is much faster compared to that in the  $[1\bar{1}00]_{\text{InN}}$  direction, this will lead to a formation of a 3D growth structure with a trapezoidal shape (Fig. 5.18). The trapezoidal structures can be changed to pyramidal shapes if the growth rate in the  $[0001]_{\text{InN}}$  direction is fast enough.

The  $\{10\bar{1}1\}$  and  $\{11\bar{2}2\}$  boundary facets of the InN islands on GaN templates should be taken into account to explain the growth process of the InN layers on GaN templates (Figs. 5.16 and 5.18). The  $(10\bar{1}1)$  and  $(11\bar{2}2)$  surfaces also have N-polarity and has a similar dangling bond configuration qualitatively similar to the  $(000\bar{1})$  surface, but rotated by  $\sim 60^\circ$  with respect to the  $c$ -plane (Fig. 5.18). The  $(10\bar{1}1)$  and  $(11\bar{2}2)$  surfaces also have one dangling bond at any sites of the surface, similar to the  $(000\bar{1})$  surface (Fig. 5.18). Even though a lower growth rate is expected in the perpendicular direction of the  $(10\bar{1}1)$  and  $(11\bar{2}2)$  surfaces due to a higher diffusion barrier in that direction caused by the strong covalent In-N bond, similar to the  $(000\bar{1})$  surface. However, the layer growth might be affected by the surface area of that layer. The larger surface area

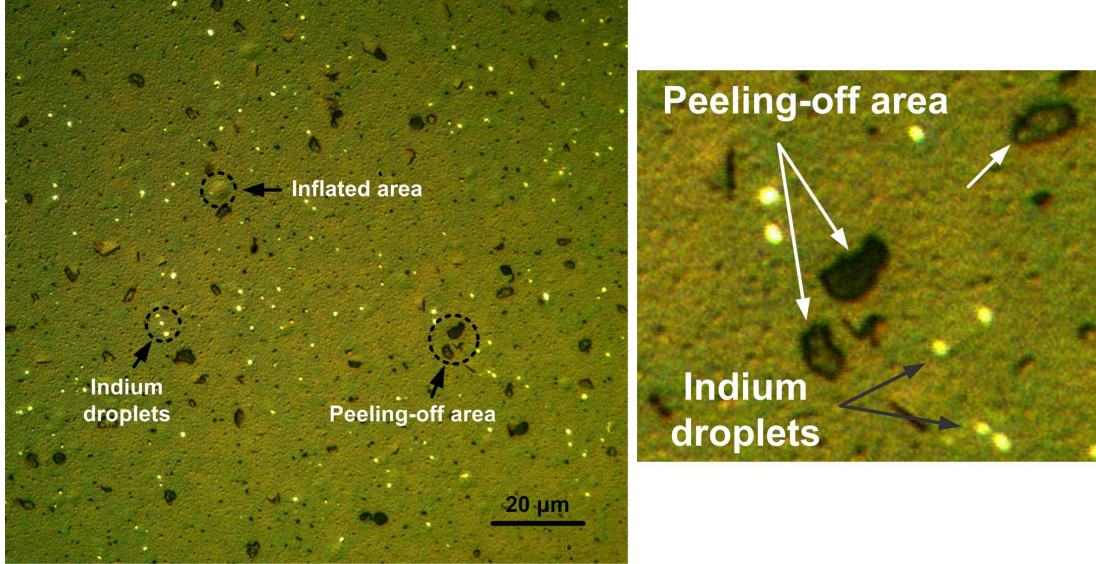


**Figure 5.19:** Normaski optical microscopic image of a *c*-plane InN layer grown at 560°C on *c*-plane sapphire. In the image, indium droplets (white dots), inflated areas, and peeling-off areas (dashed circles) can be obviously seen.

of the layer, the higher chance to incorporate more atoms. The 3D growth with the  $\{10\bar{1}1\}$  or  $\{11\bar{2}2\}$  boundary facets results in the larger total  $(10\bar{1}1)$  (or  $(11\bar{2}2)$ ) surface area compared to the  $(0001)$  surface. Therefore, the growth at the sides of the islands is expected to be faster than at the topmost  $(0001)$  surface. The fact that the lateral size of islands increases with increasing growth temperatures and growth times (i.e., from quantum dots to layer) also confirms our interpretation.

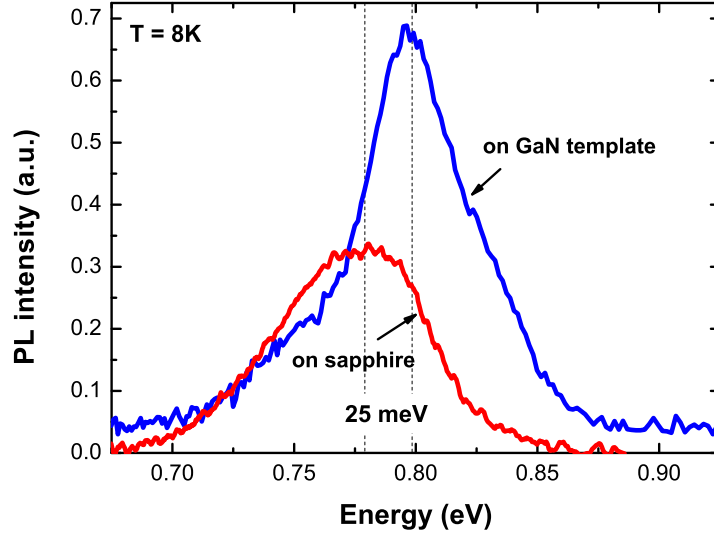
The growth rate of InN with the different polarities is affected not only by adatom diffusion but also by the adsorption/desorption rate. The growth rate of N-polar InN (about 100 nm/h) is normally slower than that of In-polar InN (about 150 nm/h). Additionally, the growth rate of InN (both polarities) is very sensitive to hydrogen etching due to the weaker In-N bond compared to the stronger Ga-N and Al-N bonds. Under H-irradiation, the N-polar InN showed a much faster etching rate compared to In-polar InN, similar to the KOH wet-etching results [103]. This behavior is explained via the differences of the dangling bond configurations between the N- and the In-polar surfaces during the etching process. The surfaces having N-polarity such as the  $(000\bar{1})$ ,  $(10\bar{1}1)$ , and  $(11\bar{2}2)$  surfaces are easily etched in the existence of H-atoms and  $\text{NH}_x$ -radicals (derived from the  $\text{NH}_3$  decomposition) since H-atoms can break the In-N bonds to create

a formation of volatile  $\text{NH}_x$ -radicals. The  $\text{NH}_x$ -radicals easily desorb from the surface at the applied growth temperature. This leads to the formation of an In-rich surface where In-atom is only loosely bound to the surface and form In-droplets. H-atoms can diffuse to the N-atoms below the In-rich layer and lead to further etching. At higher growth temperatures, the higher  $\text{NH}_3$  decomposition rates produce more H-atoms and  $\text{NH}_x$ -radicals, and hence cause the faster hydrogen etching rates. In the case of In-polar InN, the In-atoms on the surface are bound to the three underneath N-atoms. These bonds are easily broken by the attachments of H-atoms and  $\text{NH}_x$ -radicals during growth process.

InN layers grown directly on sapphire often peels off or produces inflated areas where the layer peels off sapphire (Fig. 5.19). Inflated areas might be occurred during growth (due to no full strain relaxation) or after growth during cooling (due to the different thermal expansions). The In-polar InN layers grown on GaN templates do not peel off because of the 3D morphology allowing strain relaxation (Figs. 5.14(e-h)). Nearly no stress at room temperature on the InN layer on sapphire despite the different thermal expansions indeed indicate a weaker bond InN/sapphire interface compared to the InN layers on GaN templates. The peeling-off areas on the interface of InN layers and sapphire might cause the layers become a free-standing template, and hence release the strain upon the cooling after the growth.

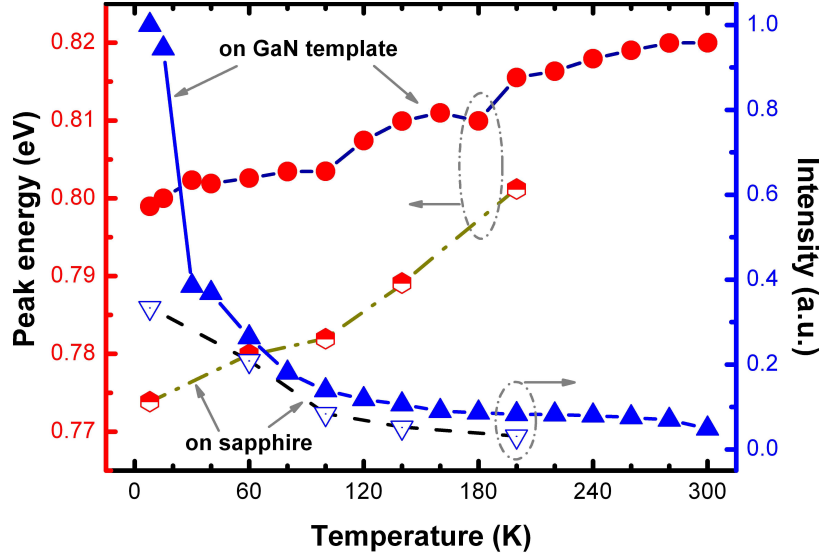
### 5.3.4 Optical properties

Figure 5.20 shows the low-temperature photoluminescence (PL) spectra (at 8K) of the InN layers grown at 530°C directly on *c*-plane sapphire substrate and on *c*-plane GaN template. The InN layer grown on GaN template showed a near band-edge (NBE) luminescence at  $\sim 0.8$  eV with a FWHM value of 63 meV, while the InN layer grown on sapphire showed an NBE luminescence at  $\sim 0.77$  eV with a FWHM value of 72 meV (Gaussian fits). Both PL spectra show asymmetrical broadenings at the low energy range that might be mostly due to the decreased response of the Ge detector. PL intensity of the InN layer grown on GaN template was as a factor of two higher compared to the InN layer grown on sapphire. Even at room temperature, PL from the InN layer grown on GaN template was obtained, while PL from the InN layer grown on sapphire could only be obtained below  $\sim 200$  K (Fig. 5.21).



**Figure 5.20:** Low-temperature photoluminescence (PL) spectra of the InN layers grown directly on *c*-plane sapphire and on *c*-plane GaN template at 530°C, respectively. The PL intensities were normalized with response function of Ge detector.

For blue-shift of NBE luminescence spectrum of highly doped InAs, a correlation between with carrier concentration was found due to the Burstein-Moss effect [122]. Recently it was demonstrated that the blue-shifts of absorption edge of lithium-doped ZnO caused by the increased dopant concentrations (and hence relate to the Burstein-Moss or band-filling effect) had a similar trend to the blue-shifts of NBE luminescence [123]. In the case of InN, a PL peak shifts to higher energies of the InN layers might be also associated with the Burstein-Moss effect due to increased carrier concentrations ( $> 10^{17} \text{ cm}^{-3}$ ) [16, 110]. Due to the high electron concentration of InN, the thermal equilibrium energy in the conduction band of InN would not be located at the conduction band minimum, this could raise the effective Fermi energy level via the Burstein-Moss effect. To check the correlation between carrier concentrations and the Burstein-Moss effect, Hall-effect measurements were performed at room temperature showed a free electron concentration of  $2.3 \times 10^{19} \text{ cm}^{-3}$  and a carrier mobility of  $370 \text{ cm}^2/\text{Vs}$  for the InN layer grown on sapphire, and  $1.5 \times 10^{19} \text{ cm}^{-3}$  and  $198 \text{ cm}^2/\text{Vs}$  for the InN layer grown on GaN template. However, Hall-effect measurements may overestimate the carrier concentrations due to the effects of the surface accumulation layers [124, 125] and morphological defects [124]. Thus the blue-shifts of the PL peak energies of the InN layers will be further discussed where they might be originated by point defects



**Figure 5.21:** Temperature dependency of the PL energy peaks and intensities of the In-polar InN grown on GaN template and the N-polar InN grown directly on sapphire at 530°C.

(or vacancies), unintentional impurities (or background doping), and strain relaxation.

At room temperature, the PL peak energy measured from the InN layer grown on GaN template (Fig. 5.21) showed a blue-shift of  $\sim 0.17$  eV compared to the InN bandgap of 0.65 eV [18]. A plausible explanation for the blue-shift can be unintentional impurities such as carbon and oxygen, as well as native point defects (i.e., nitrogen vacancies [126]). Nitrogen vacancies are easily produced in the layers due to the In-rich growth conditions and the low growth temperatures used for InN growth. Since all the InN layers showed the very high electron concentrations, the electron concentrations might be attributed to ionization of intrinsic point defects related to nitrogen vacancies [126]. Theoretical calculation showed the ionization energy of nitrogen vacancies in InN to be about 0.15 eV [126]. This activation energy would lead to a continuous increase of the carrier concentration which would lead to a continuous blue-shift in agreement with the PL measurements.

Beside the effect of N-vacancies, the blue-shifts of PL peak energies of the InN layers might be caused by impurities as well. In general, oxygen, hydrogen, and carbon are unintentionally incorporated in III-nitrides during growth, especially in InN due to the much lower growth temperatures compared to GaN and AlN. For example,  $\text{NH}_3$  is contributed as a source of hydrogen dopant for MOVPE-grown InN [127]. The surface

### 5.3. Comparisons of N- and In-polar InN

---

polarity of III-nitrides is also expected to strongly affect the amount of incorporated impurities, e.g., N-polar InN incorporates more hydrogen than In-polar InN [128]. As shown before, the InN layer on sapphire showed the flat morphology compared to the 3D morphology of the InN layer on GaN template. The 3D islands of the InN layers on GaN templates consist of six  $\{10\bar{1}1\}$  or  $\{11\bar{2}2\}$  boundary facets, which also have N-termination. Therefore, the total surface area (grain boundaries) of the InN layers on GaN templates are larger (smaller) than those of the N-polar InN layers on sapphire. During the growth processes, the higher amount of atomic hydrogen, oxygen, and carbon may reside along the smaller grain boundaries [128]. Consequently, the InN layers on GaN templates might incorporate a larger amount of the unintentional impurities than the InN layers on sapphire. Consequently, due to the higher impurities incorporation in the InN layer grown on GaN template might cause the blue-shift of the PL peak energies due to an increase of impurities-related donor concentration [129].

Recently, a correlation between FWHM values on PL intensity and bulk residual doping of InN was developed [130]. By using that model, the electron density of the InN layers grown on sapphire and on GaN template were estimated to be about  $1 \times 10^{18} \text{ cm}^{-3}$  and  $7 \times 10^{17} \text{ cm}^{-3}$ , respectively. Since the InN layer grown on GaN template has a lower carrier concentration by Hall-effect measurement and by the FWHM analysis of the PL intensity, the larger PL peak shift cannot be caused only by the Burstein-Moss effect. Since the InN layer grown on GaN template also showed residual stress in Raman (Fig. 5.11), the compressive stress could shift the PL peak energy to higher energies on the InN layer grown on GaN template. Similar correlations were also found for InGaAs and InGaP [131], where the bandgap of strained layers was larger than that of unstrained layers when under compression, and was smaller under tension.

Temperature-dependent PL spectra from all the grown InN samples showed an abnormal temperature dependence of the peak energy (Fig. 5.21). Generally, the energy bandgap of semiconductors tends to increase with decreasing temperatures due to the thermally decrease of the amplitude and the interatomic spacing of the atomic vibrations [132]. In Fig. 5.21, the PL peak intensity exponentially decreased with increasing temperatures due to an increase in the rate of non-radiative recombination of holes; however the PL peak energies increased with increasing temperatures. Similar abnormal temperature-dependent PL spectra were reported for InN grown by MBE [133, 134]. A nearly temperature-independent PL peak energy was explained by

the existence of the metallic indium clusters that leads to the efficient exciton localization phenomena that occurs at the indium/InN interface [133]. Additionally, due to the very high electron concentrations at room temperature for both samples on sapphire and on GaN templates, the effective Fermi energy level could be shifted upwards by the band-filling effect. The shift of the Fermi level can be attributed to the ionization of the donor-like centers (native point defects, e.g. nitrogen vacancies [126]), as well as hydrogen [127, 129] after increasing temperature).

### 5.4 Chapter summary

Nitridation of  $a$ -plane (11 $\bar{2}$ 0) and  $c$ -plane (0001) sapphire substrates at temperatures from 600°C to 1050°C was employed to grow  $c$ -plane InN layers. The sapphire nitridation was found to be crucial to control the polarity, and to improve the crystallinity and the surface morphology of the InN layers. Nitridation temperatures above 800°C led to N-polar InN layers, while nitridation temperatures from 700°C to 750°C produced mixed-polar InN layers and nitridation temperatures from 500°C to 650°C produced In-polar InN layers.

The growth process, crystallinity, and optical properties of the InN layers with N- and In-polarity were compared. To produce layers with N-polarity, InN layers grown on  $c$ -plane sapphire nitridated at 1050°C, while In-polar InN layers were grown on  $c$ -plane Ga-polar GaN templates. N-polar and In-polar InN layers showed different surface morphologies and crystallinities. The smoothest N-polar InN was obtained at higher growth temperatures (5 nm for 5  $\mu\text{m} \times 5 \mu\text{m}$ ), while the smoothest In-polar InN was obtained at intermediate growth temperatures (17 nm for 5  $\mu\text{m} \times 5 \mu\text{m}$ ). Growth mode of the N-polar InN layers on sapphire was found to be Frank-Van der Merwe (2D growth mode), while growth mode of the In-polar InN layers on GaN templates was Volmer-Weber (3D growth mode). In-polar InN layers exhibited a higher growth rate than N-polar InN layers for identical precursor flows, i.e., 150 nm/h and 100 nm/h, respectively. Electrical properties were similar for both layers. Raman spectra showed the same curves with two dominant phonon modes ( $E_2(\text{high})$  mode at  $\sim 491 \text{ cm}^{-1}$  and  $A_1(\text{LO})$  mode at  $\sim 596 \text{ cm}^{-1}$ ) for all the InN layers on sapphire and GaN templates. The In-polar InN layers on GaN templates showed a residual stress, while the N-polar InN layers showed a fully strain relaxation. Both the InN layers showed near-band-edge

#### 5.4. Chapter summary

---

luminescence around 0.75 eV at low temperature. Low-temperature photoluminescence of the In-polar InN layers was shifted to higher energies likely due to biaxial compressive stress and incorporation of different impurities.

## Chapter 6

# Semipolar $(10\bar{1}\bar{3})$ InN

This chapter deals with the growth and characterizations of semipolar  $(10\bar{1}\bar{3})$  InN layers on  $m$ -plane sapphire. The growth parameters were shown previously in Section 3.5. Additionally, ellipsometric transient of an InN layer on  $m$ -plane sapphire (nitridation at  $1050^\circ\text{C}$  for 2 min) was shown in Fig. 3.12. The nitridation process on  $m$ -plane sapphire (from 45 s to 6 min) at  $1050^\circ\text{C}$  was found to be very crucial for the crystal orientation of  $(10\bar{1}\bar{3})$  InN. Very short and very long nitridation times resulted in additional phases. Since the simultaneously grown  $c$ -plane InN layer on  $c$ -plane sapphire showed N-polarity (Section 5.3), the InN layers on  $m$ -plane sapphire were expected to have N-polarity.

### 6.1 Crystallinity and in-plane relationship

In order to investigate crystallinity of the InN layers grown on  $m$ -plane sapphire, X-ray diffraction (XRD) measurements were performed with an open detector. The plane of incidence was paralleled to the  $[0001]$  axis of the  $m$ -plane sapphire substrates.

Figure 6.1 shows symmetric XRD  $\omega/2\theta$  scans of the InN layers grown on  $m$ -plane sapphire with different nitridation times. For 2 min and 4 min nitridation, only the semipolar  $(10\bar{1}\bar{3})$  reflection of InN at  $\sim 28.5^\circ$  was found. For shorter and longer nitridation, the InN layers showed some additional reflections like  $(10\bar{1}\bar{2})$ ,  $(11\bar{2}0)$ ,  $(11\bar{2}\bar{2})$ ,  $(10\bar{1}\bar{4})$ ,  $(11\bar{2}\bar{4})$ ,  $(20\bar{2}\bar{4})$ , and  $(20\bar{2}\bar{5})$ . No reflections of metallic indium were observed in all the InN layers grown on  $m$ -plane sapphire. Interestingly, XRD spectra for all the

## 6.1. Crystallinity and in-plane relationship

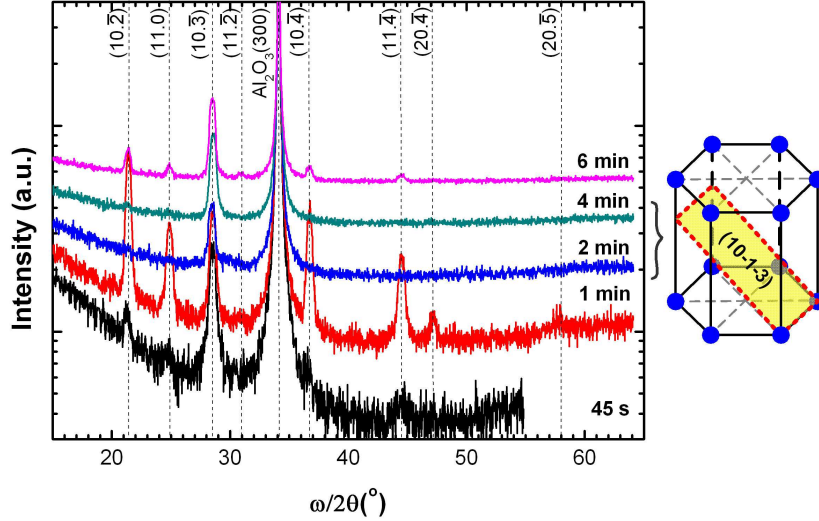


**Figure 6.1:** XRD  $\omega/2\theta$  scans of the InN layers grown on  $m$ -plane sapphire for different nitridation times at 1050°C.

simultaneously grown  $c$ -plane InN layers on  $c$ -plane sapphire showed the appearance of metallic indium (as shown in Fig. 5.10).

The epitaxial in-plane relationship of the  $(10\bar{1}\bar{3})$  InN layers and  $m$ -plane sapphire was determined from XRD off-axis  $\phi$ -scans. The skew-symmetric  $(20\bar{2}\bar{4})$  reflection of  $m$ -plane sapphire substrate was measured with a tilt angle ( $\psi$ ) of 32.38°, which indicates the  $[0001]$  direction of the  $m$ -plane sapphire (Fig. 6.2). Since the  $(10\bar{1}\bar{3})$  InN surface is tilted by  $\sim 31.8^\circ$  with respect to the  $(000\bar{1})$  InN surface, to indicate the  $[0001]_{\text{InN}}$  direction of  $(10\bar{1}\bar{3})$  InN, the skew-symmetric  $(0002)$  reflection of the  $(10\bar{1}\bar{3})$  InN layers was measured with a tilt angle of  $\sim 31.8^\circ$ . In Fig. 6.2, two skew-symmetric  $(0002)$  reflections of  $(10\bar{1}\bar{3})$  InN were found, rotated by  $\pm 90^\circ$  with respect to the  $(20\bar{2}\bar{4})$  reflection of  $m$ -plane sapphire. Since there is no other lattice plane having the same  $2\theta$  angle and tilting to the surface, the appearance of two skew-symmetric  $(0002)$  reflections indicates crystallite twinning of the  $(10\bar{1}\bar{3})$  InN layers on  $m$ -plane sapphire in two opposite directions, as illustrated in Fig. 6.2. The in-plane relationship of the  $(10\bar{1}\bar{3})$  InN layers and  $m$ -plane sapphire was determined to be  $[30\bar{3}\bar{2}]_{\text{InN}} \parallel [1\bar{2}10]_{\text{sapphire}}$  and  $[1\bar{2}10]_{\text{InN}} \parallel [0001]_{\text{sapphire}}$ , and  $[\bar{3}032]_{\text{InN}} \parallel [1\bar{2}10]_{\text{sapphire}}$  and  $[\bar{1}2\bar{1}0]_{\text{InN}} \parallel [0001]_{\text{sapphire}}$ , which is rotated by 180° in the growth plane.

The crystallite twinning of the  $(10\bar{1}\bar{3})$  InN layers was also observed in symmetric XRD reciprocal space maps (RSM). Figure 6.3 shows the symmetric RSM of the

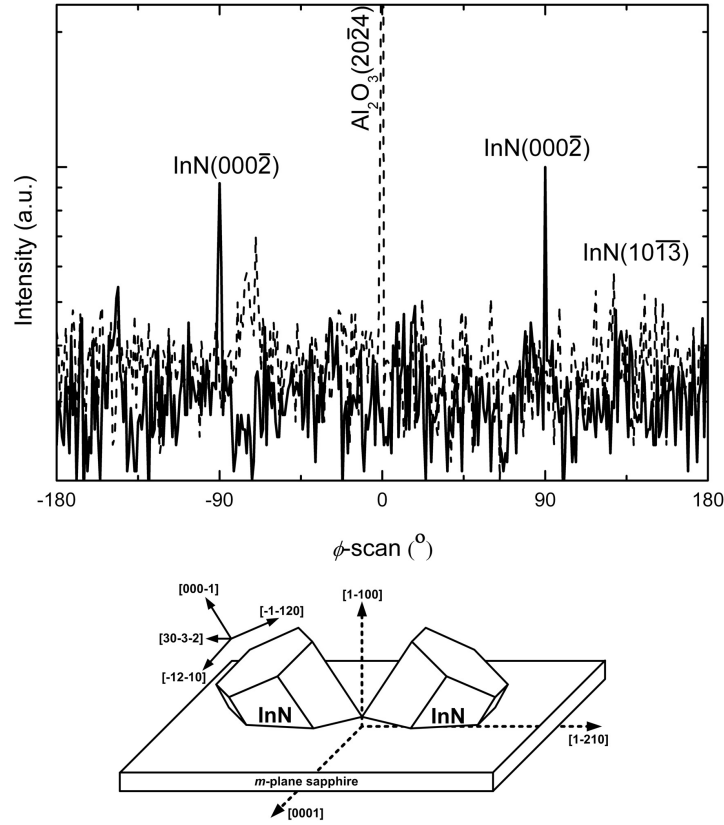


**Figure 6.2:** XRD off-axis  $\phi$ -scans with settings for the  $(0002)$  reflections of  $(10\bar{1}\bar{3})$  InN and of the  $(20\bar{2}\bar{4})$  reflection of  $m$ -plane sapphire performed in skew-symmetry. The schematic below shows the resulting epitaxial in-plane relationship of  $(10\bar{1}\bar{3})$  InN on  $m$ -plane sapphire substrate.

$(10\bar{1}\bar{3})$  InN reflections along the  $[0001]_{\text{sapphire}}$  in-plane direction (Fig. 6.3(a)) and along the  $[\bar{1}\bar{2}10]_{\text{sapphire}}$  in-plane direction (Fig. 6.3(b)). In Fig. 6.3(a), two  $(10\bar{1}\bar{3})$  InN reflections were observed in two opposite directions with respect to the  $(30\bar{3}0)$  reflection of sapphire. The RSM indicates the  $(10\bar{1}\bar{3})$  InN twins were tilted about  $\pm 1.1^\circ$  in the  $[\bar{1}\bar{2}10]_{\text{sapphire}}$  and  $[\bar{1}\bar{2}\bar{1}0]_{\text{sapphire}}$  directions (Fig. 6.3(a)) and tilted about  $0.1^\circ$  in the  $[0001]_{\text{sapphire}}$  direction (Fig. 6.3(b)). The tilt angles may be due to the different lattice mismatches of  $(10\bar{1}\bar{3})$  InN and  $m$ -plane sapphire, 13.8% along the  $[\bar{1}\bar{2}10]_{\text{sapphire}}$  direction and 9.1% along the  $[0001]_{\text{sapphire}}$  direction. Due to the different lattice mismatches, unequal dislocation distributions in both directions are expected to be present [135–139], and hence this induces the tilts of the layers. The tilts of the  $(11\bar{1}\bar{3})$  InN layers might also relate to lattice tilts [140, 141] since the layers were grown on  $m$ -plane sapphire, a vicinal

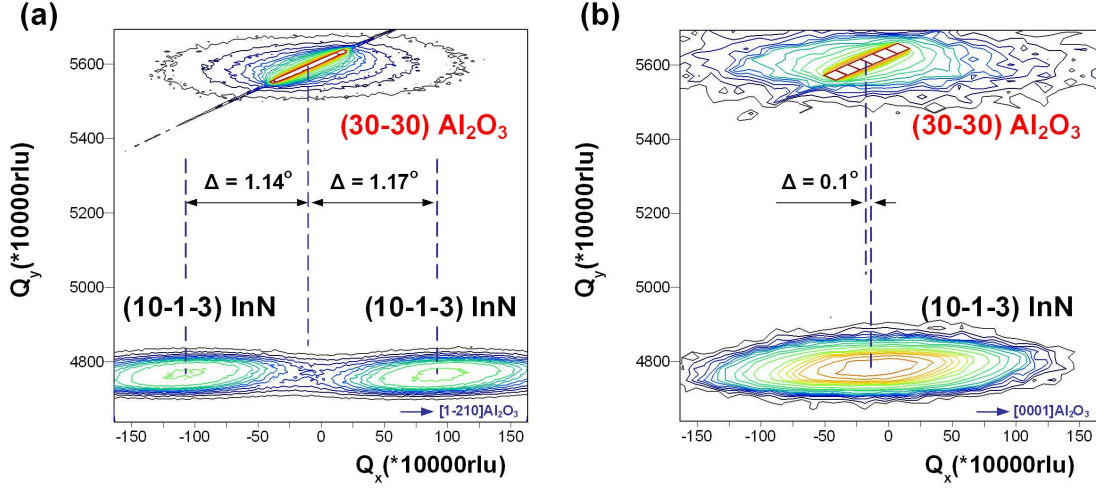


**Figure 6.3:** Reciprocal space maps of the  $(10\bar{1}\bar{3})$  InN layer grown on  $m$ -plane sapphire performed (a) along the  $[0001]_{\text{sapphire}}$  in-plane direction and (b) along the  $[\bar{1}\bar{2}10]_{\text{sapphire}}$  in-plane direction .

substrate containing surface steps (which is shown latter in Fig. 6.9). Additionally, the tilts of the InN layers might be related to the appearance of misfit dislocations, which are commonly present at the hetero-interfaces between semi-/non-polar III-nitrides and substrate, existing in the  $[1\bar{1}00]$  direction of III-nitrides [135–139, 142]. The misfit dislocations not only induce the relaxation, but also cause rotational misorientations of III-nitride epilayers in the  $[0001]$  direction [136–139].

The RSM indicate an anisotropic FWHM of the InN layers on  $m$ -plane sapphire in two perpendicular directions. The symmetric  $(10\bar{1}\bar{3})$  InN X-ray rocking curves (XRC) along the  $[30\bar{3}\bar{2}]_{\text{InN}}$  ( $[\bar{1}\bar{2}10]_{\text{sapphire}}$ ) direction and along the  $[\bar{1}\bar{2}10]_{\text{InN}}$  ( $[0001]_{\text{sapphire}}$ ) direction were measured in order to further investigate in-plane structural anisotropy (Fig. 6.4). The XRC scans of all the layers along the  $[30\bar{3}\bar{2}]_{\text{InN}}$  direction showed two  $(10\bar{1}\bar{3})$  peaks due to the crystallite twinning of the layers. The full width at half maximum (FWHM) values of the two peaks were almost equivalent (about  $1.39$  -  $1.90^\circ$ ), indicating the same crystallinity of the twinned  $(10\bar{1}\bar{3})$  InN layers along the  $[\bar{1}\bar{2}10]_{\text{sapphire}}$  and the  $[\bar{1}\bar{2}\bar{1}0]_{\text{sapphire}}$  directions. Along the  $[\bar{1}\bar{2}10]_{\text{InN}}$  direction, only one  $(10\bar{1}\bar{3})$  reflection was observed (Fig. 6.4(a)). The FWHM values of the  $(10\bar{1}\bar{3})$  InN XRC of all the InN layers were  $0.78$  -  $1.36^\circ$  along the  $[\bar{1}\bar{2}10]_{\text{InN}}$  direction, and  $2.78$  -  $3.76^\circ$  (both peaks) along the  $[30\bar{3}\bar{2}]_{\text{InN}}$  direction (Fig. 6.4(b)). However, no clear correlation of the FWHM values with the nitridation times were found.

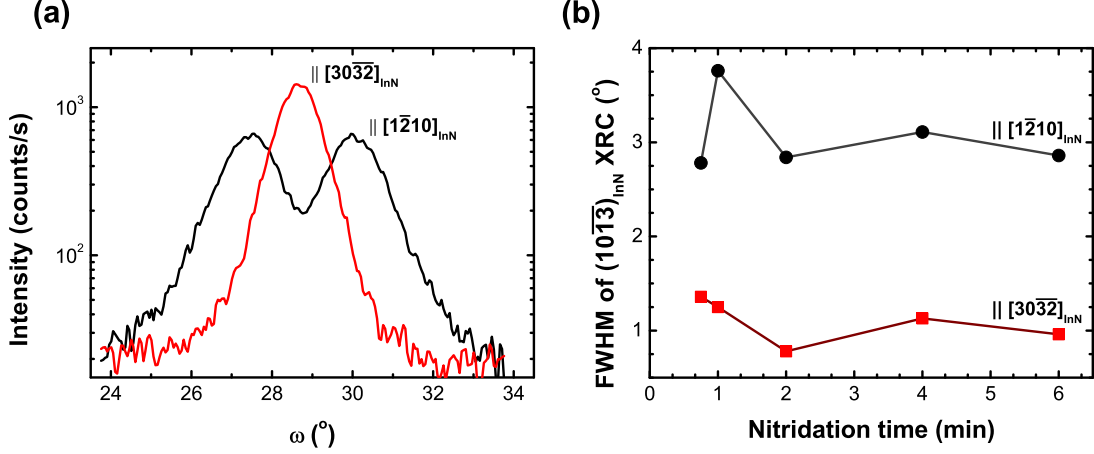


**Figure 6.4:** (a) The  $(10\bar{1}\bar{3})$  X-ray rocking curves (XRC) of an InN layer grown on  $m$ -plane sapphire scanned along the  $[30\bar{3}\bar{2}]_{\text{InN}}$  and the  $[1\bar{2}10]_{\text{InN}}$  directions. (b) the FWHM values of the XRC of the InN layers grown on  $m$ -plane sapphire as a function of nitridation time. The FWHM values of the XRC scans along the  $[1\bar{2}10]_{\text{InN}}$  direction includes the FWHM values of both  $(10\bar{1}\bar{3})$  InN peaks.

The crystallite twinning of  $(10\bar{1}\bar{3})$  InN on  $m$ -plane sapphire was similar to  $(10\bar{1}\bar{3})$  GaN grown on  $m$ -plane sapphire using MOVPE [143, 144]. For GaN layer on  $m$ -plane sapphire, depending on nitridation process (i.e., nitridation temperature and time), the layer might predominate the  $(10\bar{1}\bar{3})$  phase or the  $(11\bar{2}\bar{2})$  phase [144].

Based on the growth of pure semipolar  $(10\bar{1}\bar{3})$  and  $(11\bar{2}\bar{2})$  GaN layers on  $m$ -plane sapphire by MOVPE [144], calculations of the lattice constants for all the material systems were performed [145]. It was found that the lattice constant of the  $(10\bar{1}\bar{3})$  GaN orientation is best matched to the  $a$ -axis of sapphire compared to the other  $(10\bar{1}L)$  orientations (with  $L \neq 0, 3$ ), while the lattice constant of the  $(11\bar{2}\bar{2})$  GaN orientation is best matched to the  $c$ -axis of sapphire compared to the other  $(11\bar{2}L)$  orientations (with  $L \neq 0, 2$ ) [145]. This might be used to explain why the  $(10\bar{1}L)$  layers were grown along the  $[1\bar{2}10]_{\text{sapphire}}$  direction, while the  $(11\bar{2}L)$  layers were grown along the  $[0001]_{\text{sapphire}}$  direction. The two possibilities of the  $(10\bar{1}\bar{3})$  GaN and  $(10\bar{1}\bar{3})$  InN growth might be explained by the equalities of the growth of thin  $(10\bar{1}\bar{3})$  AlN layers on  $m$ -plane sapphire via nitridation process. By the nitridation of  $m$ -plane sapphire, the  $(10\bar{1}\bar{3})$  AlN layers were produced equally along the  $[1\bar{2}10]_{\text{sapphire}}$  and the  $[\bar{1}\bar{2}\bar{1}0]_{\text{sapphire}}$  directions [145].

For semipolar III-nitrides the suppression of the twins is needed to improve the surface morphology and crystallinity. Recently, studies on the MOVPE growth of

## 6.2. Surface morphology and surface diffusion

---

( $10\bar{1}3$ ) InN on (110) GaAs at different growth temperatures from 510-615°C were reported [146, 147]. Semipolar ( $10\bar{1}3$ ) InN layer grown on (110) GaAs also showed crystallite twinning along the [111] and  $[11\bar{1}]$  in-plane directions. It was shown that the twins of the ( $10\bar{1}3$ ) InN layers on (110) GaAs were suppressed to obtain only one dominant symmetry (along the  $[11\bar{1}]_{\text{GaAs}}$  direction) when the growth temperatures were higher 550°C, i.e., no crystallite twinning was observed for ( $10\bar{1}3$ ) InN layer grown at 615°C [147]. The twinning suppression was explained by the strong dependency of the MBE grown N- and In-polar InN on the growth temperature, where N-polar InN might be grown at higher growth temperatures than In-polar InN [148, 149]. However, the other studies mentioned that the twinning formation of the ( $10\bar{1}3$ ) InN layers on (110) GaAs is also depended on the existence of H<sub>2</sub> gas (in this case, the InN layers were grown at 575°C) [146]. By mixing H<sub>2</sub> gas (0%-0.4%) into N<sub>2</sub> carrier gas during the growth processes of the ( $10\bar{1}3$ ) InN layers, the crystallite twinning increased with increasing H<sub>2</sub> ratio [146]. For the MOVPE growth of the InN layers on *m*-plane sapphire, the crystallite twinning of the layers are existed likely due to the low-temperature growth. Overall, suppression of the crystallite twinning of ( $10\bar{1}3$ ) InN is needed to improve the material properties.

## 6.2 Surface morphology and surface diffusion

Surface morphology of the InN layers was examined by atomic force microscopy (AFM) in contact mode. Figure 6.5 shows  $5\ \mu\text{m} \times 5\ \mu\text{m}$  AFM images of the InN layers grown on *m*-plane sapphire with different nitridation times. All the AFM images reveal three-dimensional (3D) growth structures with different grain sizes along the  $[30\bar{3}\bar{2}]_{\text{InN}}$  ( $[1\bar{2}10]_{\text{sapphire}}$ ) and the  $[1\bar{2}10]_{\text{InN}}$  ( $[0001]_{\text{sapphire}}$ ) directions. The grain sizes were estimated from the AFM images by averaging line profiles (Fig. 6.6). The grain size was varying from 50 to 250 nm along the  $[30\bar{3}\bar{2}]_{\text{InN}}$  ( $[1\bar{2}10]_{\text{sapphire}}$ ) direction, and about 80-500 nm along the  $[1\bar{2}10]_{\text{InN}}$  ( $[0001]_{\text{sapphire}}$ ) direction. The grain height was similar to the layer thickness of about 100-200 nm. The grain sizes of the InN layers showed a correlation with the FWHM values of the ( $10\bar{1}3$ ) InN XRC. The layers with larger grain sizes had smaller FWHM values along both the  $[30\bar{3}\bar{2}]_{\text{InN}}$  and the  $[1\bar{2}10]_{\text{InN}}$  directions (Fig. 6.7).

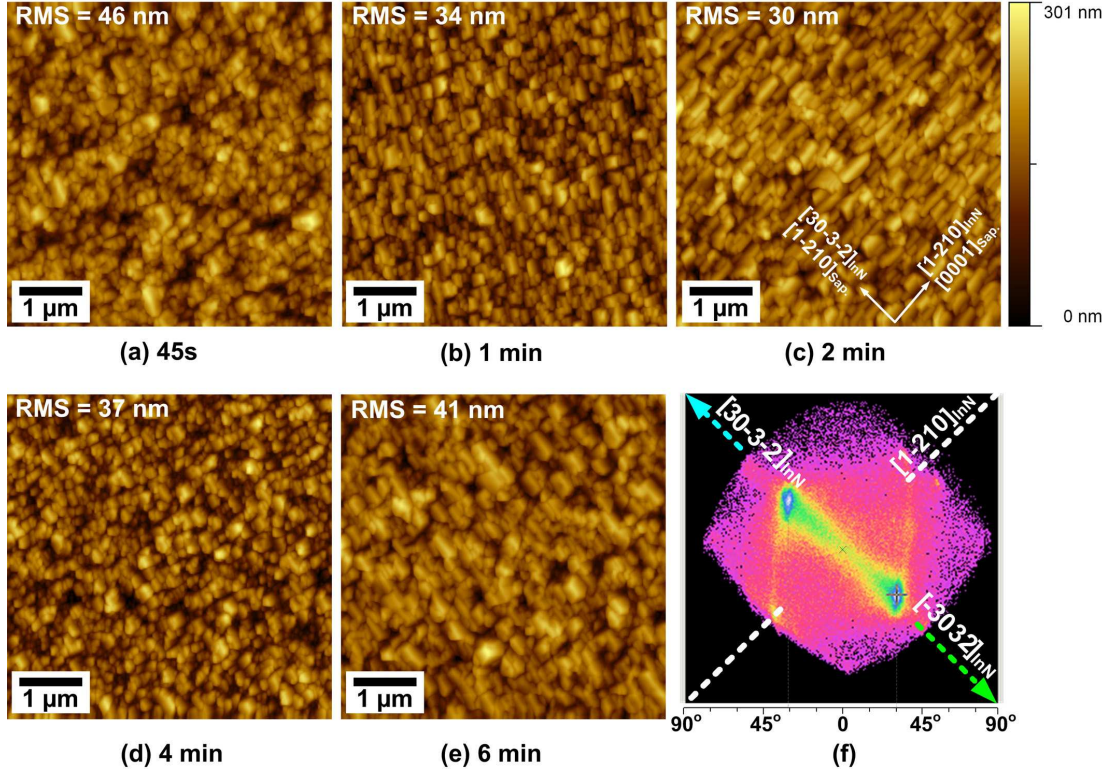


**Figure 6.5:**  $5\ \mu\text{m} \times 5\ \mu\text{m}$  AFM images and RMS roughness of the InN layers ( $\approx 250\ \text{nm}$ ) grown on  $m$ -plane sapphire with different nitridation times. Facet analysis (using GWYDDION software) of the InN layer in (c) shows two predominant facet distributions in two opposite directions with respect to the  $[1\bar{2}10]_{\text{InN}}$  ( $[0001]_{\text{sapphire}}$ ) direction. The center of the facet view corresponds to zero inclination and slopes in both the  $[30\bar{3}\bar{2}]_{\text{InN}}$  directions reach maximum values of  $\sim 34.5^\circ$ , indicating the  $(000\bar{1})$  InN planes with respect to the  $(10\bar{1}\bar{3})$  InN planes (Fig. 6.2).

Compared to the simultaneous grown InN layers on  $c$ -plane sapphire, the InN layers grown on  $m$ -plane sapphire showed very rough surface morphology. Facet analysis of the InN layer grown on  $m$ -plane sapphire (with 2 min nitridation) shows clearly two facet distributions in two opposite directions at a facet angle of  $34.5^\circ$  as shown in Fig. 6.5(f), at this sample the  $[000\bar{1}]$  direction is found. The occurrence of two  $(000\bar{1})$  facets in opposite in-plane directions is a result of the twinning. Therefore, each grain can be attributed to a different crystallite orientation. The very rough surface morphologies of the InN layers on  $m$ -plane were attributed to the crystallite twinning of the layers. Similar to  $c$ -plane InN layer with mixed polarity, the RMS roughness of the InN layers grown on  $m$ -plane also showed correlation with grain sizes, where the lowest RMS

## 6.2. Surface morphology and surface diffusion

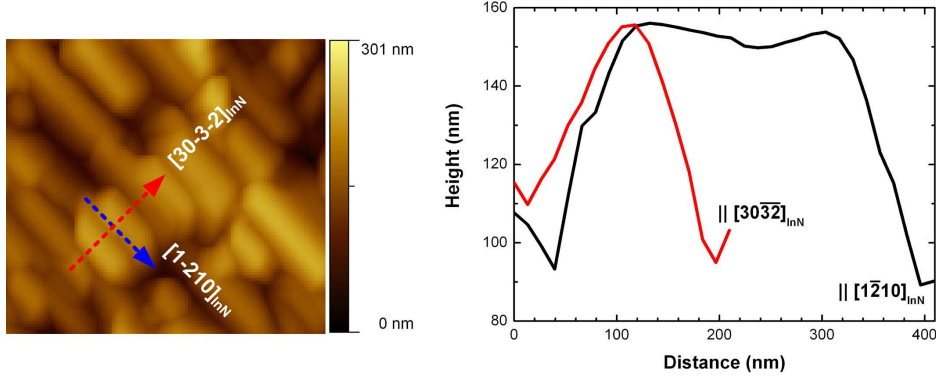


**Figure 6.6:** Line profiles of an InN structure on *m*-plane sapphire (Fig. 6.5(c)) show a grain size of 180 nm along the  $[30\bar{3}2]_{\text{InN}}$  direction and a grain size of 350 nm along the  $[\bar{1}2\bar{1}0]_{\text{InN}}$  direction.

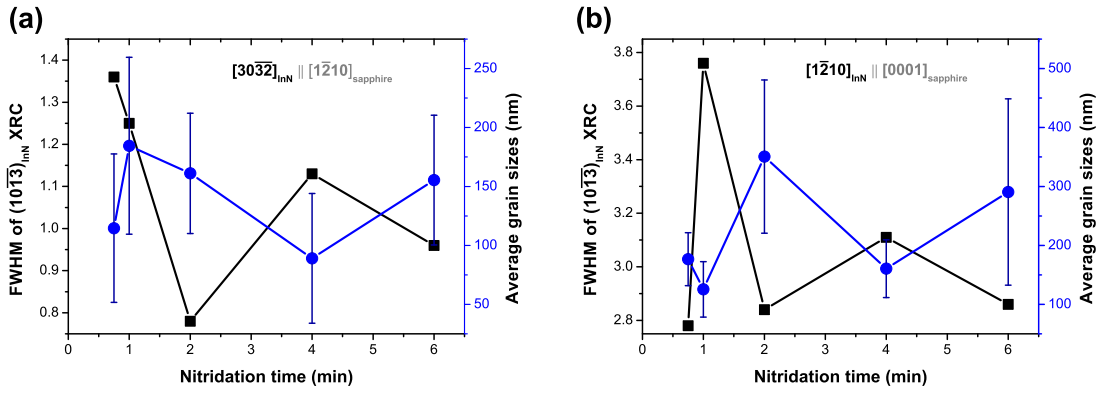


**Figure 6.7:** Average grain sizes (o) and FWHM values (□) of the  $(10\bar{1}\bar{3})_{\text{InN}}$  XRC along (a) the  $[30\bar{3}2]_{\text{InN}}$  direction and (b) the  $[\bar{1}2\bar{1}0]_{\text{InN}}$  direction plotted as functions of the nitridation time.

roughness of 30 nm can be found for the InN sample with largest grain size.

### 6.2.1 Effects of the nitridation on the surface morphology of InN

The nitridation process affects the crystallinity and the surface morphology of the InN layers, further studies were carried out on a series of bare nitridated *m*-plane sapphire substrates that were later performed in MOVPE for different times (45 s to 2 min) with the same nitridation condition. However, the grown AlN layers were very thin ( $\sim 1$  nm for 2 min nitridation), thus the growth orientation of the AlN layers could not be determined by XRD.

Figure 6.8 shows the surface morphology of an as-received *m*-plane sapphire, and

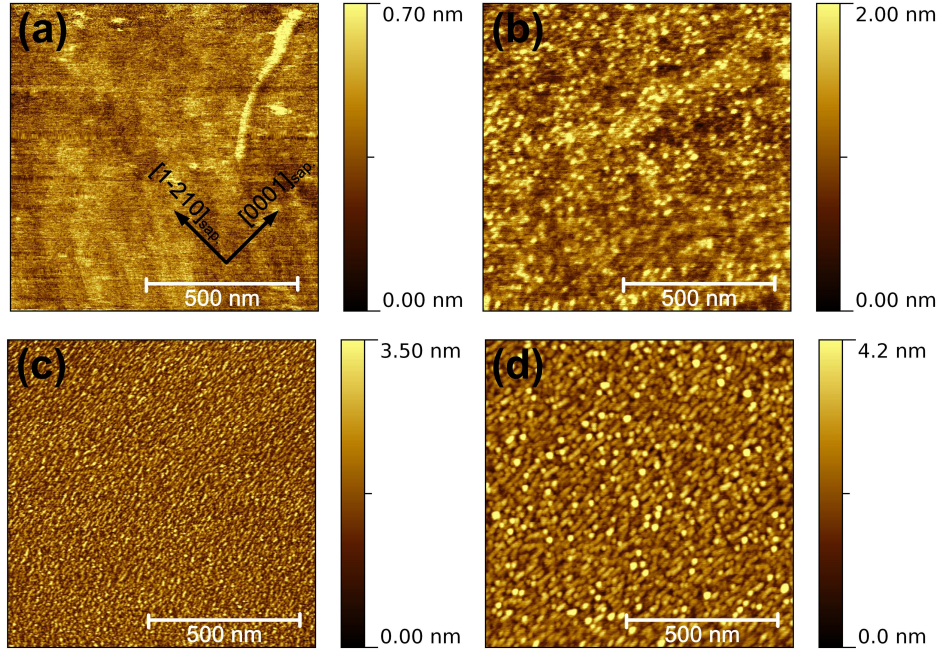


**Figure 6.8:**  $1\ \mu\text{m}\times 1\ \mu\text{m}$  AFM images of (a) an as-received  $m$ -plane sapphire substrate, and of the substrates after nitridation at  $1050^\circ\text{C}$  for (b) 45 s, (c) 1 min, and (d) 2 min.

the surface morphologies of  $m$ -plane sapphire substrates nitridated at  $1050^\circ\text{C}$  for different nitridation times. Prior the nitridation process, the  $m$ -plane sapphire substrate had a flat surface without islands (Fig. 6.8(a)). The RMS roughness and the height of the substrate were about 0.1 nm and 0.7 nm, respectively. After 45 s nitridation at  $1050^\circ\text{C}$  (Fig. 6.8(b)), many small islands appeared on the surface of  $m$ -plane sapphire. The islands were elongating along the  $[0001]_{\text{sapphire}}$  direction. When the nitridation times increased to 1 min and 2 min (Figs. 6.8(c) and (d)), the  $m$ -plane sapphire surface changed to a grainy surface containing uniform undulated islands/structures along the  $[\bar{1}210]_{\text{sapphire}}$  direction. The grain sizes of the islands/structures along the  $[\bar{1}210]_{\text{sapphire}}$  direction increased from  $\sim 10$  nm to  $\sim 20$  nm with increasing nitridation time from 1 min to 2 min, respectively. Additionally, the RMS values of the nitridated sapphire substrates increased with increasing nitridation times, 0.4 nm for 45 s, 0.6 nm for 1 min, and 0.7 nm for 2 min nitridation.

Since the nitridation layers (or AlN layers) were acting as buffer layers, the grain sizes and surface morphologies of the nitridation layers are the key parameters for the later growth of InN. Since the InN layers grown on 45 s and 1 min nitridated  $m$ -plane

## 6.2. Surface morphology and surface diffusion

---

sapphire showed many orientations, we expect to observe the same number of orientations on the nitridation layer. Thus, we assume the growth of incomplete nitridation layers at those times (Figs. 6.8(b) and (c)). The pure  $(10\bar{1}\bar{3})$  InN layers were grown after 2 min and 4 min nitridation of  $m$ -plane sapphire, therefore the pure  $(10\bar{1}\bar{3})$  AlN layers were formed at those times. Even though the surface morphology of the nitridated sapphire substrates got rougher, the grain size of islands also got larger, more uniform, and the islands covered the whole surface of  $m$ -plane sapphire. The large and uniform grain can enhance the nucleation of the InN growth. Overall, the InN layers might also replicate the surface morphology of the nitridation layers.

### 6.2.2 Surface diffusion

Base on the InN structure shown in Fig. 6.6, we propose the surface diffusion of In-atoms on the  $(10\bar{1}\bar{3})$  InN surface. Similar to the polar  $c$ -plane surface, the diffusion process of atoms on the semi- and non-polar surfaces of III-nitrides strongly affects not only the growth rate, but also quality, and surface morphology of the layer. The bonding configurations of III-nitride surface consist of the weak metallic bond (i.e., Ga-Ga or In-In) and the strong covalent bond (i.e., Ga-N or In-N). Unlike on other III-V semiconductors such as GaAs [150], Ga-atoms showed a strong stabilization on the  $c$ -plane GaN surface, so that the interaction of surface adatoms is dominated by delocalization of the metallic Ga-Ga bonds giving the isotropic diffusion barriers for the  $(0001)$  and the  $(000\bar{1})$  surfaces of 0.4 eV and 0.2 eV, respectively [151, 152]. In contrast to the  $c$ -plane GaN/InN surfaces, the nonpolar  $a$ - and  $m$ -plane surfaces showed a strong dependence on specific geometry and stoichiometry of these surfaces due to the bonding configurations and the separation distance of two neighboring adsorption sites along the  $[0001]$  direction and the perpendicular direction as well [120, 121].

Density-functional theory calculations of Ga-/In-adatom kinetics on the  $m$ -plane GaN/InN surfaces (under metal-rich conditions) showed a large diffusion barrier along the  $[0001]_{\text{GaN/InN}}$  and the  $[11\bar{2}0]_{\text{GaN/InN}}$  directions [120, 121]. The surface diffusion barrier of Ga-/In-atoms on the  $m$ -plane GaN/InN surfaces along the  $[0001]_{\text{GaN/InN}}$  directions of 0.93 eV/1.30 eV is much larger than along the  $[1\bar{1}00]_{\text{GaN/InN}}$  directions of 0.21 eV/0.06 eV. This means that Ga-/In-atoms will diffuse faster along the  $[1\bar{1}00]_{\text{GaN/InN}}$  directions than along the  $[0001]_{\text{GaN/InN}}$  directions, leading to a formation of anisotropic surface morphology. The smaller diffusion barriers of Ga-/In-atoms along the  $[11\bar{2}0]_{\text{GaN/InN}}$

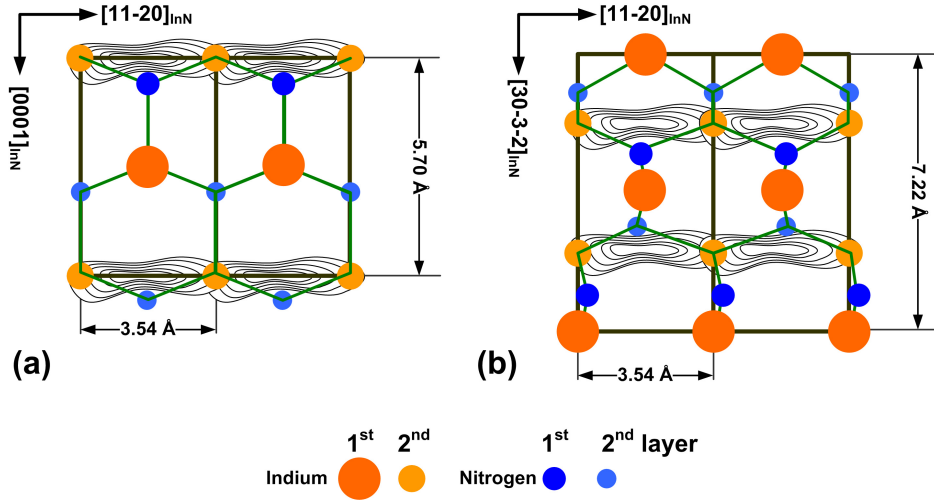


**Figure 6.9:** Unit cells ( $1 \times 2$ ) of (a) the relaxed nonpolar  $m$ -plane  $(1\bar{1}00)$  InN surface and (b) the relaxed semipolar  $(10\bar{1}\bar{3})$  InN surface. The contours indicate the pathway of indium adatom diffusions on these surfaces.

directions on the  $m$ -plane GaN/InN surfaces result in higher lateral growth rates (due to longer diffusion lengths) than those along the  $[0001]_{\text{GaN/InN}}$  directions. Figure 6.9(a) illustrates the diffusion pathways of Ga-/In-atoms on the  $m$ -plane GaN/InN surfaces as bridges (contour lines) between two adjacent Ga-N/In-N bonds.

In contrast to the nonpolar GaN/InN surfaces, the surface diffusion barriers of Ga-/In-atoms on the semipolar  $(10\bar{1}L)$  GaN/InN surfaces have not been yet studied. However, the semipolar  $(10\bar{1}L)$  InN surfaces (with  $L \neq 0$ ) show very similar surface atomic arrangements to the  $m$ -plane  $(1\bar{1}00)$  InN surface but with an additional tilt of  $\alpha$  angle ( $0^\circ < \alpha < 90^\circ$ ) with respect to the  $m$ -plane surface, as shown in Fig. 2.4). In case of the semipolar  $(10\bar{1}\bar{3})$  InN surface, the  $\alpha$  angle is  $\sim 58^\circ$  (see Figs. 2.4 and 6.2). The surfaces of  $m$ -plane and semipolar  $(10\bar{1}\bar{3})$  InN are shown in Fig. 6.9. Due to the comparable surface atomic arrangements to the  $m$ -plane surface, a similar trend for In-adatom diffusion on the semipolar  $(10\bar{1}\bar{3})$  surface is expected, i.e., a bridge of In-atoms on the surface as illustrated in Fig. 6.9(b). In-atoms diffusing on the  $(10\bar{1}\bar{3})$  InN surface along the  $[\bar{1}\bar{2}10]_{\text{InN}}$  direction might have a smaller diffusion barrier than along the  $[30\bar{3}\bar{2}]_{\text{InN}}$  direction. Moreover, In-atoms on the  $(10\bar{1}\bar{3})$  InN surface will move easily along the  $[\bar{1}\bar{2}10]_{\text{InN}}$  direction due to the weak metallic In-In bonds. In order to move the In-atoms along the  $[30\bar{3}\bar{2}]_{\text{InN}}$  direction, the strong covalent In-N bonds have to be broken and replaced by two rather weak metallic In-In bonds. Consequently, the

formation of anisotropic morphology of the InN layers is caused by the anisotropic diffusion of In-atoms on the  $(10\bar{1}\bar{3})$  InN surface (and on the other  $(10\bar{1}L)$  InN surfaces).

Additionally, due to the appearance of the  $(000\bar{1})$  InN surface (Fig. 6.5(f)), the diffusions of In-atoms are more complex. Similar to Ga-atoms on the  $c$ -plane GaN surface, In-atoms on the  $c$ -plane InN surface should have a very low diffusion barrier due to the weak metallic In-In bond. This enhances a faster In-incorporation along the  $[000\bar{1}]_{\text{InN}}$  direction than along the  $[30\bar{3}\bar{2}]_{\text{InN}}$  direction. However, the total surface diffusion barriers along both the  $[000\bar{1}]_{\text{InN}}$  and the  $[30\bar{3}\bar{2}]_{\text{InN}}$  directions are still smaller than along the  $[\bar{1}\bar{2}10]_{\text{InN}}$  direction, resulting in the smaller grain sizes in the  $[30\bar{3}\bar{2}]_{\text{InN}}$  direction (Figs. 6.6 and 6.7).

Even the surface diffusion of In-atoms on the semipolar  $(10\bar{1}L)$  InN surfaces is expected to show a similar trend to the  $m$ -plane GaN/InN surfaces. However, all those semipolar surfaces show different surface atomic arrangements, depending on the  $\alpha$  angle. This will affect the adatom kinetics of In-atoms on those semipolar surfaces, leading to the different growth rates and the surface morphologies of InN layers depending on the semipolar surface orientation. The extremely large diffusion barrier of In-atoms on the  $(10\bar{1}\bar{3})$  InN surface along the  $[30\bar{3}\bar{2}]_{\text{InN}}$  ( $[\bar{1}\bar{2}10]_{\text{sapphire}}$ ) direction compared to that along the  $[\bar{1}\bar{2}10]_{\text{InN}}$  ( $[0001]_{\text{sapphire}}$ ) (22 times larger, assuming that the  $(10\bar{1}\bar{3})$  surface was similar to the  $m$ -plane surface) might lead to the growth of 3D structure as well. Overall, the very rough morphology of the InN layers on  $m$ -plane sapphire compared to that of the simultaneously  $c$ -plane InN layers on  $c$ -plane sapphire is attributed to the crystallite twinning, the growth of the other orientations, as well as the anisotropic diffusion of In-atoms on the different surface orientations.

### 6.3 Optical properties

Low temperature photoluminescence (PL) measurements were carried out to investigate the optical properties of the InN layers on  $m$ -plane sapphire (Fig. 6.10). The PL spectrum of the  $c$ -plane InN layer on 2 min nitrated  $c$ -plane sapphire was also shown in Fig. 5.20. The PL measurements were carried out at 8K using a laser diode with an excitation source of 25 mW emitting at 405 nm wavelength. The PL signals were detected by a liquid-nitrogen cooled indium antimonide (InSb) photo-diode.

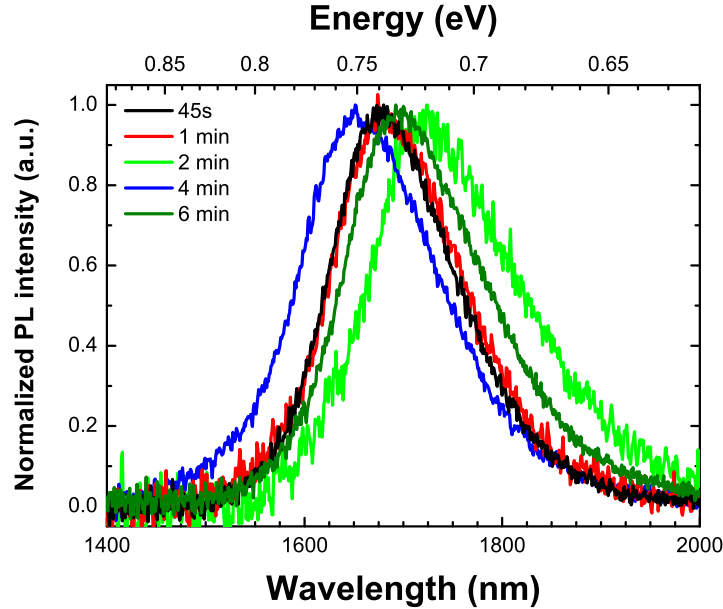


**Figure 6.10:** Low temperature photoluminescence spectra of the grown InN layers on *m*-plane sapphire with different nitridation times.

All the InN layers on *m*-plane sapphire showed a redshift of the PL peak energy compared to the *c*-plane InN on *c*-plane sapphire (see Fig. 5.20 in Chapter 5). For all the InN layers grown on *m*-plane sapphire, the PL peak energies were between 0.72 eV and 0.75 eV (Fig. 6.10), which were about 0.1-0.4 eV above the emission peak of the *c*-plane InN layer shown in Fig. 5.20. All the PL spectra had a similarly FWHM value of 57-67 meV (estimated by Gaussian fits). The redshifts of the PL peak energies of the InN layers grown on *m*-plane sapphire were also observed for semipolar ( $11\bar{2}2$ ) InN grown directly on *m*-plane sapphire [153] and nonpolar *m*-plane InN grown on *m*-plane GaN [154]. For the *m*-plane InN [154], the redshift was attributed to basal stacking faults.

The additional PL shifts were found for all the InN layers grown on the different nitridated *m*-plane sapphire substrates. The shifts of the PL peak energies can be caused by background doping, strain, or the different grain sizes of the InN layers on *m*-plane sapphire. Figure 6.11 shows the PL peak energies of the InN layers on *m*-plane sapphire as a function of the grain sizes. A correlation between the shifts of the PL peak energies and the grain sizes was found, where larger grain sizes correspond to lower PL peak energies.

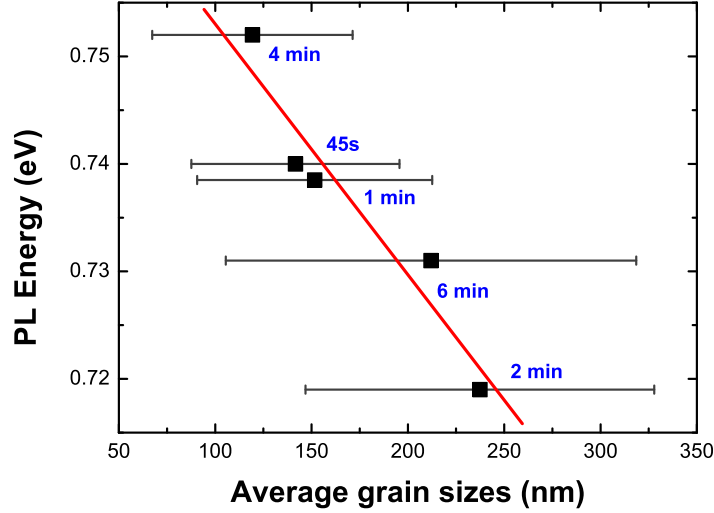


**Figure 6.11:** PL peak energies of the InN layers on  $m$ -plane sapphire plotted as a function of average grain sizes.

Since the InN layers grown on  $m$ -plane sapphire consist of islands, the background doping can not be estimated. However, as discussed in Section 5.3.4, hydrogen, oxygen, and carbon are unintentionally incorporated in the InN growth due to the low growth temperatures. The incorporation of the unintentional impurities might cause the shifts of the PL peak energies of the InN layers [129]. Similar to hydrogen [127, 128], oxygen and carbon are expected to show different amounts of incorporation for all the surface orientations (i.e.,  $Impurities_{(0001)} < Imp_{(000\bar{1})} < Imp_{(10\bar{1}1)} < Imp_{(11\bar{2}0)}$ ). The layer with smaller grain size should incorporate more impurities since the impurities are mostly residing along grain boundaries [128]. Thus the impurities might cause the shifts of the PL peak energies of the InN layers on  $m$ -plane sapphire (Figs. 6.10 and 6.11).

## 6.4 Chapter summary

The nitridation process of  $m$ -plane sapphire is very important not only to control the growth orientation of InN but also to improve material properties. Nitridating  $m$ -plane sapphire at 1050°C for 2-4 min leads to the growth of pure  $(10\bar{1}\bar{3})$  InN. The  $(10\bar{1}\bar{3})$  InN layers grown on  $m$ -plane sapphire had crystallite twinning (along  $[1\bar{2}10]_{\text{sapphire}}$  and  $[\bar{1}2\bar{1}0]_{\text{sapphire}}$ ) due to the equalities of the growth of thin  $(10\bar{1}\bar{3})$  AlN layers on  $m$ -plane sapphire via nitridation process. Crystallite twinning was observed for the  $(10\bar{1}\bar{3})$  InN layers on  $m$ -plane sapphire, which partially attributed to the very rough

## Chapter 6. Semipolar ( $10\bar{1}\bar{3}$ ) InN

---

surface morphology, the structural anisotropy, and the optical properties of the layers. The anisotropic surface morphologies of the InN layers on the nitridated  $m$ -plane sapphire substrates not only replicated the surface morphologies of the nitridated  $m$ -plane sapphire substrates, but also were caused by the anisotropic diffusion of In-atoms on the ( $10\bar{1}\bar{3}$ ) InN surface. All the grown InN layers on  $m$ -plane sapphire showed PL peak energies between 0.72 eV and 0.75 eV and had redshifts of 0.1-0.4 eV compared to  $c$ -plane InN. The shifts of the PL peak energies of the InN layers on  $m$ -plane sapphire correlated with the grain sizes of the layers, where larger grain sizes correspond to lower PL peak energies.

## 6.4. Chapter summary

---

## Chapter 7

# Semipolar $(11\bar{2}2)$ InN

As shown in Chapter 6, the semipolar  $(10\bar{1}\bar{3})$  InN layers showed very different material properties compared to  $c$ -plane InN. However, the phase purity and domain size of the  $(10\bar{1}\bar{3})$  InN layers are very sensitive to the nitridation process. The crystallite twinning of the  $(10\bar{1}\bar{3})$  InN layers causes a very rough surface morphology and limits further investigations for the layers. Growth of pure semipolar InN layers without twins is required for a successful application. Therefore, investigation of the material properties and the growth process of high quality semipolar InN layers is needed.

This chapter deals with the MOVPE growth and characterizations of semipolar  $(11\bar{2}2)$  InN layers. The focus will be put on the growth strategy and the effect of different growth temperatures on the material properties of the  $(11\bar{2}2)$  InN layers.

### 7.1 *In-situ* growth monitoring

The growth parameters of the  $(11\bar{2}2)$  InN layers grown on  $(11\bar{2}2)$  GaN templates on  $m$ -plane sapphire were similar to those of the InN layers grown on  $(0001)$  GaN templates shown in Section 3.5. The  $(11\bar{2}2)$  GaN templates were grown on  $m$ -plane sapphire using MOVPE (a Thomas Swan close coupled shower-head reactor) by Simon Ploch at the Technical University of Berlin [144, 156].

The growth process was monitored by the *in-situ* spectroscopic ellipsometry (SE) with a photon energy range of 1.6 eV - 6.5 eV. Figure 7.1 shows the imaginary parts  $\langle\epsilon_2\rangle$  of pseudo-dielectric functions recorded *in-situ* at room temperature on a  $(11\bar{2}2)$  GaN template before and after the InN growth. The incident angle was  $\sim 67.5^\circ$  along the

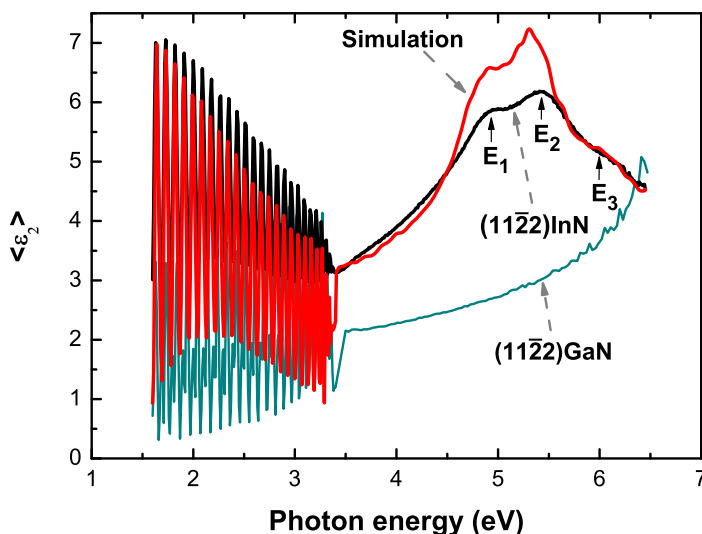


**Figure 7.1:** Imaginary parts of the effective dielectric functions of the  $(11\bar{2}2)$  GaN template (dark-green curve) after loading to the reactor, and of a  $(11\bar{2}2)$  InN layer (black curve) grown at  $540^\circ\text{C}$  on the  $(11\bar{2}2)$  GaN template on  $m$ -plane sapphire. The spectra were recorded *in-situ* at room temperature (after growth in the case of InN) along the  $[1\bar{1}00]_{\text{InN, GaN}}$  directions. The incident angle was  $\sim 67.5^\circ$ . Red curve shows the best fit, assuming 4 nm RMS roughness of  $2.8\ \mu\text{m}$ -thick  $(11\bar{2}2)$  GaN template and 4 nm RMS roughness of a 70 nm-thick  $(11\bar{2}2)$  InN layer.

$[1\bar{1}00]_{\text{GaN, InN}}$  directions. The  $\langle \epsilon_2 \rangle$  spectrum of the InN layer showed clearly three inter-band transition energies denoted as  $E_1$  ( $\sim 4.9\ \text{eV}$ ),  $E_2$  ( $\sim 5.3\ \text{eV}$ ), and  $E_3$  ( $\sim 6.1\ \text{eV}$ ), which are similar to those of the InN layers on  $c$ - and  $m$ -plane sapphire shown in Fig. 3.12. The comparability of these spectra indicates the successful growth of InN on the  $(11\bar{2}2)$  GaN template. The intensity of the  $E_2$  inter-band transition energy (as well as  $E_1$  and  $E_3$ ) of the  $\langle \epsilon_2 \rangle$  spectra decreased with increasing growth temperatures (Fig. 7.2), indicating the grown InN layers might become rougher morphology or exhibit a higher defect density at higher growth temperatures.

Thickness simulations were performed using a six-layer model (sapphire, GaN, root-mean square (RMS) roughness of GaN, InN, RMS roughness of InN, air/vacuum) by the commercial software LayTec AnalysR [157]. Because the dispersion data for semipolar InN is not known, the simulations were based on the dispersion data for  $m$ -plane GaN [158] and  $m$ -plane InN [159]. Despite these limitations, a reliable mean thickness of about 90 nm and a mean roughness of about 4 nm were obtained for the InN sample grown on the  $(11\bar{2}2)$  GaN template in Fig. 7.1. The thicknesses of the InN layers grown

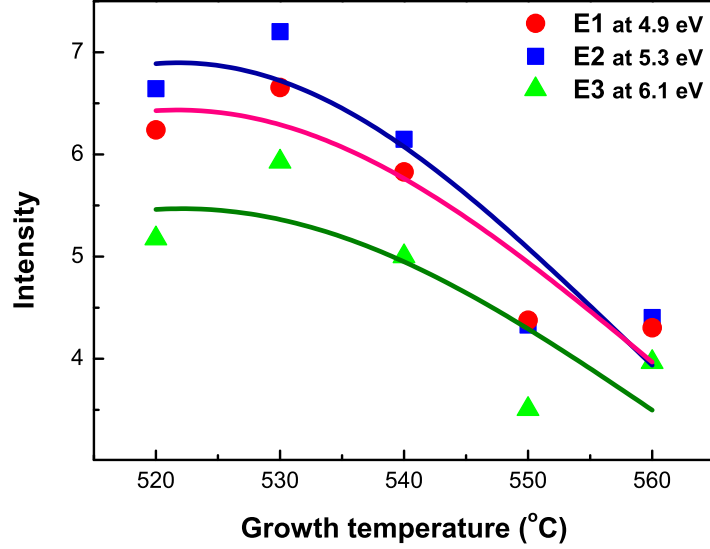


**Figure 7.2:** Intensity of the  $E_1$ ,  $E_2$ , and  $E_3$  inter-band transition energies of the  $\langle\epsilon_2\rangle$  spectra (Fig. 7.1) of the  $(11\bar{2}2)$  InN layers grown on the  $(11\bar{2}2)$  GaN templates at different temperatures.

on the  $(11\bar{2}2)$  GaN templates were about 90-150 nm with a thickness variation of 20 nm (determined by TEM), and were 3-4 times thinner than the ones for the simultaneous  $c$ -plane InN layers grown on the  $c$ -plane GaN templates (Section 5.3).

## 7.2 Crystallinity and in-plane relationship

Figure 7.3 shows the symmetric XRD  $\omega$ - $2\theta$  scans of the  $(11\bar{2}2)$  GaN template and an InN sample grown at 560°C. The plane of incidence was calibrated along the  $[0001]$  axis of the  $m$ -plane sapphire substrate. Only a single reflection corresponding to the  $(11\bar{2}2)$  reflection of semipolar InN was found.

The epitaxial in-plane relationships of the grown  $(11\bar{2}2)$  InN layers, the  $(11\bar{2}2)$  GaN templates, and  $m$ -plane sapphire were determined from XRD off-axis  $\phi$ -scans. The skew-symmetric  $(20\bar{2}4)$  reflection of  $m$ -plane sapphire substrate was measured with a tilt angle of  $32.38^\circ$ , which indicates the  $[000\bar{1}]$  direction of  $m$ -plane sapphire at a  $\phi$  angle of  $-90^\circ$  (Fig. 7.4). To determine in-plane direction of  $(11\bar{2}2)$  InN and  $(11\bar{2}2)$  GaN, the skew-symmetric  $(0002)$  reflections of the  $(11\bar{2}2)$  InN and  $(11\bar{2}2)$  GaN layers were measured with tilt angles of  $58.14^\circ$  and  $58.41^\circ$ , respectively. Figure 7.4 shows the skew-symmetric  $(0002)$  reflections of the  $(11\bar{2}2)$  InN and  $(11\bar{2}2)$  GaN layers rotated by  $180^\circ$

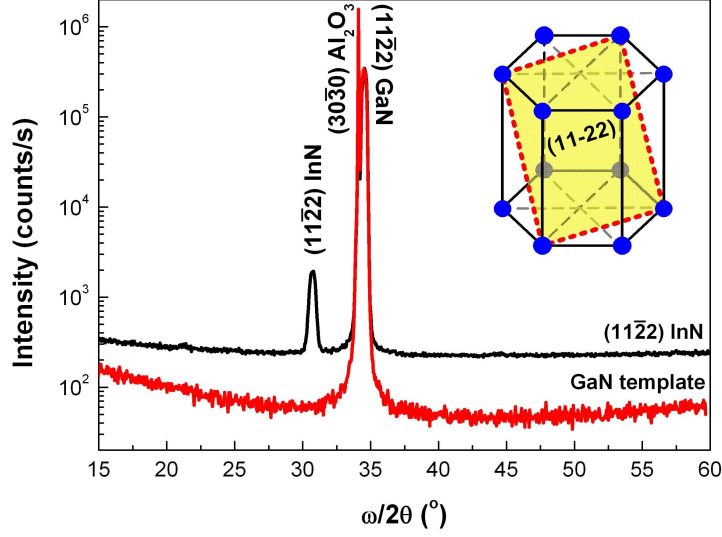


**Figure 7.3:** Symmetric XRD  $\omega$ - $2\theta$  scans of an InN layer grown on an  $m$ -plane sapphire substrate with a  $(11\bar{2}2)$  GaN buffer layer, and of the bare  $(11\bar{2}2)$  GaN template

with respect to the  $(20\bar{2}4)$  reflection of  $m$ -plane sapphire substrate. Only one reflection was found for the  $(11\bar{2}2)$  InN, indicating that no twinning occurred for  $(11\bar{2}2)$  InN in contrast to the InN layers grown directly on  $m$ -plane sapphire (see Chapter 6). The in-plane relationship is  $[1\bar{1}00]_{\text{InN}} \parallel [1\bar{1}00]_{\text{GaN}} \parallel [1\bar{2}10]_{\text{sapphire}}$  and  $[\bar{1}\bar{1}23]_{\text{InN}} \parallel [\bar{1}\bar{1}23]_{\text{GaN}} \parallel [0001]_{\text{sapphire}}$  (or  $[11\bar{2}\bar{3}]_{\text{InN}} \parallel [11\bar{2}\bar{3}]_{\text{GaN}} \parallel [0001]_{\text{sapphire}}$ ). The in-plane relationship of the grown  $(11\bar{2}2)$  InN with respect to  $m$ -plane sapphire was illustrated in Fig. 7.4(b). The InN layers reproduced the orientations of the  $(11\bar{2}2)$  GaN templates [160, 161], and had the same relationship as  $(11\bar{2}2)$  InN layer grown directly on  $m$ -plane sapphire [153]. The in-plane relationship of  $(11\bar{2}2)$  InN/GaN with respect to  $m$ -plane sapphire indicates that the  $[\bar{1}\bar{1}23]$  direction (projection of the  $c$ -axis to growth plane, i.e.,  $c'$ ) of the  $(11\bar{2}2)$  InN/GaN layer were paralleled to the  $[0001]_{\text{sapphire}}$  direction. This alignment is different to the  $(10\bar{1}\bar{3})$  InN layer on  $m$ -plane sapphire, where the  $(10\bar{1}\bar{3})$  InN structures were crystallographically equivalent to the  $[1\bar{2}10]_{\text{sapphire}}$  and the  $[\bar{1}2\bar{1}0]_{\text{sapphire}}$  directions causing crystallite twinning (Fig. 6.3 and Ref. 162).

Structural anisotropy was observed for the  $(10\bar{1}\bar{3})$  InN layers on  $m$ -plane sapphire by XRD [162]. For precise investigation of the anisotropy in  $(11\bar{2}2)$  InN layers, reciprocal space maps (RSM) were performed along both in-plane directions of the  $[0001]_{\text{sapphire}}$  ( $[\bar{1}\bar{1}23]_{\text{InN}}$ ) and the  $[1\bar{2}10]_{\text{sapphire}}$  ( $[1\bar{1}00]_{\text{InN}}$ ). Figures 7.5(a) and 7.5(c) show the symmetric  $(11\bar{2}2)$  InN and  $(11\bar{2}2)$  GaN reflections along the  $[0001]_{\text{sapphire}}$  and

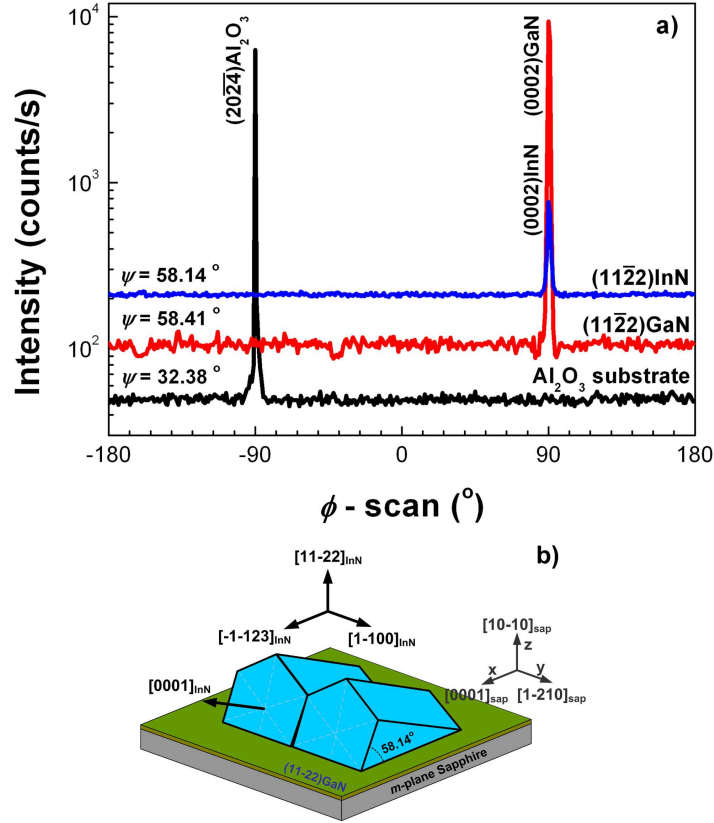


**Figure 7.4:** (a) XRD off-axis  $\phi$ -scans with settings for the  $(0002)$  reflections of  $(11\bar{2}2)$  InN and  $(11\bar{2}2)$  GaN performed in skew-symmetry, respectively, and of the  $(20\bar{2}4)$  reflection of  $m$ -plane sapphire. (b) Resulting epitaxial in-plane relationships of  $(11\bar{2}2)$  InN grown on  $m$ -plane sapphire substrate show the main growth directions related to the substrate.

the  $[1\bar{2}10]_{\text{sapphire}}$  in-plane directions, respectively. Only one  $(11\bar{2}2)$  InN/GaN reflection was observed in both symmetric RSM scans. That confirms the in-plane relationship in Fig. 7.4(b). In order to check the strain state of the  $(11\bar{2}2)$  InN layers, asymmetric RSM scans were performed in both perpendicular directions. Figure 7.5(b) shows the asymmetric  $(\bar{2}\bar{1}33)$  reflections ( $\phi = 90^\circ$ ) along the  $[0001]_{\text{sapphire}}$  direction, while Fig. 7.5(d) shows the asymmetric  $(11\bar{2}4)$  reflections ( $\phi = 90^\circ$ ) along the  $[1\bar{2}10]_{\text{sapphire}}$  direction. The dashed lines in Figs. 7.5(b) and 7.5(d) shows the relaxed and the strained positions, indicating the  $(11\bar{2}2)$  InN layer is fully relaxed along all crystal directions. Schematic descriptions of the in-plane crystalline structures at the relaxed surfaces of  $(11\bar{2}2)$  InN,  $(11\bar{2}2)$  GaN, and  $m$ -plane sapphire are illustrated in Fig. 7.6.

The RSM of the  $(11\bar{2}2)$  InN and  $(11\bar{2}2)$  GaN layers indicates an in-plane structural

## 7.2. Crystallinity and in-plane relationship

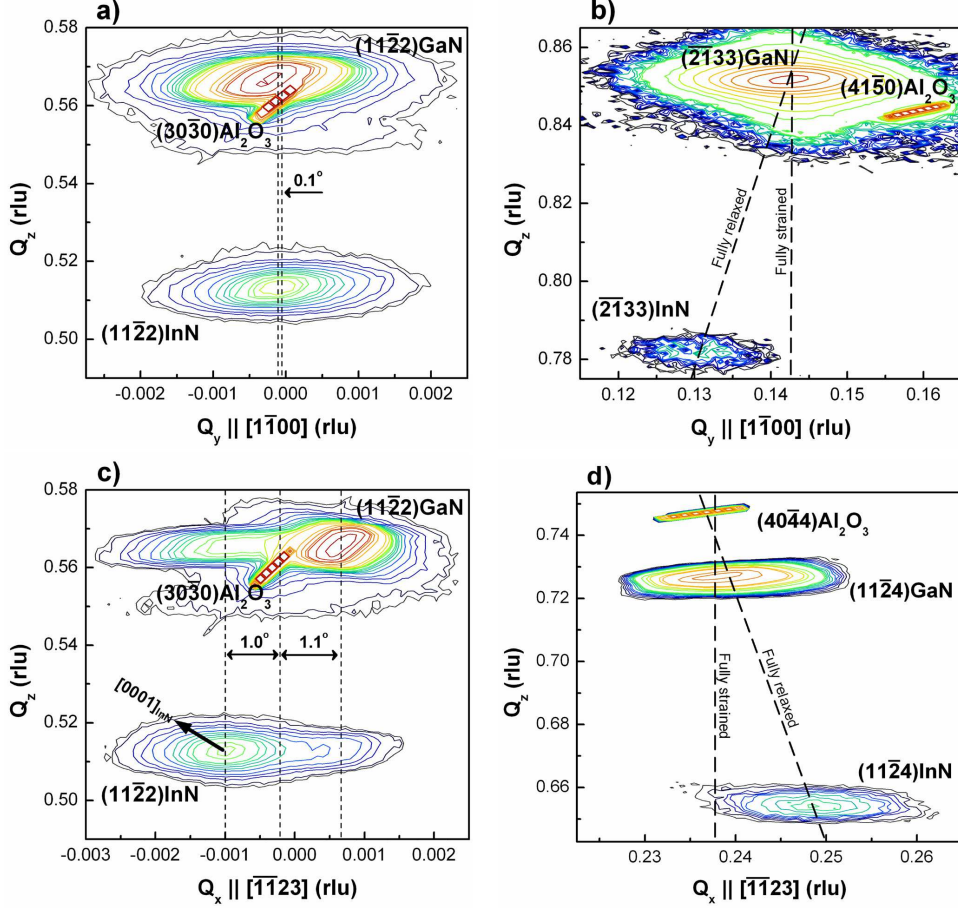


**Figure 7.5:** Reciprocal space maps of the  $(11\bar{2})$  InN layer grown at  $540^\circ\text{C}$  on the  $(11\bar{2})$  GaN template on  $m$ -plane sapphire: (a) and (b) symmetric  $(11\bar{2})$  and asymmetric  $(\bar{2}133)$  reflections along the  $[\bar{1}\bar{1}23]_{\text{InN}}$  (or  $[0001]_{\text{sapphire}}$ ) direction, respectively; (c) and (d) symmetric  $(11\bar{2})$  and asymmetric  $(11\bar{2}4)$  reflections along the  $[\bar{1}\bar{1}00]_{\text{InN}}$  (or  $[\bar{1}\bar{2}10]_{\text{sapphire}}$ ) direction, respectively.

anisotropy in the  $[0001]_{\text{sapphire}}$  and the  $[\bar{1}\bar{2}10]_{\text{sapphire}}$  directions due to the different broadening (Figs. 7.5(a) and 7.5(c)), similar to the  $(10\bar{1}\bar{3})$  InN layer on  $m$ -plane sapphire (Fig. 6.3). Generally, broadening of the reciprocal lattice points of semi- and non-polar III-nitrides is attributed to different types of defects, anisotropic strain and mosaicity, i.e., crystalline rotations of  $(11\bar{2})$  InN and  $(11\bar{2})$  GaN along the  $[\bar{1}\bar{1}23]$  direction [167, 168]. The crystallite tilt distributions can be seen in the symmetric  $(11\bar{2})$  InN/GaN reflections due to the broadenings along the  $[\bar{1}\bar{1}23]_{\text{InN,GaN}}$  directions in Fig. 7.5(c). Additionally, a broadening in the RSM along the  $[0001]_{\text{GaN}}$  direction was found in all  $(11\bar{2})$  GaN samples. This broadening is associated with the presence of basal stacking

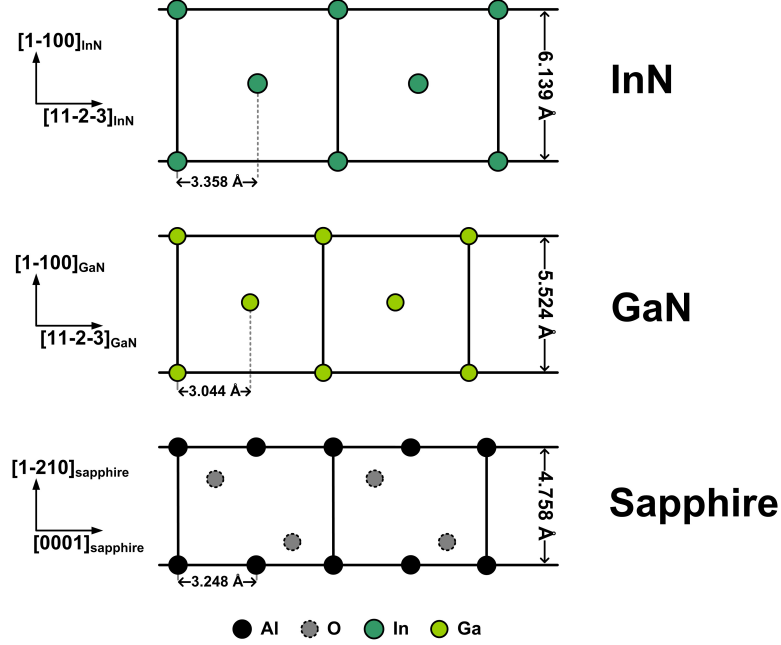


**Figure 7.6:** Schematic illustrations of the in-plane crystalline structures at the relaxed surfaces of  $(11\bar{2}2)$  InN,  $(11\bar{2}2)$  GaN, and  $m$ -plane sapphire.

faults (BSFs) and partial dislocations (PDs) [167, 168]. However, for the  $(11\bar{2}2)$  InN layers, the broadening along the  $[0001]_{\text{InN}}$  direction was less (Fig. 7.5(c)). Since the  $(11\bar{2}2)$  InN layers were tilted, the tilt may induce a rotation of the asymmetric RSM, i.e., from an unrelaxed position to the relaxed position.

The full width at half maximum (FWHM) of  $(11\bar{2}2)$  InN X-ray rocking curves (XRC) were determined from the RSM along the  $[\bar{1}\bar{1}23]_{\text{InN}}$  (or  $[0001]_{\text{sapphire}}$ ) and the  $[1\bar{1}00]_{\text{InN}}$  (or  $[1\bar{2}10]_{\text{sapphire}}$ ) directions shown in Fig. 7.7. The FWHM values were about  $1.26$ - $1.80^\circ$  along the  $[1\bar{2}10]_{\text{InN}}$  direction, and about  $1.65$ - $2.15^\circ$  along the  $[30\bar{3}\bar{2}]_{\text{InN}}$  direction (Fig. 7.7). The FWHM values of the XRC of the  $(11\bar{2}2)$  InN layers along the  $[\bar{1}\bar{1}23]_{\text{InN}}$  and the  $[1\bar{1}00]_{\text{InN}}$  directions increased with increasing growth temperatures, corresponding to a decrease of crystallinity.

The  $(11\bar{2}2)$  GaN templates and the  $(11\bar{2}2)$  InN layers show much larger values of tilt angles ( $\sim 1.0^\circ$ ) along the  $[1\bar{2}10]_{\text{sapphire}}$  and  $[\bar{1}\bar{2}\bar{1}0]_{\text{sapphire}}$  directions than those ( $\sim 0.1^\circ$ ) along the  $[0001]_{\text{sapphire}}$  and  $[000\bar{1}]_{\text{sapphire}}$  directions (Fig. 7.5 and Table 7.1). The same tilting values were also observed for the  $(10\bar{1}\bar{3})$  InN layer on  $m$ -plane sapphire (Fig. 6.3). The origin of the different tilts is the equivalence of bond configurations along the

## 7.2. Crystallinity and in-plane relationship

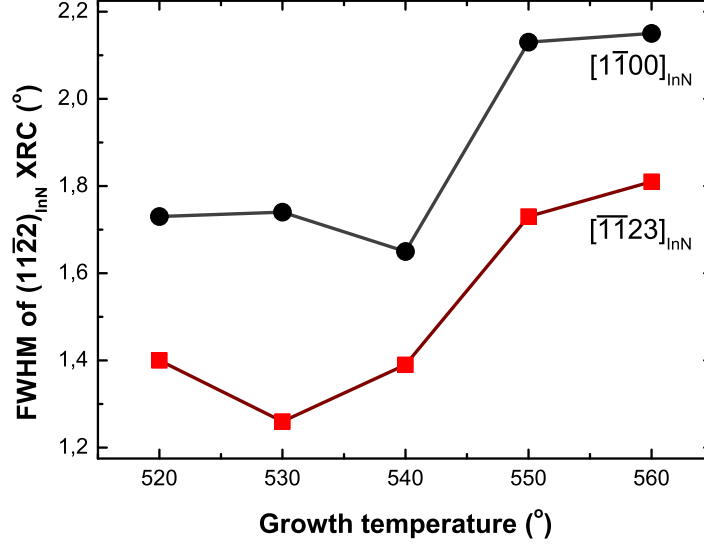


**Figure 7.7:** The FWHM values of the  $(11\bar{2}2)$  X-ray rocking curves of the  $(11\bar{2}2)$  InN layers scanned along the  $[\bar{1}\bar{1}23]_{\text{InN}}$  and the  $[1\bar{1}00]_{\text{InN}}$  directions.

$[1\bar{1}00]$  and  $[\bar{1}100]_{\text{InN}}$  directions allowing tilts along both the  $[0001]$  and  $[000\bar{1}]_{\text{InN}}$  equivalently. However, bond configurations in  $[\bar{1}\bar{1}23]_{\text{InN}}$  and  $[11\bar{2}\bar{3}]_{\text{InN}}$  directions are highly anisotropic (Fig. 7.6 and Table 7.1).

The difference in these tilting values of GaN and InN may also relate to different lattice tilts, different defect density, growth conditions and surface morphology, or strain relaxation at the InN/GaN and GaN/sapphire surfaces. The tilts of the layers might relate to lattice tilts since the  $(11\bar{2}2)$  InN and the  $(11\bar{2}2)$  GaN layers were grown on vicinal substrates (InN on  $(11\bar{2}2)$  GaN, and  $(11\bar{2}2)$  GaN on  $m$ -plane sapphire) containing

**Table 7.1:** Tilt angles along the  $[\bar{1}\bar{1}23]_{\text{InN, GaN}}$  directions towards the  $[1\bar{2}10]_{\text{sapphire}}$  direction (“-” sign) and the  $[\bar{1}2\bar{1}0]_{\text{sapphire}}$  direction (“+” sign). Tilt angles along the  $[1\bar{1}00]_{\text{InN, GaN}}$  directions towards the  $[000\bar{1}]_{\text{sapphire}}$  direction (“-” sign) and the  $[0001]_{\text{sapphire}}$  direction (“+” sign).

Samples	Tilt angle (°)			
	$[\bar{1}\bar{1}23]_{\text{InN}}$	$[1\bar{1}00]_{\text{InN}}$	$[\bar{1}\bar{1}23]_{\text{GaN}}$	$[1\bar{1}00]_{\text{GaN}}$
520 °C	0.0	+1.2	-0.2	-1.1
530 °C	+0.1	-1.2	0.0	+1.1
540 °C	-0.1	+1.0	+0.2	-1.1
550 °C	0.0	-1.0	+0.2	+1.1
560 °C	+0.3	+1.0	+0.1	-1.1

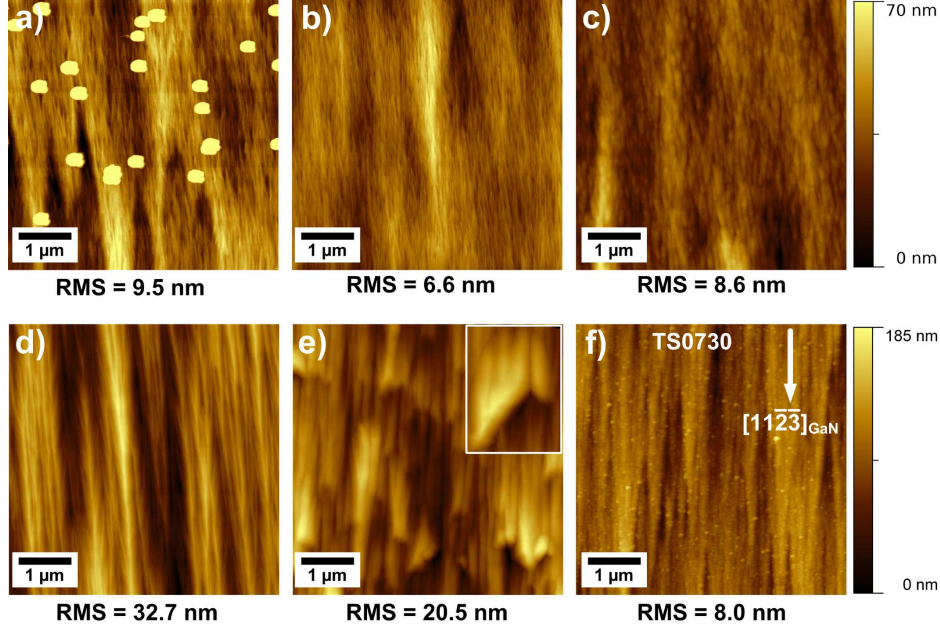


**Figure 7.8:**  $5\ \mu\text{m} \times 5\ \mu\text{m}$  AFM images (and corresponding root-mean square (RMS) roughness) of the  $(11\bar{2}2)$  InN layers grown on (f) the bare GaN templates at different temperatures (a)  $520^\circ\text{C}$ , (b)  $530^\circ\text{C}$ , (c)  $540^\circ\text{C}$ , (d)  $550^\circ\text{C}$ , and (e)  $560^\circ\text{C}$ . The RMS roughness of the InN layer grown at  $520^\circ\text{C}$  was extracted excluding indium droplets (white dots). The *inset* of (e) shows an island with the horizontal size of  $0.7\ \mu\text{m}$  and the vertical size of  $1.5\ \mu\text{m}$ .

surface steps (shown later in Fig. 7.10). Additionally, the tilts of the layers might relate to the appearance of the high density of the misfit dislocations as observed at the hetero-interfaces of  $(11\bar{2}2)$  (Al,In)GaN on  $(11\bar{2}2)$  GaN template [139, 164, 165]. Both the high density of the misfit dislocations [139, 140, 164–166] and the lattice tilts [140] can minimize the elastic strain energy at the hetero-interface of InN/ $(11\bar{2}2)$  GaN, resulting in the fully strain relaxation of the  $(11\bar{2}2)$  InN layers (Fig. 7.5).

### 7.3 Surface morphology and surface diffusion

The morphology of the InN samples was investigated using atomic force microscopy (AFM) in contact mode. AFM images of all the  $(11\bar{2}2)$  InN layers show smooth planar surfaces with an undulation along the  $[1\bar{2}10]_{\text{sapphire}}$  direction (or  $[1\bar{1}00]_{\text{InN,GaN}}$ ) (Fig. 7.8), qualitatively similar to the morphology of the  $(11\bar{2}2)$  GaN templates. The root-mean square (RMS) roughness of  $5\ \mu\text{m} \times 5\ \mu\text{m}$  was found to be between 6 nm and 20 nm similar to the RMS roughness of the  $(11\bar{2}2)$  GaN templates. Similar to the si-

### 7.3. Surface morphology and surface diffusion

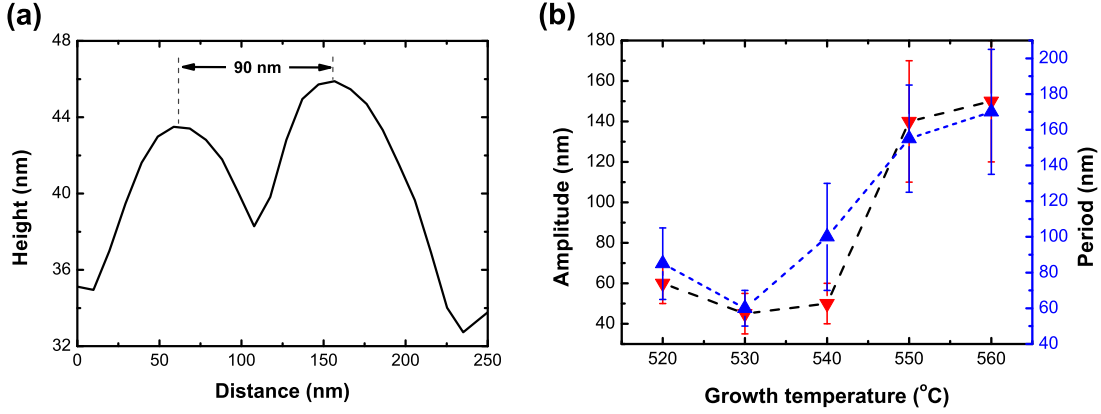


**Figure 7.9:** (a) A line profile along the  $[1\bar{1}00]_{\text{InN}}$  direction crossing two undulations on the surface of the  $(11\bar{2}2)$  InN grown at 540°C. An amplitude of  $\sim 45$  nm and a period of  $\sim 90$  nm were determined. The undulations have a trapezoidal-like (or cone-like) shape with a side-edge angle of  $(25 \pm 2)^\circ$ . (b) Undulation parameters (period ( $\Delta$ ) and amplitude ( $\nabla$ )) of the  $(11\bar{2}2)$  InN layers grown at different temperatures. The period and amplitude of the undulation of the  $(11\bar{2}2)$  GaN templates were  $(50 \pm 10)$  nm and  $(150 \pm 30)$  nm, respectively.

multaneously grown  $c$ -plane InN layers on  $c$ -plane GaN templates (Fig. 5.14), the RMS roughness of the semipolar InN layers slightly increased with increasing growth temperatures (Fig. 7.8). An increasing RMS roughness was found also on the simultaneously grown  $c$ -plane InN layers on  $c$ -plane GaN templates (Fig. 5.14). Only at a growth temperature of 520°C, metallic indium droplets were formed on the semipolar InN surface (Fig. 7.8(a)), likely caused by insufficient  $\text{NH}_3$  decomposition at this temperature. However, XRD shows the presence of metallic indium for all simultaneously grown  $c$ -plane InN layers on  $c$ -plane GaN templates (Fig. 5.10).

Amplitude and period of the undulation were averaged from line profiles crossing two adjacent undulations. Figure 7.9(b) shows an example of a line profile along the  $[1\bar{1}00]_{\text{InN}}$  direction crossing two undulations on the  $(11\bar{2}2)$  InN surface grown at 540°C. The amplitude and period of the undulations increased with increasing growth temperatures (Fig. 7.9(b)). A similar trend was also found for the  $(11\bar{2}2)$  GaN templates [169]. The morphology (RMS roughness and undulation parameters) corresponds also to the FWHM values of the  $(11\bar{2}2)$  InN XRC scans of the grown  $(11\bar{2}2)$  InN layers (Fig. 7.7). Smaller undulation parameters (amplitude and period) and smaller RMS roughness correlate with smaller FWHM values of the XRC (Figs. 7.7 and 7.9). Both results were comparable with the ellipsometry results (Fig. 7.2), i.e., the intensity of the  $E_2$  inter-band transition energy of the  $\langle \epsilon_2 \rangle$  spectra also decreased with increasing growth

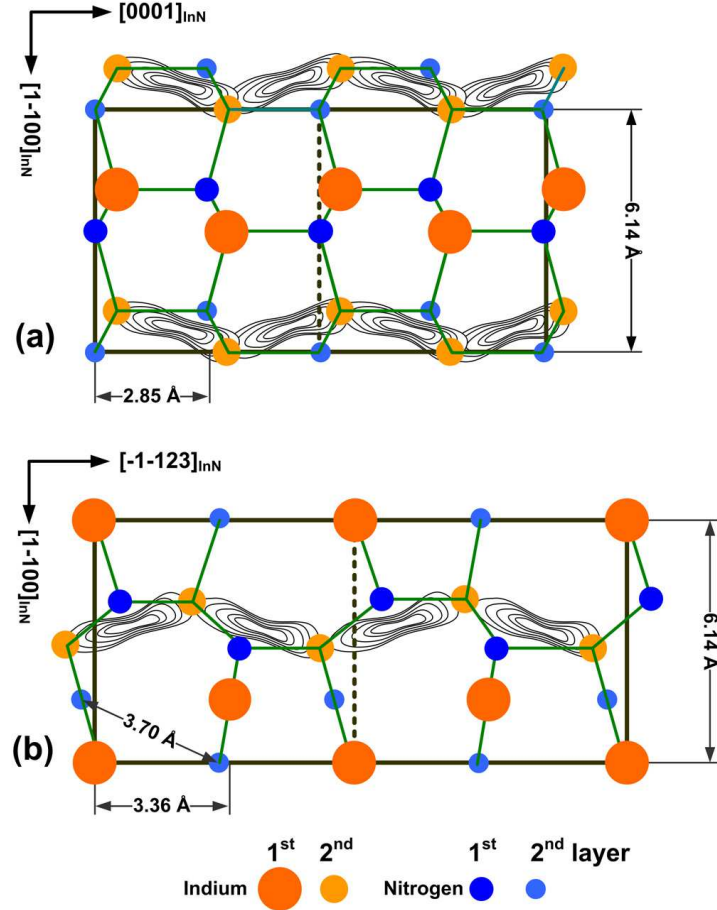


**Figure 7.10:** Unit cells ( $1 \times 2$ ) of (a) the relaxed nonpolar  $a$ -plane  $(11\bar{2}0)$  InN surface and (b) the relaxed semipolar  $(11\bar{2}2)$  InN surface. The contours indicate the pathway of indium adatom diffusions on these surfaces.

temperatures corresponding to the increase of RMS roughness and the decrease of crystallinity of the InN layers.

The  $(11\bar{2}2)$  InN layers replicated the undulations and the arrowhead morphology of the  $(11\bar{2}2)$  GaN templates. The formation of an undulation on the semipolar  $(11\bar{2}2)$  GaN templates grown on  $m$ -plane sapphire might be caused by anisotropic diffusion lengths of Ga-atoms along the  $[1\bar{1}00]_{\text{GaN}}$  and the  $[\bar{1}\bar{1}23]_{\text{GaN}}$  directions [169], and in-plane residual strain. Although the morphology of the  $(11\bar{2}2)$  InN layers was similar to the  $(11\bar{2}2)$  GaN templates, much higher undulation periods were found for the  $(11\bar{2}2)$  InN layers compared to the  $(11\bar{2}2)$  GaN templates [169], showing that the morphology of the InN layers is not only replicated the GaN surface.

### 7.3. Surface morphology and surface diffusion

---

As mentioned in Section 6.2.2, for the nonpolar  $a$ -plane ( $11\bar{2}0$ ),  $m$ -plane ( $1\bar{1}00$ ) GaN [120] and InN [121] surfaces, DFT calculations of the adatom kinetics of Ga-/In-atoms showed a strong dependence on specific geometry and stoichiometry of these surfaces due to (i) the different bonding properties of the weak metallic Ga-Ga/In-In bonds and the strong Ga-N/In-N bonds, and (ii) the distance that separates two neighboring adsorption sites along the  $[0001]$  direction and the perpendicular direction [120, 121]. For the  $m$ -plane GaN/InN surfaces, the diffusion barriers of Ga-/In-atoms are much higher along the  $[0001]_{\text{GaN/InN}}$  direction than along the  $[11\bar{2}0]_{\text{GaN/InN}}$  direction ( $\sim 4$  times larger for GaN and  $\sim 22$  times larger for InN along the  $[0001]_{\text{GaN/InN}}$  direction) [120, 121]. In contrast to the  $m$ -plane surface, the DFT calculations of Ga-/In-adatom kinetics (under metal-rich conditions) on the  $a$ -plane GaN/InN surfaces showed a smaller difference in the diffusion barriers of 0.31 eV/0.41 eV along the Ga-N/In-N dimer chains and the perpendicular direction [120, 121]. The surface diffusion barrier along the  $[0001]_{\text{GaN/InN}}$  directions of 0.32 eV/0.24 eV is smaller than along the  $[1\bar{1}00]_{\text{GaN/InN}}$  directions of 0.63 eV/0.65 eV [120, 121].

Furthermore, the distances separating two neighboring N-surface atoms on the  $a$ -plane GaN/InN surfaces along the  $[0001]$  and the  $[1\bar{1}00]$  directions are  $3.23 \text{ \AA}/3.01 \text{ \AA}$  and  $5.52 \text{ \AA}/6.14 \text{ \AA}$ , respectively (Fig. 7.10(a)). The used lattice parameters are  $a = 3.545 \text{ \AA}$  and  $c = 5.703 \text{ \AA}$  for InN, and  $a = 3.189 \text{ \AA}$  and  $c = 5.189 \text{ \AA}$  for GaN [29]. The smaller diffusion barriers on the  $a$ -plane GaN/InN surfaces result in faster lateral growth rates (due to a longer diffusion length) along the  $[0001]_{\text{GaN,InN}}$  directions than along the  $[1\bar{1}00]_{\text{GaN,InN}}$  directions. Figure 7.10(a) illustrates the diffusion pathways of Ga-/In-atoms on the  $a$ -plane GaN/InN surfaces as a zigzag jump (contour lines) between two adjacent Ga-N/In-N dimer chains.

In the case of the semipolar ( $11\bar{2}2$ ) InN surface, the adatom diffusion barrier of In-atoms is still unknown. However, the adatom diffusion barriers of Ga-atoms on the semipolar ( $11\bar{2}2$ ) GaN surface were estimated from the undulation periods to be  $\sim 0.8 \text{ eV}$  along the  $[\bar{1}\bar{1}23]_{\text{GaN}}$  direction and  $\sim 1.3 \text{ eV}$  along the  $[1\bar{1}00]_{\text{GaN}}$  direction [169]. Since the ( $11\bar{2}2$ ) InN layers replicated the surface morphology of the ( $11\bar{2}2$ ) GaN templates, the surface diffusion barriers of In-atoms on the ( $11\bar{2}2$ )<sub>InN</sub> surface should show a similar trend. Furthermore, the semipolar ( $11\bar{2}2$ ) GaN/InN surfaces are similar to the  $a$ -plane surface, but tilted by  $\sim 32^\circ$  (Figs. 2.4 and 7.10). A similar trend for Ga-/In-diffusion pathways on these semipolar surfaces is expected, i.e., a zigzag jump of Ga-/In-atoms

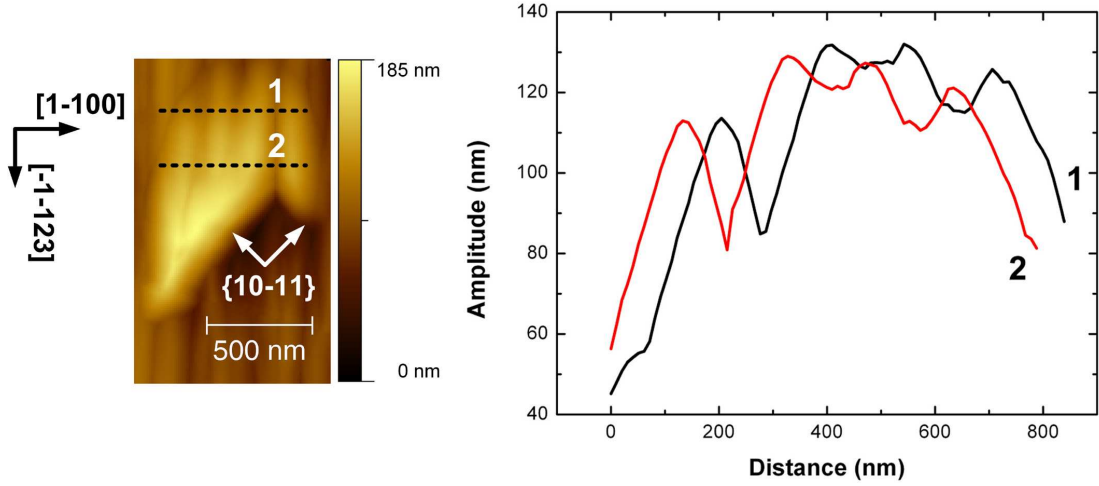


**Figure 7.11:** An island of the  $(11\bar{2}2)$  InN layer grown at  $560^\circ\text{C}$  with the horizontal size of  $0.7\ \mu\text{m}$  and the vertical size of  $1.5\ \mu\text{m}$ . The island exhibits undulation along the  $[\bar{1}\bar{1}00]_{\text{InN}}$  direction with a period of  $(168 \pm 12)$  nm, and an amplitude of  $(130 \pm 10)$  nm. The opening angle of the “V”-facets, terminating the islands, is  $\sim(100-110)^\circ$ , corresponding to the  $\{10\bar{1}1\}$  InN facets.

on the surfaces as illustrated in Fig. 7.10(b). The distances between the two neighboring atop N-surface atoms on the  $(11\bar{2}2)$  GaN/InN surfaces under metal-rich conditions are about  $3.40\ \text{\AA}/3.70\ \text{\AA}$  along the  $[\bar{1}\bar{1}23]$  direction and about  $5.52\ \text{\AA}/6.14\ \text{\AA}$  along the  $[1\bar{1}00]$  direction as shown in Fig. 7.10(b). These relative distances are similar to those of the  $a$ -plane GaN/InN surfaces. This increases the diffusion lengths of Ga-/In-atoms along the  $[\bar{1}\bar{1}23]_{\text{GaN, InN}}$  directions on the  $(11\bar{2}2)$  GaN/InN surfaces compared to those along the  $[1\bar{1}00]_{\text{GaN, InN}}$  directions, leading to a 2D-like growth along the  $[\bar{1}\bar{1}23]_{\text{GaN, InN}}$  directions and a 3D-like growth along the  $[1\bar{1}00]_{\text{GaN, InN}}$  directions compared to the  $(10\bar{1}\bar{3})$  InN layers (see Chapter 6). From the AFM images we assume a much faster lateral growth rate along the  $[\bar{1}\bar{1}23]_{\text{GaN, InN}}$  directions than that along the  $[1\bar{1}00]_{\text{GaN, InN}}$  directions to form the undulation (Fig. 7.8). Overall, the undulations of the  $(11\bar{2}2)$  InN surface not only replicate the typical morphology of the  $(11\bar{2}2)$  GaN templates but also are caused by the anisotropic diffusion of In-atoms on the  $(11\bar{2}2)$  InN surface.

The amplitude and period of the undulations on the  $(11\bar{2}2)$  InN surface increased with increasing growth temperatures (Fig. 7.9). This can be expanded by an increased diffusion length along the  $[\bar{1}\bar{1}23]_{\text{InN}}$  with increasing growth temperatures, which may result in faster growth rates in both directions.

Additionally, in the  $(11\bar{2}2)$  InN sample grown at  $560^\circ\text{C}$  islands with different sizes

(the horizontal sizes of 300 - 700 nm, and the vertical sizes of 600 - 1500 nm) are present, as shown in Fig. 7.11. These islands corresponds to be semipolar  $(11\bar{2}2)$  InN structures as well (Fig. 7.4(b)). The islands were terminated by  $c$ -plane facets or by “V”-facets. The opening angle of the “V”-facets, terminating the islands, is  $\sim(100-110)^\circ$ , thus the facets seem to be the  $\{10\bar{1}1\}$  InN facets. In the case of  $c$ -plane InN layers, the “V”-facets would contribute to hexagonal pits (Fig. 5.15). The islands on the  $(11\bar{2}2)$  InN surface also exhibit undulation with a period of  $(168 \pm 12)$  nm, and an amplitude of  $(130 \pm 10)$  nm, since they were grown on undulated structures. The growth of those islands might be caused by the recrystallization of In-atoms aggregating during the InN growth at the surface or at the border between two adjacent undulated structures, which may cause defects at the surface and alter the surface diffusions. On the other hand, the occurrence of these islands may somehow replicate islands that exist on some of the  $(11\bar{2}2)$  GaN templates. The shape of the islands, i.e., the arrowhead-like features confirm the anisotropic surface diffusion of In-atoms on the  $(11\bar{2}2)$  InN surface that occurs at the beginning of growth.

## 7.4 Defects and micro-structure

Cross-sectional transmission electron microscopy (TEM, measured by Francesco Ivaldi at Institute of Physics, Polish Academy of Sciences) was used to investigate structural defects of the InN layers using a JEOL 2000EX microscope equipped with a LaB6 electron gun operating at 200 kV. The  $(11\bar{2}2)$  InN layers grown at  $540^\circ\text{C}$  -  $550^\circ\text{C}$  were analyzed for TEM measurements. Figure 7.12 shows TEM images of the  $(11\bar{2}2)$  InN layer grown at  $550^\circ\text{C}$  in the  $[1\bar{1}00]$  and the  $[\bar{1}\bar{1}23]$  zone axes. The InN layer thickness was determined of  $(80 \pm 10)$  nm, which is comparable to the *in-situ* SE simulations (Fig. 7.1). The TEM images acquired along the  $[\bar{1}\bar{1}23]$  direction reveal triangular formations at the surface with the  $[11\bar{2}2]$  growth direction (Fig. 7.12(a)). The angles of the top triangular formations were estimated about  $(23 \pm 2)^\circ$ , and in good agreement with the undulations shown in Fig. 7.9. The peak to valley distances of the undulations vary between 60 - 110 nm and correlate with the distances measured by AFM (Figs. 7.8 and 7.9).

Due to the large lattice mismatch, non- and semi-polar III-nitride layers commonly have very high defect densities such as stacking faults (basal plane and prismatic stack-

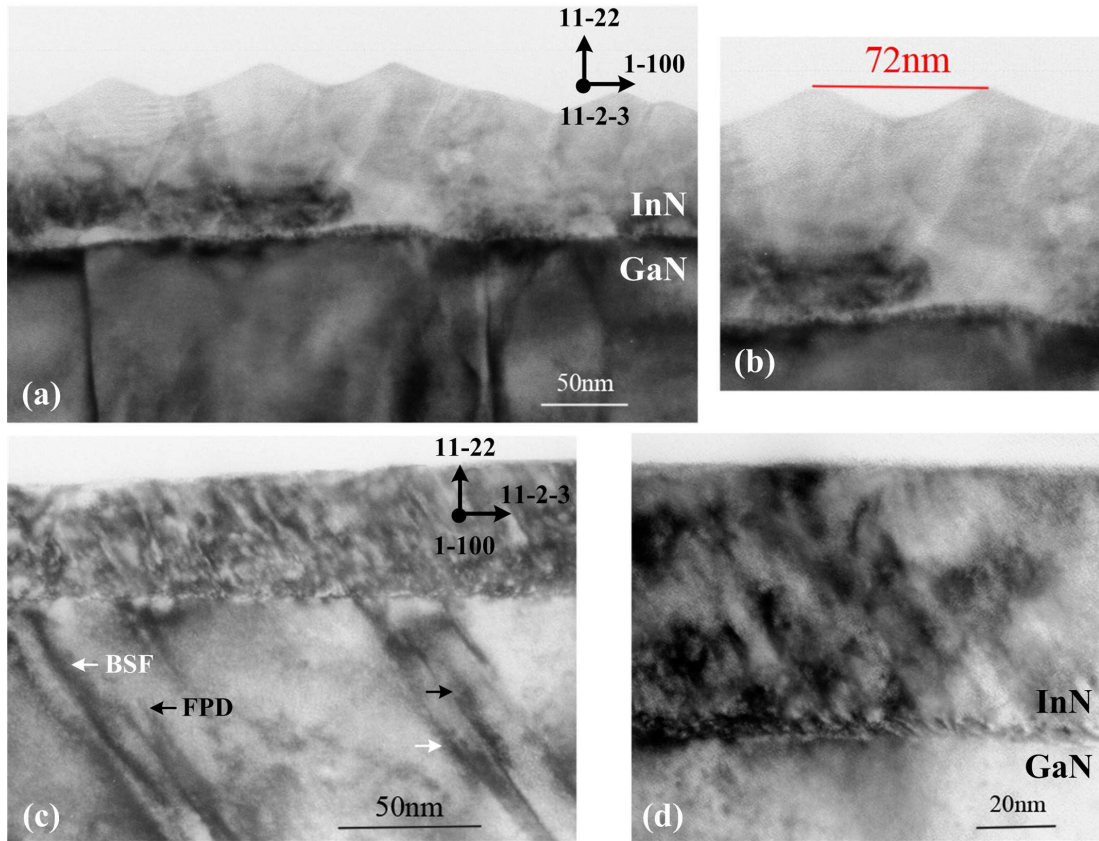


**Figure 7.12:** (a) and (b) TEM images of the  $(11\bar{2}2)$  InN layer grown at  $550^\circ\text{C}$  acquired in the  $[11\bar{2}3]$  zone axis. Triangular shaped formations can be distinguished at the surface. (c) and (d) TEM images acquired in the  $[1\bar{1}00]$  zone axis. The basal-plane stacking faults (BSFs, white arrows) and Frank-Shockley partial dislocations (FPDs, black arrows) in the  $(11\bar{2}2)$  GaN buffer layer can be observed in both axes. The TEM images were measured by Francesco Ivaldi at IFPAN, Poland.

ing faults) and dislocations (threading and partial dislocations) [135–139, 166, 173, 174]. In fact, the BSFs are present in the  $(11\bar{2}2)$  GaN buffer layers shown in the TEM images acquired for both axes (Figs. 7.12(a) and 7.12(c)). Frank-Shockley partial dislocations (FPDs) are also present in the  $(11\bar{2}2)$  GaN buffer layers as termination points of the stacking faults along the GaN basal planes. However, no defects could be observed in the  $(11\bar{2}2)$  InN layers. From the TEM images acquired in the  $[1\bar{1}00]$  zone axis (Fig. 7.12(c)), the GaN/InN interface reveals a high density of misfit dislocations due to the high lattice mismatch between  $(11\bar{2}2)$  InN and  $(11\bar{2}2)$  GaN, corresponding to the relaxation observed in asymmetric RSM  $(\bar{2}133)$  (Fig. 7.5(b)). Apparently, the presence of the BSFs in the  $(11\bar{2}2)$  GaN buffer layers does not affect the  $(11\bar{2}2)$  InN layers quality,

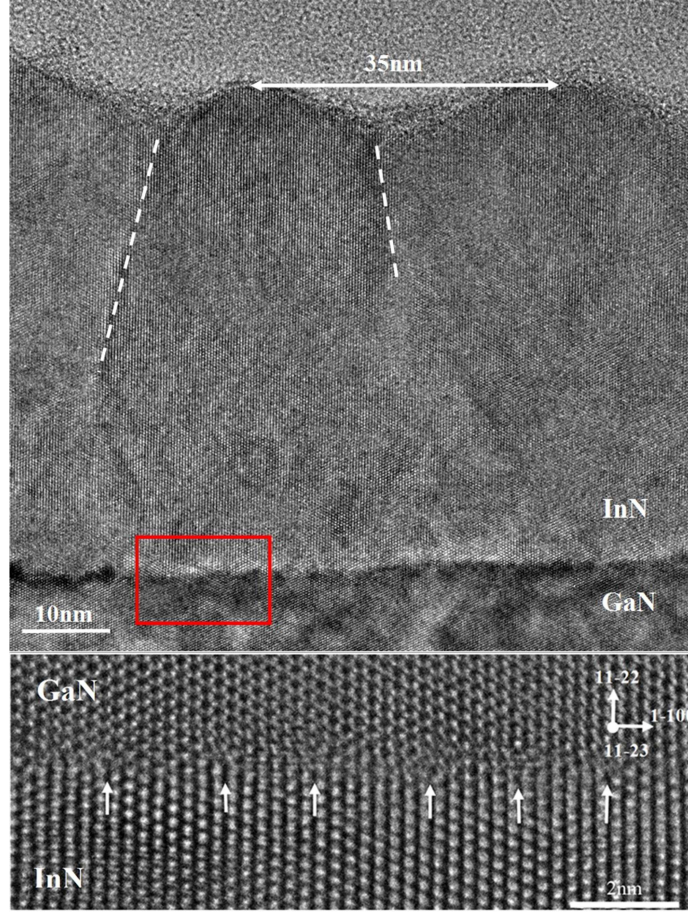


**Figure 7.13:** HR-TEM images of the  $(11\bar{2}2)$  InN sample grown at  $540^\circ\text{C}$  in the  $[\bar{1}\bar{1}23]$  zone axis. Coalescent borders between crystallites are marked with white dashed lines. The magnified area shows the fully relaxed InN/GaN interface and its  $60^\circ$  edge dislocations. The periodicity of the misfit dislocation is about 2 nm. The HRTEM images were measured by Francesco Ivaldi at IFPAN, Poland.

since all the observed faults were terminated at the FPDs or at the GaN/InN interface due to formation of the misfit dislocations.

The InN/GaN hetero-interfaces were further examined by high resolution TEM (HR-TEM) to investigate misfit dislocations at the interfaces. Figure 7.13 shows HR-TEM images of the  $(11\bar{2}2)$  InN layer grown at  $540^\circ\text{C}$  acquired in the  $[\bar{1}\bar{1}23]$  zone axis in bright field imaging mode. The bottom part of the InN layer reveals the presence of the misfit dislocations along the whole GaN/InN interface (Fig. 7.13), similar to  $c$ -plane InN quantum dots on  $c$ -plane GaN template [175]. The misfit dislocations could be determined to be perfect  $60^\circ$  edge dislocations with a Burger vector of type  $\mathbf{b} = \frac{1}{3a}\langle 11\bar{2}0 \rangle$

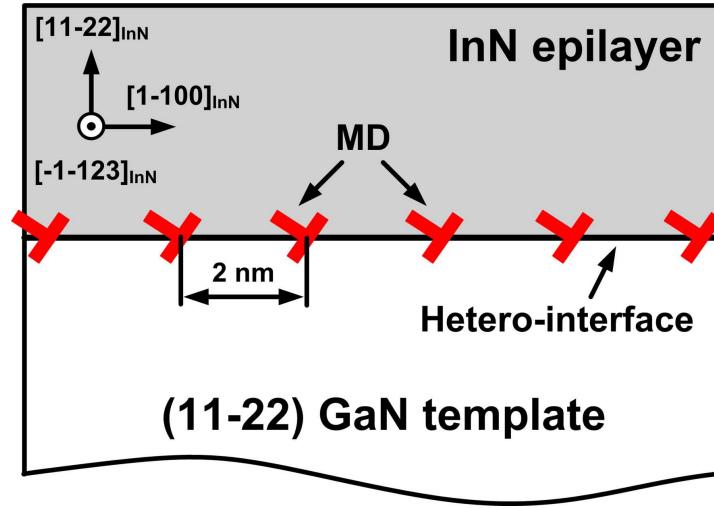


**Figure 7.14:** Schematics of misfit dislocations (MDs) in semipolar (11 $\bar{2}2$ ) InN epilayer grown on (11 $\bar{2}2$ ) GaN template. The misfit dislocations are spaced along the InN/GaN hetero-interface with 2 nm distance (8-9 lattice planes) between each other.

gliding on the (0001) InN basal plane along the  $[1\bar{1}00]_{\text{InN}}$  direction. Similar finding was found for (11 $\bar{2}2$ ) (Al,In)GaN [139, 164, 165]. The misfit dislocations are evenly spaced along the hetero-interface with 2 nm distance (8-9 lattice planes) between each other.

The presence of the misfit dislocations along the whole hetero-interface of the (11 $\bar{2}2$ ) InN/GaN layers observed here are common for hetero-grown semi-/non-polar III-nitride layers due to the lattice mismatches between the layers and substrates [136, 137, 139]. The misfit dislocations along the hetero-interfaces of non- and semi-polar III-nitride layers was contributed to the strain relaxation of the layers [138, 139, 166]. The misfit dislocations might also terminate or generate dislocations into the layers [136], and cause an epitaxial tilt angle of hetero-grown semi-/non-polar layers with respect to substrates [136–138]. Figure 7.14 shows the schematics of misfit dislocations in semipolar (11 $\bar{2}2$ ) InN epilayer grown on (11 $\bar{2}2$ ) GaN template. For the (11 $\bar{2}2$ ) InN layers, the relaxation state of the layers with the periodicity of the misfit dislocations was calculated by the geometric phase analysis of the layers, showing a  $\pm(1.5-2.0)\%$  of confidence on the strain values. The presence of the misfit dislocations resulted in not only the full relaxation but also in the lattice tilts of the (11 $\bar{2}2$ ) InN layers, as found in the RSM (Fig. 7.5).

The TEM images confirmed that 3D InN crystallites are formed on the GaN templates in the first stages of the growth process due to the Volmer-Weber growth. With

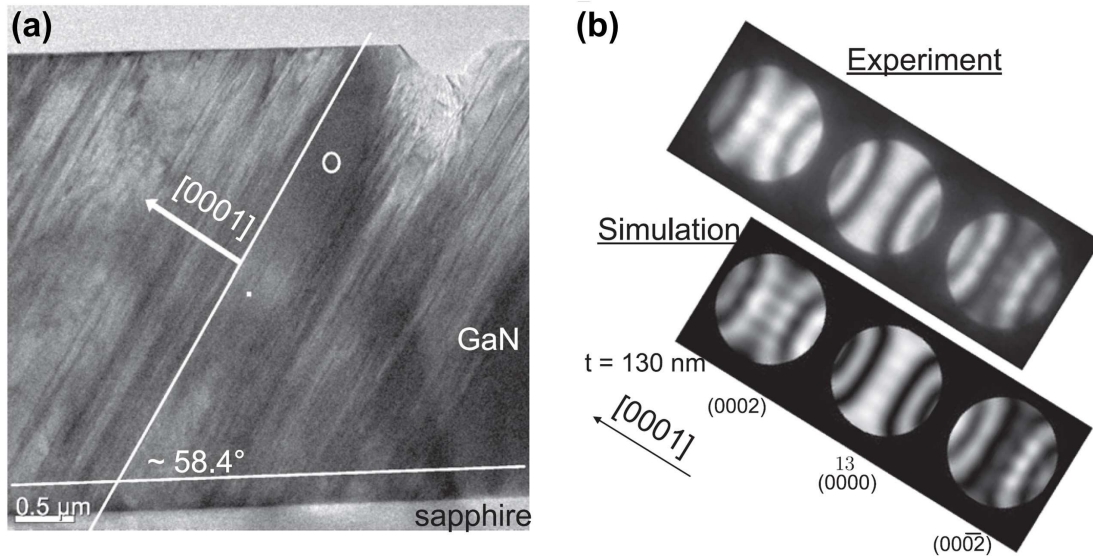


**Figure 7.15:** (a) TEM cross sectional image taken in the  $[1\bar{1}00]$  zone-axis in bright field imaging mode of a  $(11\bar{2}2)$  GaN template. The arrow denotes the direction of the  $[0001]_{\text{GaN}}$  direction. (b) Experimental and simulated CBED patterns in the  $[1\bar{1}00]$  zone-axis. Only a central section of the experimental CBED pattern at the  $[1\bar{1}00]$  zone-axis is depicted. By comparison with the simulated CBED pattern, the  $(11\bar{2}2)$  GaN layer was determined to have Ga-polarity [161].

increasing growth time, the crystallites enlarge, afterwards they coalesce with each other. The merging interfaces between the crystallites were observed in Fig. 7.13. However, no dislocations were observed at the coalescence sites (Fig. 7.13). Instead of it, a mono-crystalline layer was observed at the coalesced sites of two crystallites.

## 7.5 Polarity

The polarity of the  $(11\bar{2}2)$  GaN templates was determined using TEM measurement by convergent beam electron diffraction (CBED, measured by Jae Bum Park at Technical University of Berlin), which indicated that the  $(11\bar{2}2)$  GaN templates have Ga-polarity (Fig. 7.15 of Ref. 161). The grown  $(11\bar{2}2)$  InN layers are not thick enough for the CBED. However, all the grown  $(11\bar{2}2)$  InN layers on the  $(11\bar{2}2)$  GaN templates are expected to reproduce the group-III (Ga) polarity of the templates, therefore have the In-polarity, similar to the In-polar (0001) InN layers grown on the Ga-polar (0001) GaN templates.

X-ray photoelectron spectroscopic (XPS, measured by Daria Skuridina at Technical University of Berlin) measurements were used to determine the polarity of the semipolar

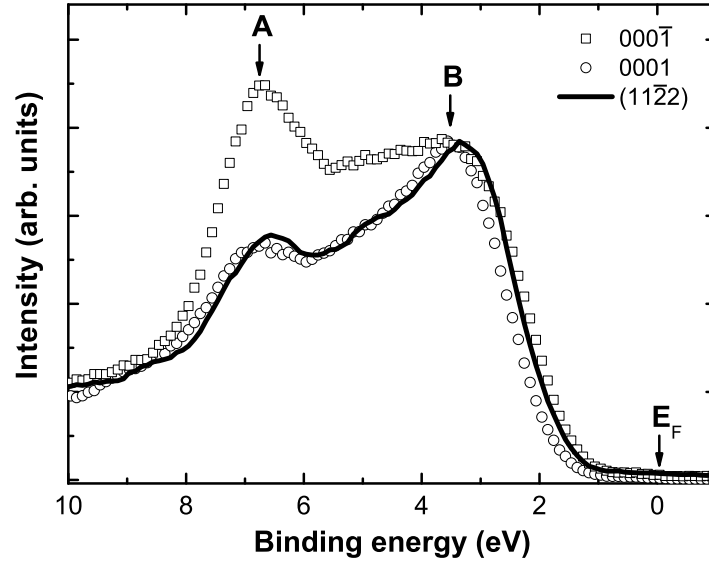


**Figure 7.16:** Valence band (VB) spectrum of a semipolar  $(11\bar{2}2)$  InN grown at  $560^\circ\text{C}$  (solid line) recorded along the  $[0001]_{\text{InN}}$  direction at an emission angle of  $\sim 58^\circ$  with respect to the surface normal. The XPS VB spectra of ( $\square$ ) the N-polar  $c$ -plane InN grown directly on  $c$ -plane sapphire, and ( $\circ$ ) the In-polar  $c$ -plane InN grown on Ga-polar  $c$ -plane GaN template were measured at normal emission. The spectra were normalized according to identical peak B intensity. The VB spectra were measured by Daria Skuridina at Technical University of Berlin.

$(11\bar{2}2)$  InN layers by comparing the peak heights in valence band (VB) spectra of InN (binding energy range of 0-10 eV, Section 5.1). The  $(11\bar{2}2)$  InN layers were rotated by  $\sim 58^\circ$  with respect to the analyzer to obtain emission along the  $[0001]_{\text{InN}}$  direction (Fig. 7.4(b)) and to achieve in-plane wave vector  $k_{\parallel[0001]} = 0$ . The VB spectrum of the oxidized  $(11\bar{2}2)$  InN layer grown at  $560^\circ\text{C}$  is shown in Fig. 7.16. The XPS spectrum consists of two distinct maxima at lower (peak B) and higher (peak A) binding energies (as discussed in Section 5.1).

In Fig. 7.16, the peak B dominates for the  $(11\bar{2}2)$  surface at  $\sim 58^\circ$  and the XPS VB spectrum of the  $(11\bar{2}2)$  InN layer is very similar to the spectrum of the In-polar  $c$ -plane InN layer on the Ga-polar  $c$ -plane GaN template (Fig. 5.8). Thus the  $(11\bar{2}2)$  InN layers have In-polarity, matching the Ga-polar orientation of the  $(11\bar{2}2)$  GaN templates.

## 7.6 Chapter summary

The MOVPE growth and characterizations of  $(11\bar{2}2)$  InN layers on  $(11\bar{2}2)$  GaN templates on  $m$ -plane sapphire were investigated. The surface morphology and crystal orientation of the grown InN layers were similar to those of the  $(11\bar{2}2)$  GaN templates. The surface morphology of the  $(11\bar{2}2)$  InN layers and the  $(11\bar{2}2)$  GaN templates showed an undulation along the  $[\bar{1}100]_{\text{InN, GaN}}$  directions attributed to anisotropic adatom diffusion. The polarity of the  $(11\bar{2}2)$  InN layers was determined to be In-polar by valence band photoelectron spectroscopy, matching to the Ga-polar  $(11\bar{2}2)$  GaN surface of the template. Compared to  $c$ -plane InN, the growth rate of  $(11\bar{2}2)$  InN was 3-4 times lower. The  $(11\bar{2}2)$  InN layers were relaxed and the relaxation occurred at the InN/GaN interface by formation of misfit dislocations with a spacing of 2 nm. The presence of the misfit dislocations not only caused a tilt of the  $(11\bar{2}2)$  InN layers to the GaN templates and the  $(11\bar{2}2)$  GaN templates to  $m$ -plane sapphire but also blocked the penetration of basal stacking faults in the  $(11\bar{2}2)$  GaN templates into the  $(11\bar{2}2)$  InN layers.

## Chapter 8

# Polar (0001) $\text{In}_x\text{Ga}_{1-x}\text{N}$

A large solid phase miscibility gap of ternary  $\text{In}_x\text{Ga}_{1-x}\text{N}$  alloys, which comes from the large difference in interatomic spacing (11%) between  $\text{InN}$  and  $\text{GaN}$  [45], is attributed to cause the difficulties of  $\text{InGaN}$  growth. Furthermore,  $\text{In}_x\text{Ga}_{1-x}\text{N}$  layers grown on  $c$ -plane  $\text{GaN}$  templates show rough surface morphology due to the strain relaxation and the subsequent three-dimensional (3D) growth. In contrast to  $c$ -plane  $\text{InN}$  and  $\text{GaN}$ , the growth parameters of  $\text{In}_x\text{Ga}_{1-x}\text{N}$  directly on sapphire are not well-known and must be improved.

This chapter will deal with the growth of  $\text{In}_x\text{Ga}_{1-x}\text{N}$  layers directly on  $c$ -plane sapphire. The effects of growth parameters (V/III ratio, growth time, and growth temperature) on quality of the  $\text{In}_x\text{Ga}_{1-x}\text{N}$  layers were systematically investigated.

In Chapter 5, the growth of  $\text{InN}$  layers directly on different oriented sapphire substrates has been investigated. The growth parameters of  $\text{In}_x\text{Ga}_{1-x}\text{N}$  directly on  $c$ -plane sapphire were mostly based on the growth parameters of  $\text{InN}$  on  $c$ -plane sapphire. Figure 8.1 shows the growth diagram of  $\text{In}_x\text{Ga}_{1-x}\text{N}$  grown directly on  $c$ -plane sapphire by a two-step growth mode, including the nitridation process and  $\text{In}_x\text{Ga}_{1-x}\text{N}$  epitaxy. Similar to the  $\text{InN}$  layers grown on  $c$ -plane sapphire substrate, the substrate was thermally cleaned (under  $\text{H}_2$ ) at  $1050^\circ\text{C}$  for 10 min. Subsequently, the substrate was nitridated (using 3l/min  $\text{NH}_3$  under  $\text{N}_2$  carrier gas with a flow rate of 3l/min) at the same temperature for 2 min. After the nitridation process, the sample was cooled to  $600\text{--}750^\circ\text{C}$  to grow  $\text{In}_x\text{Ga}_{1-x}\text{N}$  layer under  $\text{N}_2$ . All the growth steps were performed at a reactor pressure of 100 mbar.

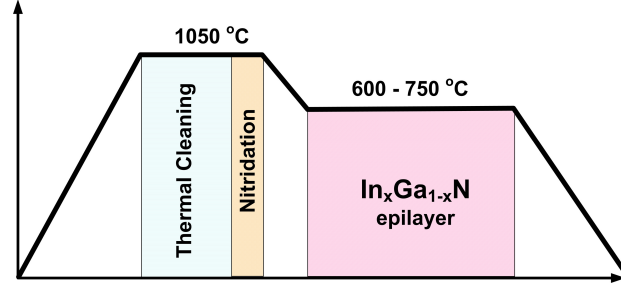


**Figure 8.1:** Growth diagram of  $\text{In}_x\text{Ga}_{1-x}\text{N}$  directly on  $c$ -plane sapphire. The thermal cleaning and the nitridation processes were performed at 1050°C, while the  $\text{In}_x\text{Ga}_{1-x}\text{N}$  epitaxy was performed at 600-750°C.

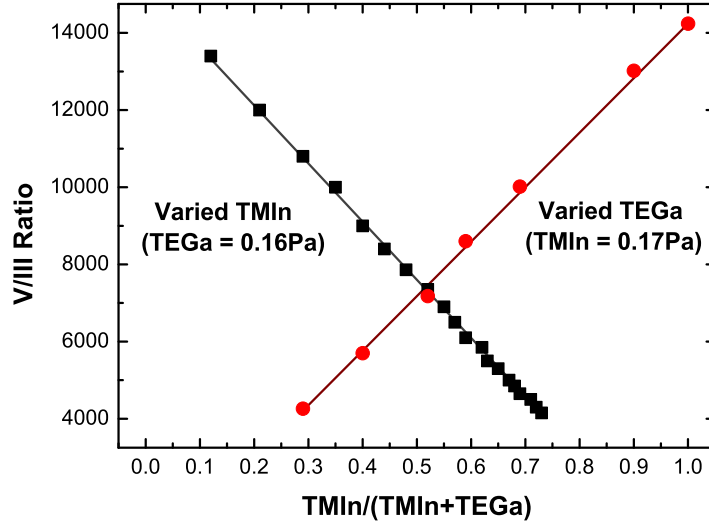


**Figure 8.2:**  $\text{TMIn}/(\text{TMIn}+\text{TEGa})$  ratio plotted as a function of  $\text{V}/\text{III}$  ratio. ( $\square$ ) Varied  $\text{TMIn}$  partial pressure while keeping  $\text{TEGa} = 0.16\text{Pa}$ . ( $\circ$ ) Varied  $\text{TEGa}$  partial pressure while keeping  $\text{TMIn} = 0.17\text{Pa}$ .

Trimethyl-indium ( $\text{TMIn}$ ), triethyl-gallium ( $\text{TEGa}$ ), and  $\text{NH}_3$  were used as In-, Ga-, and N-source, respectively. During the  $\text{In}_x\text{Ga}_{1-x}\text{N}$  epitaxy,  $\text{NH}_3$  flow rate was kept constant at 1 l/min (partial pressure of  $\sim 2500\text{Pa}$ ). Figure 8.2 shows  $\text{TMIn}/(\text{TMIn}+\text{TEGa})$  ratio *vs.*  $\text{V}/\text{III}$  ratio (4000-14000). Varied  $\text{TMIn}$  or  $\text{TEGa}$  flow rate while keeping the other one constant was used to achieve different In-contents of the  $\text{In}_x\text{Ga}_{1-x}\text{N}$  layers (Fig. 8.2).

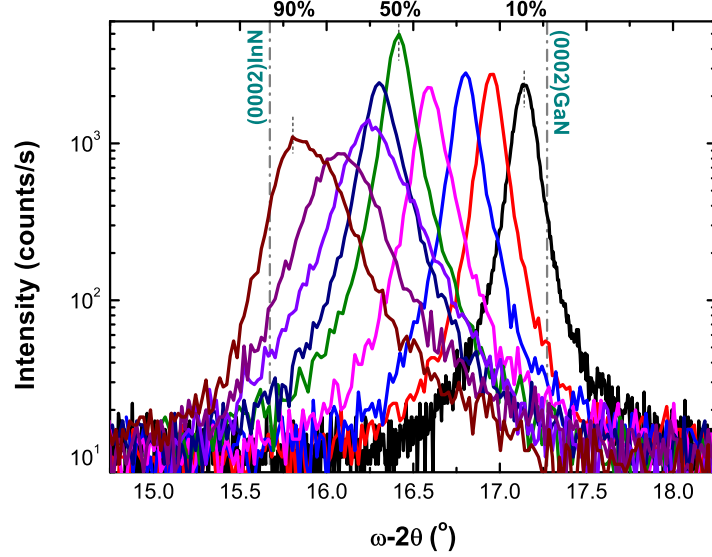


**Figure 8.3:** XRD  $\omega$ - $2\theta$  scans of the  $\text{In}_x\text{Ga}_{1-x}\text{N}$  layers grown on  $c$ -plane sapphire at  $600^\circ\text{C}$ . The XRD spectra were normalized to the (0006) reflection of sapphire at  $\sim 20.84^\circ$ .

## 8.1 Effect of group-III input flow rate

### 8.1.1 Crystalline properties

In-contents of the  $\text{In}_x\text{Ga}_{1-x}\text{N}$  layers were determined based on the Vegards law [187, 188] from the peak angles of (0002) reflections obtained by X-ray diffraction (XRD)  $\omega$ - $2\theta$  scans. Figure 8.3 shows the (0002) reflections of the  $\text{In}_x\text{Ga}_{1-x}\text{N}$  layers on  $c$ -plane sapphire at  $600^\circ\text{C}$  with different  $\text{TMIn}/(\text{TMIn}+\text{TEGa})$  ratios. The peak positions of the XRD  $\omega$ - $2\theta$  spectra continuously shift between the lower angles with respect to the (0002) InN position and the higher angles with respect to the (0002) GaN position. All the XRD spectra show symmetrical curves with single peaks, indicating the growth of pure  $\text{In}_x\text{Ga}_{1-x}\text{N}$  layers without any phase separations, as well as no metallic indium (i.e., the (101) reflection of metallic indium at  $\sim 16.47^\circ$ ). Peak broadening can be attributed to the layer thickness (see discussion in page 113). The  $\text{In}_x\text{Ga}_{1-x}\text{N}$  layers were assumed to be fully relaxed, which gave the In-contents in Fig. 8.4. The In-contents of the  $\text{In}_x\text{Ga}_{1-x}\text{N}$  layers were found to cover the whole range ( $0 < x < 1$ ). This implies that the theoretically predicted miscibility gap of  $\text{In}_x\text{Ga}_{1-x}\text{N}$  was not observed [45].

Similar to the growth of InN, the growth of  $\text{In}_x\text{Ga}_{1-x}\text{N}$  is also sensitive to indium and gallium input flow rates (or TMIn and TEGa partial pressures). To inves-

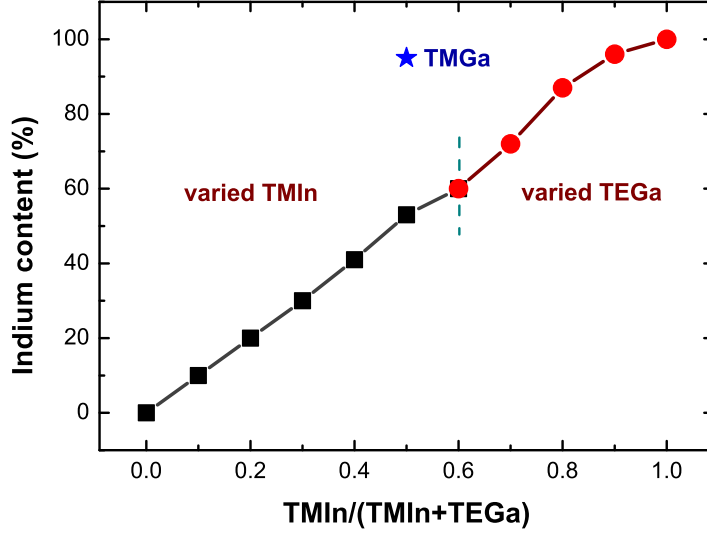


**Figure 8.4:** In-contents plotted as a function of  $\text{TMIn}/(\text{TMIn}+\text{TEGa})$  ratio, showing linear behaviors even with different TMIn ( $\square$ ) or TEGa ( $\circ$ ) input flow rates. Instead of using TEGa, TMGa ( $\star$ ) was used for a reference, giving  $\sim 95\%$  In-content compared to  $\sim 50\%$  In-content of  $\text{InGa}_x\text{N}$  when using TEGa with the same  $\text{TMIn}/(\text{TMIn}+\text{TEGa})$  ratio.

to investigate the effect of indium input flow rate on the growth of  $\text{In}_x\text{Ga}_{1-x}\text{N}$ , the TEGa partial pressure was kept constant at 0.16 Pa, the TMIn partial pressure was varied between 0.0-0.25 Pa, corresponding to  $\text{TMIn}/(\text{TMIn}+\text{TEGa}) = 0.1-0.6$  (V/III ratios shown in Fig 8.2). By this,  $\text{In}_x\text{Ga}_{1-x}\text{N}$  layers with In-content of 10-60% can be grown (Fig. 8.4). The  $\text{TMIn}/(\text{TMIn}+\text{TEGa})$  ratios showed a linear behavior with respect to In-contents (Fig. 8.4). However, when the TMIn partial pressure was larger than 0.25 Pa ( $\text{TMIn}/(\text{TMIn}+\text{TEGa}) = 0.6$ ), only metallic indium was found. The very rich In-condition prevented the growth of  $\text{In}_x\text{Ga}_{1-x}\text{N}$ .

In order to obtain more In-rich  $\text{In}_x\text{Ga}_{1-x}\text{N}$ , the TMIn partial pressure was kept at 0.17 Pa while the TEGa partial pressure was varied between 0.0-0.17 Pa, corresponding to  $\text{TMIn}/(\text{TMIn}+\text{TEGa}) = 0.5-1.0$  (V/III ratios shown in Fig 8.2). By this,  $\text{In}_x\text{Ga}_{1-x}\text{N}$  layers with In-content range of 60-90% can be grown (Fig. 8.4). Overall, by varying the  $\text{TMIn}/(\text{TMIn}+\text{TEGa})$  ratio, the whole range of In-contents of  $\text{In}_x\text{Ga}_{1-x}\text{N}$  can be grown directly on *c*-plane sapphire. This indicates that growth temperature is sufficiently low to avoid indium desorption.

Instead of using TEGa, TMGa precursor was used as Ga-source for a single sample. By choosing a  $\text{TMIn}/(\text{TMIn}+\text{TMGa}) = 0.5$ , about  $\sim 95\%$  In-content  $\text{InGa}_x\text{N}$  was grown

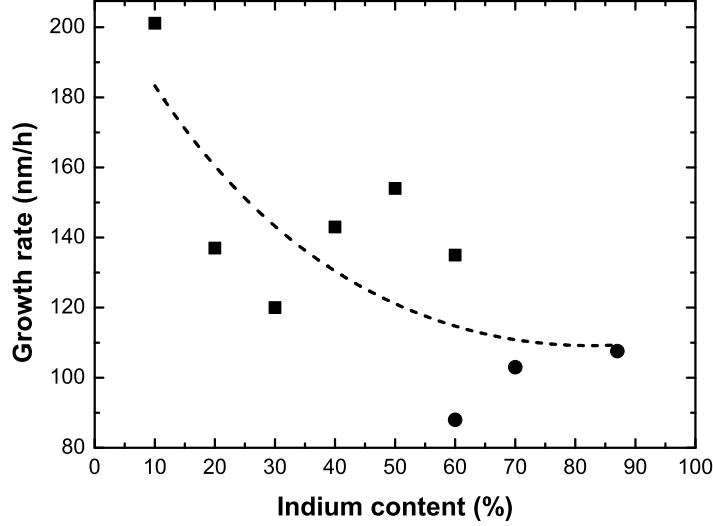


**Figure 8.5:** Growth rates of the  $\text{In}_x\text{Ga}_{1-x}\text{N}$  layers grown on  $c$ -plane sapphire at  $600^\circ\text{C}$  for 60 min as a function of In-contents in two different cases: varied TMIn ( $\square$ ) and varied TEGa ( $\circ$ ).

compared to  $\sim 50\%$  In-content InGaN when using TEGa with the same  $\text{TMIn}/(\text{TMIn}+\text{TEGa})$  ratio (Fig. 8.4). This is caused by the lower decomposition of TMGa at  $600^\circ\text{C}$  compared to TEGa [63].

The thickness of the  $\text{In}_x\text{Ga}_{1-x}\text{N}$  layers on  $c$ -plane sapphire were estimated using Scherrer equation [191], with an assumption that the  $\text{In}_x\text{Ga}_{1-x}\text{N}$  layers were fully relaxed and perfectly crystallinity. The Scherrer equation can be described below:

$$d_{\text{InGaN}} = \frac{0.94 \times \lambda}{FWHM_{\omega-2\theta} \times \cos(2\theta)}, \quad (8.1)$$

where  $d_{\text{InGaN}}$  is the estimated layer thickness,  $\lambda$  is the X-ray wavelength ( $\lambda = 1.54056 \text{ \AA}$ ), and  $FWHM_{\omega-2\theta}$  is the FWHM value of XRD  $\omega-2\theta$  scan in radian.

Based on the thickness estimations, the growth rates of the  $\text{In}_x\text{Ga}_{1-x}\text{N}$  layers were determined and plotted as a function of In-contents (Fig. 8.5). The growth rate decreases with increasing In-contents of the  $\text{In}_x\text{Ga}_{1-x}\text{N}$  layers. It is very interesting to note that for the varied TMIn case, the growth rates of the  $\text{In}_x\text{Ga}_{1-x}\text{N}$  layers were two times higher than those for the varied TEGa case.

Figure 8.6 shows full-width at half maximum (FWHM) of (0002) X-ray rocking curves (XRC) of the  $\text{In}_x\text{Ga}_{1-x}\text{N}$  layers grown on  $c$ -plane sapphire. The FWHM values showed a parabolic curve with different In-contents with a broad maximum peak at

## 8.1. Effect of group-III input flow rate

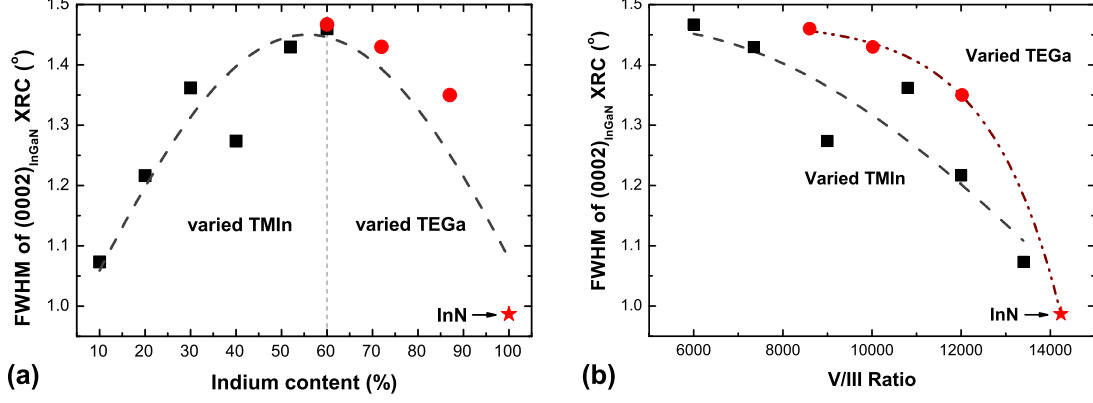


**Figure 8.6:** FWHM values of (0002) X-ray rocking curves (XRC) of the  $\text{In}_x\text{Ga}_{1-x}\text{N}$  layers on *c*-plane sapphire at 600°C as functions of (a) In-contents (or  $\text{TMIn}/(\text{TMIn}+\text{TEGa})$  ratio) and of (b) V/III ratio.

around 60% In-content ( $\text{TMIn}/(\text{TMIn}+\text{TEGa}) = 0.6$ ). Additionally, due to the different V/III ratios of the varied TMIn and the varied TEGa cases (Fig. 8.2), the FWHM values were also plotted as a function of the V/III ratios (Fig. 8.6(b)). The FWHM values were between 1.0-1.5° and decreased with increasing the V/III ratios for both the varied TMIn and the varied TEGa cases (Fig. 8.6(b)).

For  $\text{In}_x\text{Ga}_{1-x}\text{N}$  system, the Helmholtz free energy of mixing ( $\Delta F_{mix}$ ) can be described as [189, 190]:

$$\Delta F_{mix}(x, T) = \Delta U_{mix}(x, T) - T\Delta S_{mix}(x, T), \quad (8.2)$$

where  $\Delta S_{mix}$  is the entropy of mixing,  $\Delta U_{mix}$  is the enthalpy of mixing,  $T$  is the absolute temperature. For an ideal case, the enthalpy of mixing can be considered to be zero, and hence:

$$\begin{aligned} \Delta U_{mix}(x, T) &= 0 \\ \Delta F_{mix}(x, T) &= -T\Delta S_{mix}(x, T). \end{aligned} \quad (8.3)$$

The lower crystallinity of a layer, the greater its entropy and free energy [189]. At the same temperature and pressure, the free energy of mixing for wurtzite  $\text{In}_x\text{Ga}_{1-x}\text{N}$  vs. In-content shows the same shape as of the FWHM curve [190]. Thus, one should expect that larger FWHM value of the  $\text{In}_x\text{Ga}_{1-x}\text{N}$  XRC relates to larger value of the

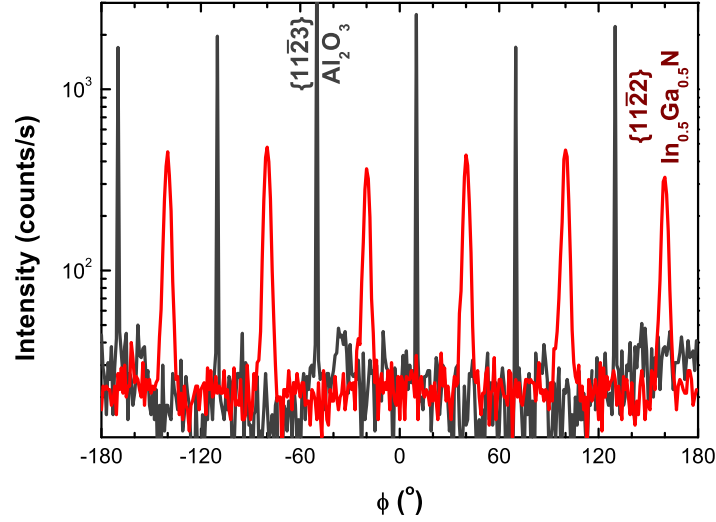


**Figure 8.7:** XRD  $\phi$ -scans performed in skew-symmetry of the  $\{11\bar{2}2\}$  reflection of an  $\text{In}_{0.5}\text{Ga}_{0.5}\text{N}$  layer with respect to the  $\{11\bar{2}3\}$  reflection of  $c$ -plane sapphire.

free energy of mixing. On the other hand, the changes of the FWHM values might also relate to the changes of layer thickness. In fact, the thickness of the  $\text{In}_x\text{Ga}_{1-x}\text{N}$  layers (for 1 h growth) reduces with increasing In-contents (Fig. 8.5), this might result in the increase of the FWHM values.

To determine the epitaxial in-plane relationship between the  $c$ -plane  $\text{In}_x\text{Ga}_{1-x}\text{N}$  layers and  $c$ -plane sapphire, XRD  $\phi$ -scans were performed in skew-symmetry. Figure 8.7 shows the skew-symmetric  $\phi$ -scan of the  $\{11\bar{2}2\}$  reflection of an  $\text{In}_{0.5}\text{Ga}_{0.5}\text{N}$  layer with respect to the  $\{11\bar{2}3\}$  reflection of  $c$ -plane sapphire. Similar to  $c$ -plane InN on  $c$ -plane sapphire (Fig. 4.9), the skew-symmetric  $\phi$ -scan of the  $\{11\bar{2}2\}$  reflection of the  $c$ -plane  $\text{In}_{0.5}\text{Ga}_{0.5}\text{N}$  layer also shows six sharp peaks of the  $c$ -plane  $\text{In}_{0.5}\text{Ga}_{0.5}\text{N}$  at exactly  $60^\circ$  intervals (and exactly  $30^\circ$  periods with respect to the  $\{11\bar{2}3\}$  reflection of  $c$ -plane sapphire). This not only confirms that the  $\text{In}_{0.5}\text{Ga}_{0.5}\text{N}$  layer exhibits a single-domain wurtzite structure with six-fold symmetry, but also confirms that the sapphire nitridation at  $1050^\circ\text{C}$  also works for the growth of the  $\text{In}_x\text{Ga}_{1-x}\text{N}$  layers. The in-plane relationship of the  $\text{In}_x\text{Ga}_{1-x}\text{N}$  layers with respect to  $c$ -plane sapphire is  $[\bar{1}100]_{\text{In}_x\text{Ga}_{1-x}\text{N}} \parallel [11\bar{2}0]_{\text{sapphire}}$  and  $[0001]_{\text{In}_x\text{Ga}_{1-x}\text{N}} \parallel [0001]_{\text{sapphire}}$ .

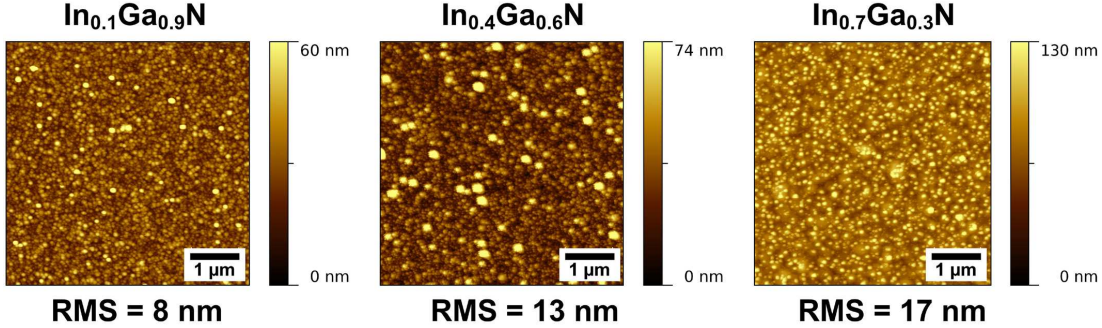


**Figure 8.8:**  $5\ \mu\text{m}\times 5\ \mu\text{m}$  AFM images of the  $\text{In}_x\text{Ga}_{1-x}\text{N}$  layers with different In-contents grown on  $c$ -plane sapphire at  $600^\circ\text{C}$  for 60 min. Thicknesses of the layers were shown in Fig. 8.5.

### 8.1.2 Surface morphology and polarity determination

The surface morphology of the  $\text{In}_x\text{Ga}_{1-x}\text{N}$  layers was examined by  $5\ \mu\text{m}\times 5\ \mu\text{m}$  AFM images in contact mode (Fig. 8.8). All the layers showed a grainy surface morphology with root-mean square (RMS) roughness varied from 7 nm to 23 nm (Fig. 8.9). The RMS roughness increased with increasing In-contents independent of absolute TMin and TEGa flows (Fig. 8.9). The increase of RMS value with increasing In-contents is attributed to the increase of lattice mismatch in the  $a$ -axis between  $\text{In}_x\text{Ga}_{1-x}\text{N}$  and sapphire.

Similar to  $c$ -plane InN (Section 5.3), the polarity of the  $\text{In}_x\text{Ga}_{1-x}\text{N}$  layers was determined by KOH wet-etching (20% KOH at  $30^\circ\text{C}$ ). Figure 8.10 shows the surface morphology ( $2\ \mu\text{m}\times 2\ \mu\text{m}$ ) of an  $\text{In}_{0.7}\text{Ga}_{0.3}\text{N}$  layer before KOH wet-etching, after 20 min and 60 min KOH wet-etching. Before the KOH wet-etching process (Fig. 8.10(a)), the surface morphology of the layer showed a grainy morphology (RMS = 14.5 nm) consisting of many islands. However, no phase separation was observed for this layer (Fig. 8.3). After 20 min KOH wet-etching (Fig. 8.10(b)), the layer showed a rougher surface morphology (RMS = 18 nm) than before the KOH wet-etching. A higher density and a larger size of islands were also observed, many small islands were at the grainy boundaries, indicating the layer was etched. After 60 min KOH wet-etching, the layer consisted of only islands (RMS = 20 nm). The density and the size of islands continuously increased when the etching time increased, indicating the layer was etched deeper. After 60 min KOH wet-etching (Fig. 8.10(c)), the layer was almost etched away. Similar KOH wet-etching results were observed for N-polar InN layer grown on  $c$ -plane sapphire,

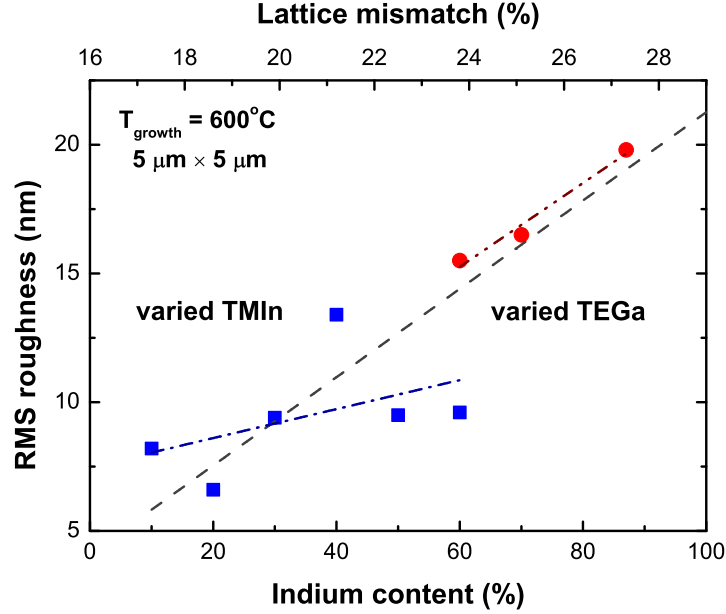


**Figure 8.9:** RMS roughness values ( $5 \mu\text{m} \times 5 \mu\text{m}$ ) of the  $\text{In}_x\text{Ga}_{1-x}\text{N}$  layers plotted as functions of In-contents and lattice mismatches in the  $a$ -axis between  $\text{In}_x\text{Ga}_{1-x}\text{N}$  and  $c$ -plane sapphire with the varied TMIn ( $\square$ ) and varied TEGa ( $\circ$ ) cases. Lines are the linear fits.

which was nitridated at  $1050^\circ\text{C}$  for 2 min [170]. Since the  $\text{In}_x\text{Ga}_{1-x}\text{N}$  layers were grown on  $c$ -plane sapphire by using the same nitridation parameters (Fig. 8.1), we concluded that the  $\text{In}_x\text{Ga}_{1-x}\text{N}$  layers also have the N-polarity.

## 8.2 Evolution of $\text{In}_{0.5}\text{Ga}_{0.5}\text{N}$ morphology and crystallinity

A series of layers was prepared in which the  $\text{In}_x\text{Ga}_{1-x}\text{N}$  growth was stopped after periods of time ranging from 2 min to 60 min. TMIn/(TMIn+TEGa) ratio was 0.5, and the growth temperature was  $600^\circ\text{C}$ . In XRD  $\omega$ - $2\theta$  scans, all the  $\text{In}_x\text{Ga}_{1-x}\text{N}$  layers show the same peak position, which corresponds to 50% In-content of InGaN (Fig. 8.11). The symmetrical broadening of the XRD spectra indicates pure  $\text{In}_{0.5}\text{Ga}_{0.5}\text{N}$  layers were grown. No metallic indium was observed. The intensities of the (0002)  $\text{In}_x\text{Ga}_{1-x}\text{N}$  reflections drastically increase with increasing growth time, indicating the increase of layer thickness. Using the Scherrer equation (Eqn. 8.1 and Ref. 191), estimated thicknesses of 2-130 nm were found for the layers grown for 2-60 min, respectively (Fig. 8.12). However, the layer thickness does not show a linear behavior with the growth temperatures,

## 8.2. Evolution of $\text{In}_{0.5}\text{Ga}_{0.5}\text{N}$ morphology and crystallinity

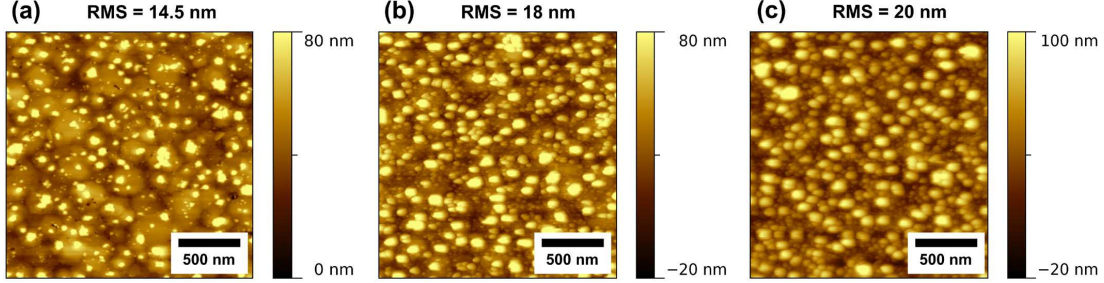


**Figure 8.10:**  $2\ \mu\text{m}\times 2\ \mu\text{m}$  AFM images of an  $\text{In}_{0.7}\text{Ga}_{0.3}\text{N}$  layer ( $\approx 120\ \text{nm}$ ) (a) before KOH wet-etching, and after (b) 20 min and (c) 60 min KOH wet-etching.

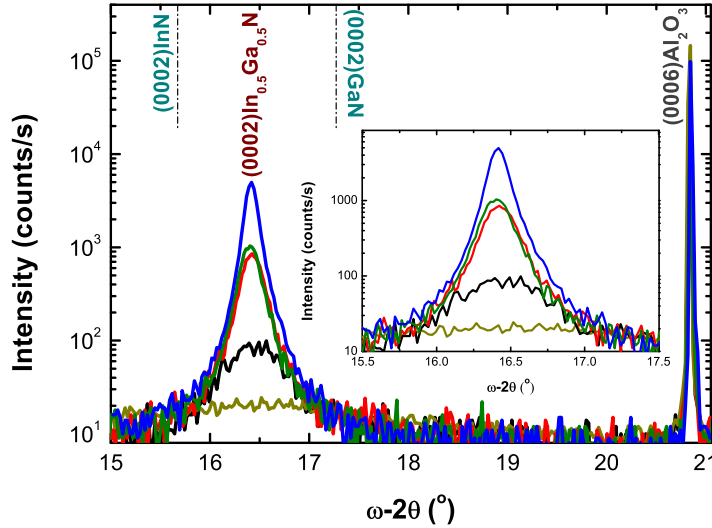


**Figure 8.11:** XRD  $\omega$ - $2\theta$  scans of the  $\text{In}_x\text{Ga}_{1-x}\text{N}$  layers on  $c$ -plane sapphire grown at  $600^\circ\text{C}$  for 2-60 min at a  $\text{TMIIn}/(\text{TMIIn}+\text{TEGa})$  ratio of 0.5. The *inset* shows the enlargements of the XRD spectra at the (0002)  $\text{In}_x\text{Ga}_{1-x}\text{N}$  reflections.

indicating a change in growth mode.

Figure 8.13 shows AFM images ( $2\ \mu\text{m}\times 2\ \mu\text{m}$ ) of the  $\text{In}_x\text{Ga}_{1-x}\text{N}$  layers grown on  $c$ -plane sapphire for different time. For 2 min growth time, the  $\text{In}_x\text{Ga}_{1-x}\text{N}$  layer showed a very high density of small islands similar to the morphology of nitridated layer (Fig. 4.5), indicating that time was just enough for  $\text{In}_x\text{Ga}_{1-x}\text{N}$  to nucleate on the nitridated layer. After 5 min, some uncoated areas can be seen. When growth time was about 13 min, the islands started to coalesce explaining the reduction of the vertical growth rate (Fig. 8.12). The 3D structures indicate the  $\text{In}_x\text{Ga}_{1-x}\text{N}$  layers are due to the Volmer-Weber growth mode (VW). However, the surface morphology of the  $\text{In}_x\text{Ga}_{1-x}\text{N}$  layers still showed 3D structures even after 60 min. The VW growth mode was also observed

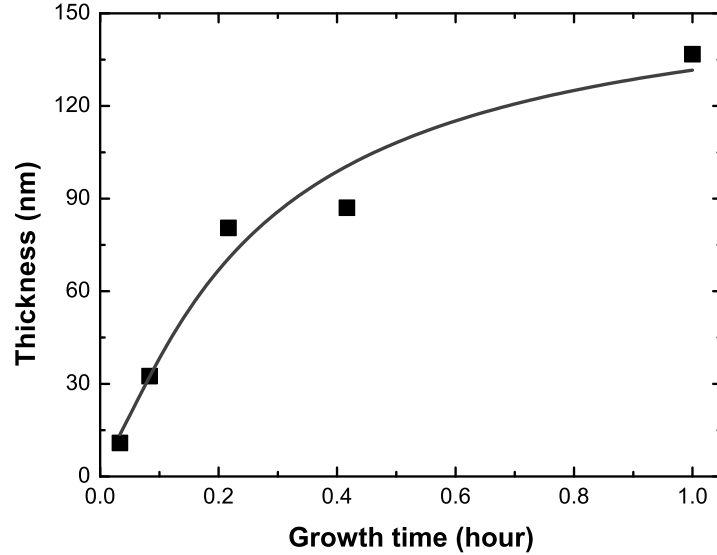


**Figure 8.12:** Estimated thickness of the  $\text{In}_x\text{Ga}_{1-x}\text{N}$  layers grown on *c*-plane sapphire at  $600^\circ\text{C}$  for 2-60 min.

for In-polar InN on Ga-polar GaN [170]. For the N-polar  $\text{In}_x\text{Ga}_{1-x}\text{N}$  layers on *c*-plane sapphire, the VW growth mode is attributed to the large lattice mismatch of  $\text{In}_x\text{Ga}_{1-x}\text{N}$  compared to GaN.

### 8.3 Effect of growth temperature

For III-nitride epitaxy, growth temperature is one of the most important parameters since it affects not only the decomposition rate of group III precursors but also the surface diffusion and desorption. It is known that at high temperature ( $T > 600^\circ\text{C}$ ), In-content decreases drastically due to desorption of In-atoms [192, 193]. To investigate the effects of temperature on the In-content of InGaN, the  $\text{TMIIn}/(\text{TMIIn} + \text{TEGa})$  ratio was kept at 0.5, which corresponded to about 50% In-content InGaN layer grown at  $600^\circ\text{C}$  (Figs. 8.3 and 8.4). The growth of  $\text{In}_x\text{Ga}_{1-x}\text{N}$  layers was performed at different temperatures from  $600^\circ\text{C}$  to  $750^\circ\text{C}$ . Figure 8.14(a) shows the XRD  $\omega - 2\theta$  scans of the  $\text{In}_x\text{Ga}_{1-x}\text{N}$  layers on *c*-plane sapphire, indicating a decrease of In-contents with increasing growth temperatures. Figure 8.14(b) shows the exponential decrease of In-contents caused by the increase of the desorption rate of In-atoms, e.g., when growth temperature was  $750^\circ\text{C}$ , only 8% In-content InGaN layer was grown. Again, no phase

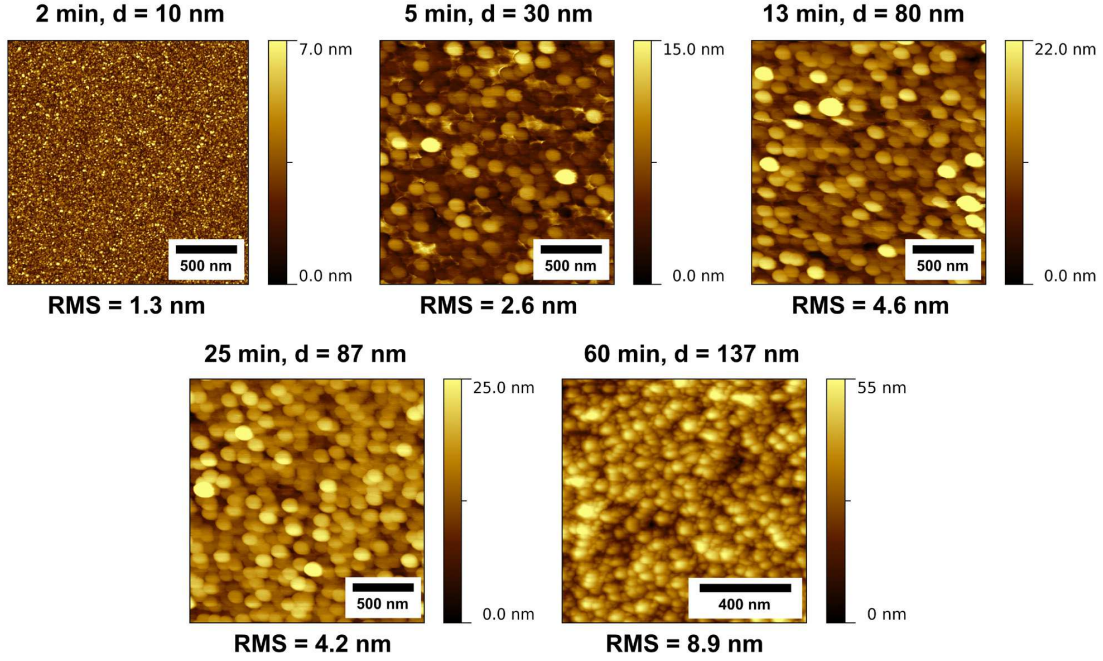


**Figure 8.13:** Evolution of surface morphology ( $2\mu\text{m}\times 2\mu\text{m}$  AFM images) of the  $\text{In}_x\text{Ga}_{1-x}\text{N}$  layers grown on  $c$ -plane sapphire at  $600^\circ\text{C}$  for different times.

separations and no metallic indium were found for all cases (Fig. 8.14(a)).

The FWHM values of (0002) XRC were about  $1.0$ - $1.4^\circ$  for the  $\text{In}_x\text{Ga}_{1-x}\text{N}$  layers on  $c$ -plane sapphire at different temperatures (Fig. 8.14(b)). The FWHM values decreased with increasing growth temperatures, indicating the higher crystallinity of the lower In-content  $\text{In}_x\text{Ga}_{1-x}\text{N}$  layers. The trend of the FWHM values might be related to the mixing free energy of  $\text{In}_x\text{Ga}_{1-x}\text{N}$ , where the mixing free energy decreases with increasing temperatures [190]. This trend of the FWHM values in these cases is similar to the results shown in Fig. 8.6(a).

The  $\text{In}_x\text{Ga}_{1-x}\text{N}$  layers grown on  $c$ -plane sapphire at different temperatures showed a surface morphology with RMS roughness value ( $5\mu\text{m}\times 5\mu\text{m}$ ) about 4-7 nm (Fig. 8.15). However, in contrast to the  $\text{In}_x\text{Ga}_{1-x}\text{N}$  layers grown on  $c$ -plane sapphire at  $600^\circ\text{C}$  (Fig. 8.9), the RMS roughness value of the  $\text{In}_x\text{Ga}_{1-x}\text{N}$  layers grown at different temperatures slightly increases with increasing growth temperatures, i.e., 5.0 nm and 6.5 nm for the layers grown at  $700^\circ\text{C}$  and  $750^\circ\text{C}$ , respectively (Fig. 8.15). Since the  $\text{In}_x\text{Ga}_{1-x}\text{N}$  growth was due to the VW growth mode, the diffusion length along the perpendicular growth direction ( $[000\bar{1}]_{\text{InGa}_x\text{N}}$ ) should be longer than that along the parallel growth

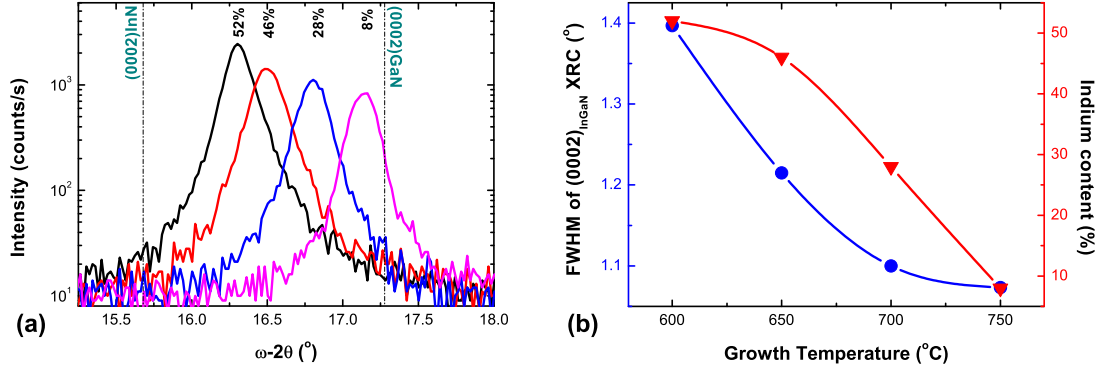


**Figure 8.14:** (a) XRD  $\omega-2\theta$  scans of the  $\text{In}_x\text{Ga}_{1-x}\text{N}$  layers on *c*-plane sapphire grown at different temperatures for 30 min. The XRD spectra were normalized to the (0006) reflection of sapphire at  $\sim 20.84^\circ$ . A TMIIn/(TMIIn+TEGa) ratio of 0.5 was chosen. (b) FWHM values of (0002) X-ray rocking curves (XRC, ○) of the  $\text{In}_x\text{Ga}_{1-x}\text{N}$  layers on *c*-plane sapphire at different temperatures as functions of In-contents (▽) and growth temperatures.

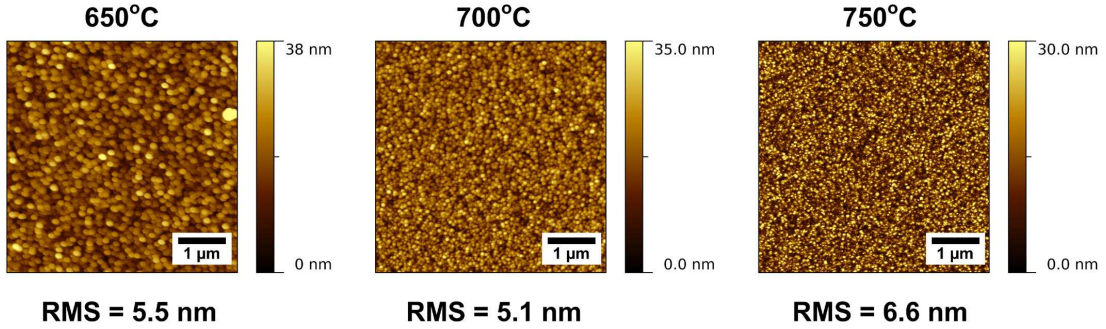


**Figure 8.15:**  $5\ \mu\text{m} \times 5\ \mu\text{m}$  AFM images ( $\approx 50\text{--}70\ \text{nm}$ ) of the  $\text{In}_x\text{Ga}_{1-x}\text{N}$  layers on *c*-plane sapphire grown at  $650^\circ\text{C}$  (46% In-content),  $700^\circ\text{C}$  (28% In-content), and  $750^\circ\text{C}$  (8% In-content).

direction ( $[1\bar{1}00]_{\text{InGa}_x\text{N}}$ ). The  $\text{In}_x\text{Ga}_{1-x}\text{N}$  growth might be more complex at higher growth temperatures due to the increased desorption rate of In-atoms, which affects the In-incorporation and surface morphology.

## 8.4 Chapter summary

The growth of the whole range of In-content of  $\text{In}_x\text{Ga}_{1-x}\text{N}$  layers directly on *c*-plane sapphire has been investigated. The  $\text{In}_x\text{Ga}_{1-x}\text{N}$  layers showed N-polarity due to the sapphire nitridation at  $1050^\circ\text{C}$  for 2 min, similar to N-polar InN.

Dependence of crystallinity and morphology on indium (TMIIn) and gallium (TEGa)

input flow rate, growth time and temperature were investigated. All  $\text{In}_x\text{Ga}_{1-x}\text{N}$  layers were found to be single phase in In-content and epitaxial relationship. Compared to  $\text{In}_x\text{Ga}_{1-x}\text{N}$  layers on *c*-plane GaN templates, improved homogeneity, surface morphology, as well as an increased range of In-content were realized. The surface morphology of the  $\text{In}_x\text{Ga}_{1-x}\text{N}$  layers showed 3D structures due to the Volmer-Weber growth mode, explaining the relatively rough surface.

# Summary

The presented work describes MOVPE growth and properties of InN layers with polar and semipolar surface orientations. The work focuses on two aspects of the growth: (1) the understanding the growth processes, the control polarity and orientations, and (2) the properties of the layers with different surface orientations.

Sapphire nitridation process (varied time and temperature) was studied for InN and  $\text{In}_x\text{Ga}_{1-x}\text{N}$  ( $0 < x < 1$ ) epitaxy grown directly on sapphire. The nitridation was critical to control polarity (i.e., (0001) polarity or  $(000\bar{1})$  polarity) and improve crystallinity and surface morphology. Sapphire nitridation at higher temperatures ( $\geq 800^\circ\text{C}$ ) not only enhances the crystallinity and surface morphology, but also produces an N-polar orientation of InN and InGaN layers on *c*-plane sapphire. N-polar *c*-plane InN layers on *c*-plane sapphire was grown at  $560^\circ\text{C}$  after sapphire nitridation at  $1050^\circ\text{C}$  for 2 min with good quality.

Polar *c*-plane (0001) InN layers with different polarities grown on *c*-plane sapphire (N-polar InN) and on *c*-plane GaN/sapphire templates (In-polar InN) showed different trends of layer quality with respect to growth temperature ( $520$  -  $560^\circ\text{C}$ ). N-polar InN layers showed a better crystallinity and smoother surface than In-polar InN layers at higher growth temperatures due to a two-dimensional (2D) growth mode, while In-polar InN layers exhibit a 3D growth mode.

Semipolar InN layers with  $(10\bar{1}\bar{3})$  and  $(11\bar{2}2)$  orientations were grown directly on nitridated *m*-plane  $(1\bar{1}00)$  sapphire and on  $(11\bar{2}2)$  GaN templates, respectively. Semipolar InN layers showed an anisotropic crystallinity and morphology, as well as anisotropic structural properties due to the typical growth orientations and the anisotropic adatom diffusion.  $(10\bar{1}\bar{3})$  InN layers showed 3D structures consisting of islands, while  $(11\bar{2}2)$  InN layers showed a planar surface morphology.

---

Finally, based on the growth parameters of InN, *c*-plane  $\text{In}_x\text{Ga}_{1-x}\text{N}$  layers with the entire range of In-content were grown directly on *c*-plane sapphire substrates nitridated at 1050°C for 2 min. The In-content of  $\text{In}_x\text{Ga}_{1-x}\text{N}$  was precisely controlled by varying gas ratio or by varying growth temperature (600 - 750°C).  $\text{In}_x\text{Ga}_{1-x}\text{N}$  layers showed a relative smooth morphology but were still due to the 3D growth mode.

# Zusammenfassung

Diese Arbeit beschreibt das MOVPE Wachstum und die Charakterisierung von InN Schichten mit polaren und semipolaren Oberflächenorientierungen. Zwei Aspekte des Wachstums werden dabei eingehender betrachtet: (1) das Verständnis des Wachstumsprozesses, sowie die Kontrolle der Polarität und Oberflächenorientierung; und (2) die Charakterisierung der epitaktischen Schichten mit verschiedenen Oberflächenorientierungen.

Sowohl für, epitaktisch auf Saphir abgeschiedenes, InN als auch für  $\text{In}_x\text{Ga}_{1-x}\text{N}$  ( $0 < x < 1$ ) wurde der Nitridierungsprozess von Saphir in Abhängigkeit von Zeit und Temperatur untersucht. Dabei erwies sich die Nitridation als wichtiger Faktor um nicht nur die Polarität (entweder (0001) oder (000 $\bar{1}$ )) festzulegen, sondern auch um die Kristallinität und Oberflächenmorphologie zu verbessern. So verbessert die Nitridation bei Temperaturen über 800°C sowohl die Oberflächenmorphologie als auch die Kristallinität. Gleichzeitig erzeugt die Nitridation eine N-polare Oberflächenorientierung bei InN und InGaN Schichten, die auf (0001) Saphir abgeschieden wurden. Stickstoffpolare (0001) InN Schichten von guter Qualität wurde bei 560°C abgeschieden, nachdem bei 1050°C für zwei Minuten nitridiert wurden.

N-polare (0001) InN Schichten, die auf nitridiertem Saphir und In-polare InN Schichten, die auf GaN/Saphir Templates bei 520°C-560°C abgeschieden wurden zeigen deutlich unterschiedliche Schichtqualitäten. N-polare InN Schichten haben eine bessere Kristallinität und glattere Oberflächen als In-polare InN Schichten. In-polare InN Schichten zeigen hingegen dreidimensionalem Wachstum.

Semipolare InN Schichten mit (10 $\bar{1}\bar{3}$ ) beziehungsweise (11 $\bar{2}\bar{2}$ ) Oberflächenorientierung wurden auf nitridiertem *m*-orientierten (1 $\bar{1}$ 00) Saphir und auf (11 $\bar{2}\bar{2}$ ) GaN Templates abgeschieden. Semipolare InN Schichten besitzen eine anisotrope Kristallinität und Morphologie, sowie anisotrope Strukturelle Eigenschaften. Diese sind typisch für die jeweiligen Wachstumsorientierten und die anisotrope Diffusionen der Adatom. Auf

---

( $10\bar{1}\bar{3}$ ) InN Schichten findet man dreidimensionale Inseln, während ( $11\bar{2}2$ ) InN Schichten eine planare Oberflächenmorphologie haben.

Basierend auf den Wachstumsparametern von InN Schichten wurden ( $0001$ )  $\text{In}_x\text{Ga}_{1-x}\text{N}$  Schichten im gesamten Zusammensetzungsbereich auf ( $0001$ ) Saphir Substraten abgeschieden. Diese Substraten wurden zuvor für zwei Minuten bei  $1050^\circ\text{C}$  Nitridierung. Durch die Variation der Partialdrücke der Precursor und durch Kontrolle der Wachstumstemperatur ( $600$ - $750^\circ\text{C}$ ) konnte der Indiumanteil in  $\text{In}_x\text{Ga}_{1-x}\text{N}$  Schichten genau festgelegt werden. Diese  $\text{In}_x\text{Ga}_{1-x}\text{N}$  Schichten haben eine verhältnismäßig glatte Oberflächenmorphologie, neigen aber dennoch zu dreidimensionalem Wachstum.

# Acknowledgments

I would like to express my thanks to all, who support and help me in this work. In particular I would like to thank:

Prof. Dr. Michael Kneissl and PD Dr. Markus Pristovsek for their opportunities in this project, as well as a lot of discussion and helpful comment. Without them, this work could not be succeeded, therefore I am very grateful to them.

Prof. Dr. Nicolas Grandjean at École Polytechnique Fédérale de Lausanne (EPFL, Switzerland), for his comments as a co-reviewer of this thesis.

Prof. Dr. Christ F. McConville at University of Warwick (UW, United Kingdom) for his kindly suggestions and discussions as my mentor within the Rainbow project.

Dipl.-Phys. Daria Skuridina for her permanent interest in InN, her supports for XPS and LEED results, as well as her help for thesis proofreading.

Dipl.-Phys. Simon Ploch and Dipl.-Phys. Martin Frentrup for their supporting GaN templates and many discussions.

Sergej Solopow for his supporting measurements during his Diploma work.

Dr. Tim Wernicke for a lot of discussion and helpful comment for my manuscripts and thesis.

Dipl.-Phys. Nils Kaufmann and Bsc. Eng. Denis Martin (EPFL, Switzerland), Ms. Sci. Albert Minj (UNIBO, Italy), Dr. Naresh Gunasekar (USTRA, Scotland), Dipl.-Phys. Egidijus Sakalauskas (TUIL, Germany), Dipl.-Phys. Francesco Ivaldi (IFPAN, Poland), and Dr. Arantxa Vilalta-Clemente (CIMAP, France) as well as all other members of the Rainbow project for their warmly welcomes during the Rainbow trainings and workshops.

Matthias Dreier for his very kindly helps and sharing many experiences about the

---

life in Germany.

Dipl.-Phys. Tim Kolbe and his wife, Susann Hemmel Kolbe, for their helps to get appointments for Germany VISA application.

All other members of the group of Prof. Dr. Kneissl for the motivating atmosphere, as well as for the pleasant and successful cooperation during my PhD.

And especially my family for their continuous supports and encouragements.

This work was financially supported by the EU-ITN RAINBOW project within the 7th Framework Program (FP7), under agreement no. PITN-GA-2008-213238.

### Bibliography

- [1] O. V. Losev, *Telegrafiya i Telefoniya bez Provodov* **44**, 485 (1927).
- [2] H. J. Round, “A Note on Carborundum”, *Electrical World* **19**, 309 (1907).
- [3] T. H. Maiman, *Nature* **187**, 493 (1960).
- [4] R. N. Hall, G. E. Fenner, J. D. Kingsley, T. J. Soltys, and R. O. Carlson, *Phys. Rev. Lett.* **9**, 366 (1962).
- [5] M. I. Nathan, W. Dumke, G. Burns, F. H. Dill Jr., and G. Lasher, *Appl. Phys. Lett.* **1**, 62 (1962).
- [6] N. Holonyak Jr. and S. F. Bevacqua, *Appl. Phys. Lett.* **1**, 82 (1962).
- [7] T. M. Quist, R. H. Rediker, R. J. Keyes, W. E. Krag, B. Lax, A. L. McWhorter, and H. J. Zeigler, *Appl. Phys. Lett.* **1**, 91 (1962).
- [8] Z. I. Alferov and R. F. Kazarinov, “Semiconductor laser with electric pumping”, Inventors Certificate 181737 [in Russian], Appli. 950840, (1963).
- [9] H. Kroemer, “Semiconductor laser with electric pumping”, U.S. Patent 3 309 553, (1967).
- [10] D. F. Welch, *IEEE J. Sel. Top. Quantum Electron.* **6**, 1470 (2000).
- [11] Z. I. Alferov, *IEEE J. Sel. Top. Quantum Electron.* **6**, 832 (2000).
- [12] D. F. Nelson, R. J. Collins, and W. Kaiser, *Phys. Today* **63** (1), 40 (2010).
- [13] S. Nakamura, T. Mukai, and M. Senoh, *Appl. Phys. Lett.* **64**, 1687 (1994).
- [14] T. L. Tansley and C. P. Foley, *Electron. Lett.* **20**, 1066 (1984).
- [15] T. L. Tansley and C. P. Foley, *J. Appl. Phys.* **59**, 3241 (1986).
- [16] V. Y. Davydov, A. A. Klochikhin, V. V. Emtsev, D. A. Kurdyukov, S. V. Ivanov, V. A. Vekshin, F. Bechstedt, J. Furthmüller, J. Aderhold, J. Graul, A. V. Mudryi, H. Harima, A. Hashimoto, A. Yamamoto, and E. E. Haller, *Phys. Stat. Solidi B* **234**, 787 (2002).
- [17] J. Wu, W. Walukiewicz, K. M. Yu, J. W. Ager, E. E. Haller, H. Lu, W. J. Schaff, Y. Saito, and Y. Nanishi, *Appl. Phys. Lett.* **80**, 3967 (2002).
- [18] G. Koblmüller, C. S. Gallinat, S. Bernardis, J. S. Speck, G. D. Chern, E. D. Readinger, H. Shen, and M. Wraback, *Appl. Phys. Lett.* **89**, 071902 (2006).
- [19] <http://www.osram-os.com/>
- [20] <http://www.soraa.com/>

## BIBLIOGRAPHY

---

- [21] J. W. Ager III, J. Wu, K. M. Yu, R. E. Jones, S. X. Li, W. Walukiewicz, E. E. Haller, H. Lu, and W. J. Schaff, <http://dx.doi.org/10.1117/12.561935> **5530**, 308 (2004).
- [22] A. Yamamoto, Md. R. Islam, T.-T. Kang, and A. Hashimoto, *Phys. Stat. Sol. C* **7**, 1309 (2010).
- [23] A. E. Romanov, T. J. Baker, S. Nakamura, and J. S. Speck, *J. Appl. Phys.* **100**, 023522 (2006).
- [24] J. Li, K. B. Nam, M. L. Nakarmi, J. Y. Lin, H. X. Jiang, P. Carrier, and S.-H. Wei, *Appl. Phys. Lett.* **83**, 5163 (2003).
- [25] A. Chakraborty, B. A. Haskell, S. Keller, J. S. Speck, S. P. DenBaars, S. Nakamura, and U. K. Mishra, *Appl. Phys. Lett.* **85**, 5143 (2004).
- [26] A. Chakraborty, T. J. Baker, B. A. Haskell, F. Wu, J. S. Speck, S. P. DenBaars, S. Nakamura, and U. K. Mishra, *Jpn. J. Appl. Phys.* **44**, L945, (2005).
- [27] H. Masui, S. Nakamura, S. P. DenBaars, U. K. Mishra, *IEEE Trans. Elec. Dev.* **57**, 88 (2009).
- [28] D. R. Askeland, P. P. Fulay, W. J. Wright “The Science and Engineering of Materials” 6<sup>th</sup> Ed., Cengage Learning, Stamford, USA (2010).
- [29] O. Madelung, “Semiconductors: data handbook”, 3<sup>rd</sup> Ed., Springer, Berlin, Heidelberg (2004).
- [30] E. T. Yu, X. Z. Dang, P. M. Asbeck, S. S. Lau, and G. J. Sullivan, *J. Vac. Sci. Technol. B* **17(4)**, 1742 (1999).
- [31] W. Qian, M. Skowronski, G. R. Rohrer, Chapter: “Structural defects and their relationship to nucleation of GaN thin films” in “III-Nitride, SiC, and Diamond Materials for Electronic Devices”. Eds. D. K. Gaskill, C. D. Brandt, and R. J. Nemanich, Mater. Res. Soc. Symp. Proceedings, Pittsburgh, PA., **423**, 475 (1996).
- [32] M. E Levinshhtēin, S. L. Rumyantsev, M. Shur, “Properties of Advanced Semiconductor Materials: GaN, AlN, InN, BN, SiC, SiGe”, John Wiley & Sons, Inc., New York, p. 49-66 (2001).
- [33] E. R. Dobrovinskaya, L. A. Lytvynov, and V. Pishchik, “Sapphire: Materials, Manufacturing, Application”, Springer, p. 109, (2009).
- [34] S. C. Jain, M. Willander, J. Narayan, and R. Van Overstraeten, *J. Appl. Phys.* **87**, 965 (2000).
- [35] S. N. Mohammad and H. Morkoc, *Prog. Quantum Electron.* **20**, 361 (1996).
- [36] M. Shur, B. Gelmont, and M. A. Khan, *J. Electron. Mater.* **25**, 777 (1996).

## BIBLIOGRAPHY

---

- [37] B. E. Foutz, S. K. O’Leary, M. S. Shur, and L. F. Eastman, *J. Appl. Phys.* **85**, 7727 (1999).
- [38] V. W. L. Chin, T. L. Tansley, and T. Osotchan, *J. Appl. Phys.* **75**, 7365 (1994).
- [39] C. H. Swartz, R. P. Tomkins, T. H. Myers, H. Lu, and W. J. Schaff, *Phys. Stat. Sol. C* **2**, 2250 (2005).
- [40] S. C. Binari and H. C. Dietrich, “GaN and Related Materials”, Gordon and Breach, New York, (1997).
- [41] K. Wongchotiquil, N. Chen, D. P. Zhang, X. Tang, and M. G. Spencer, *H12 Mater. Res. Soc. Symp. Proc.*, **395**, 279 (1996).
- [42] S. K. O’leary, B. E. Foutz, M. S. Shur, U. V. Bhapkar, and L. F. Eastman, *J. Appl. Phys.* **83**, 826 (1998).
- [43] S. K. O’Leary, B. E. Foutz, M. S. Shur, and L. F. Eastman, *Appl. Phys. Lett.* **88**, 152113 (2006).
- [44] R. Ascázubi, I. Wilke, K. Denniston, H. Lu, and W. J. Schaff, *Appl. Phys. Lett.* **84**, 4810 (2004).
- [45] I. Ho and G. B. Stringfellow, *Appl. Phys. Lett.* **69**, 2701 (1996).
- [46] I. Mahboob, T. D. Veal, L. F. J. Piper, C. F. McConville, H. Lu, W. J. Schaff, J. Furthmüller, and F. Bechstedt, *Phys. Rev. B.* **69**, 201307(R) (2004).
- [47] I. Mahboob, T. D. Veal, C. F. McConville, H. Lu, and W. J. Schaff, *Phys. Rev. Lett.* **92**, 036804 (2004).
- [48] J. M. Woodall, J. L. Freeouf, G. D. Pettit, T. Jackson, and P. Kircher, *J. Vac. Sci. Technol.* **19**, 626 (1981).
- [49] V. Darakchieva, M. Schubert, T. Hofmann, B. Monemar, C. L. Hsiao, T. W. Liu, L. C. Chen, W. J. Schaff, Y. Takagi, and Y. Nanishi, *Appl. Phys. Lett.* **95**, 202103 (2009).
- [50] E. Calleja, J. Grandal, M. A. Sánchez-García, M. Niebelschütz, V. Cimalla, and O. Ambacher, *Appl. Phys. Lett.* **90**, 262110 (2007).
- [51] T. D. Veal, P. H. Jefferson, L. F. J. Piper, C. F. McConville, T. B. Joyce, P. R. Chalker, L. Considine, H. Lu, and W. J. Schaff, *Appl. Phys. Lett.* **89**, 202110 (2006).
- [52] P. D. C. King, T. D. Veal, A. Adikimenakis, H. Lu, L. R. Bailey, E. Iliopoulos, A. Georgakilas, W. J. Schaff, and C. F. McConville, *Appl. Phys. Lett.* **92**, 172105 (2008).

## BIBLIOGRAPHY

---

- [53] V. Y. Aristov, V. M. Zhilin, C. Grupp, A. Taleb-Ibrahimi, H. J. Kim, P. S. Mangat, P. Soukiassian, and G. L. Lay, *Appl. Surf. Sci.* **166**, 263 (2000).
- [54] M. Noguchi, K. Hirakawa, and T. Ikoma, *Phys. Rev. Lett.* **66**, 2243 (1991).
- [55] H. Yamaguchi, J. L. Sudijono, B. A. Joyce, T. S. Jones, C. Gatzke, and R. A. Stradling, *Phys. Rev. B* **58**, R4219 (1998).
- [56] P. D. C. King, T. D. Veal, D. J. Payne, A. Bourlange, R. G. Egdell, and C. F. McConville, *Phys. Rev. Lett.* **101**, 116808 (2008).
- [57] D. Segev and C. G. Van de Walle, *Europhys. Lett.* **76** (2), 305 (2006).
- [58] T. D. Veal, L. F. J. Piper, M. R. Phillips, M. H. Zareie, H. Lu, W. J. Schaff, and C. F. McConville, *Phys. Stat. Sol. A* **204**, 536 (2007).
- [59] L. F. J. Piper, T. D. Veal, C. F. McConville, H. Lu, and W. J. Schaff, *Appl. Phys. Lett.* **88**, 252109 (2006).
- [60] H. Manasevit, *Appl. Phys. Lett.* **12**, 156 (1968).
- [61] <http://www.aixtron.com/>
- [62] <http://www.veeco.com/maxbright/>
- [63] G. B. Stringfellow, “Organometallic Vapor-Phase Epitaxy: Theory and Practice”, Academic Press, Inc., San Diego, California, (1989).
- [64] M. A. Herman and H. Sitter, “Molecular Beam Epitaxy”, Ed. M. B. Panish, “Springer Series in Materials Science”, Springer, New York, (1989).
- [65] K. W. Kolasinski, “Surface science: Foundations of Catalysis and Nanoscience”, 2<sup>nd</sup> Ed., Wiley & Son , p. 356 (2008).
- [66] N. I. Buchan and M. L. Yu, *Surf. Sci.* **280** 383 (1993).
- [67] N. I. Buchan, C. A. Larsen, G. B. Stringfellow, *J. Cryst. Growth* **92**, 591 (1988).
- [68] M. Volmer and A. Weber, *Z. Phys. Chem* **119**, 277 (1926).
- [69] F. C. Frank and J. H. van der Merwe, *Proc. R. Soc. London* **A**, 205 (1949).
- [70] J. N. Stranski and L. Krastanov, *Ber. Akad. Wiss. Wien* **146**, 797 (1938).
- [71] J. A. Venables, G. D. T. Spiller, and M. Hanbucken, *Rep. Prog. Phys.* **47**, 399 (1984).
- [72] S. S. Liu and D. A. Stevenson, *J. Electrochem. Soc.* **125**, 1161 (1978).
- [73] S. Nishide, T. Yoshimura, Y. Takamatsu, A. Ichige, K. Pak, N. Ohshima, and H. Yonezu, *J. Cryst. Growth* **189/190**, 325 (1998).

## BIBLIOGRAPHY

---

- [74] A. Koukitu, N. Takahashi, T. Taki, and H. Seki, *Jpn. J. Appl. Phys.* **35**, L673 (1996).
- [75] M. Mesrine, N. Grandjean, and J. Massies, *Appl. Phys. Lett.* **72**, 350 (1998).
- [76] D. F. Davidson, K. Kohse-hoinghaus, A. Y. Chang, and R. K. Hanson, *Int. J. Chem. Kinet.* **22**, 513 (1990).
- [77] R. M. Graham, A. C. Jones, N. J. Manson, S. Rushworth, A. Salesse, T. Y. Seong, G. Booker, L. Smith, and P. J. Walker, *Semi. Sci. Tech.* **8**, 1797 (1993).
- [78] S. Curioto and D. Chatain, *Surf. Sci* **603**, 2688 (2009).
- [79] H. G. Tompkins and E. A. Irene, “*Handbook of ellipsometry*”, William Andrew Pub., Springer (2005).
- [80] A. Kasic, E. Valcheva, B. Monemar, H. Lu, and W. J. Schaff, *Phys. Rev. B* **70**, 115217 (2004).
- [81] M. Losurdo, P. Capezzuto, G. Bruno, G. Namkoong, W. A. Doolittle, and A. S. Brown, *J. Appl. Phys.* **91**, 2508 (2002).
- [82] F. Dwikusuma and T. F. Kuech, *J. Appl. Phys.* **94**, 5656 (2003).
- [83] M. Drago, C. Werner, M. Pristovsek, U. W. Pohl, and W. Richter, *Phys. Stat. Solidi A* **203**, 1622(2006).
- [84] B. Ma, W. Hu, H. Miyake, and K. Hiramatsu, *App. Phys. Lett.* **95**, 121910 (2009).
- [85] N. Grandjean, J. Massies, and M. Leroux, *App. Phys. Lett.* **69**, 2071 (1996).
- [86] T. Yamaguchi, T. Araki, Y. Saito, K. Kano, H. Kanazawa, Y. Nanishi, N. Teraguchi, and A. Suzuki, *J. Cryst. Growth* **237**, 993 (2002).
- [87] A. Marmier and S. C. Parker, *Phys. Rev. B* **69**, 115409 (2004).
- [88] W. J. Wang, K. Sugita, Y. Nagai, Y. Houchin, A. Hashimoto, and A. Yamamoto, *Phys. Stat. Solidi C* **4**, 2415 (2007).
- [89] F. Liu, R. Collazo, S. Mita, Z. Sitar, G. Duscher, and S. J. Pennycook, *Appl. Phys. Lett.* **91**, 203115 (2007).
- [90] Y. Wang, X. L. Du, Z. X. Mei, Z. Q. Zeng, M. J. Ying, H. T. Yuan, J. F. Jia, Q. K. Xue, and Z. Zhang, *Appl. Phys. Lett.* **87**, 051901 (2005).
- [91] P. Vennégués and B. Beaumont, *Appl. Phys. Lett.* **75**, 4115 (1999).
- [92] M. Drago, “MOVPE growth of InN analyzed by in-situ spectroscopic ellipsometry”, *PhD Thesis*, Technical University of Berlin (2007).

- [93] T. Hashimoto, Y. Terakoshi, M. Ishida, M. Yuri, O. Imafuji, T. Sugino, A. Yoshikawa, and K. Itoh, *J. Cryst. Growth* **189/190** 254, (1998).
- [94] V. E. Henrich and P. A. Cox, “The Surface Science of Metal Oxides”, Cambridge University Press, New York, p. 53 (1994).
- [95] R. Di Felice and J. E. Northrup, *Appl. Phys. Lett.* **73**, 936 (1998).
- [96] L. Liu and J. H. Edgar, *Mater. Sci. and Eng. R* **37**, 61 (2002).
- [97] R. Collazo, S. Mita, A. Aleksov, R. Schlessler, and Z. Sitar, *J. Cryst. Growth* **287**, 586 (2005).
- [98] M. Takeuchi, H. Shimizu, R. Kajitani, K. Kawasaki, T. Kinoshita, K. Takada, H. Murakami, Y. Kumagai, A. Koukitu, T. Koyama, S. F. Chichibu, and Y. Aoyagi, *J. Cryst. Growth* **305**, 360 (2007).
- [99] C. J. Lua, X. F. Duan, H. Lu, and W. J. Schaff, *J. Mat. Res.* **21**, 1693 (2006).
- [100] T. Mitate, S. Mizuno, H. Takahata, R. Kakegawa, T. Matsuoka, and N. Kuwano, *Appl. Phys. Lett.* **86**, 134103 (2005).
- [101] D. Muto, T. Araki, H. Naoi, F. Matsuda, and Y. Nanishi, *Phys. Stat. Solidi A* **202**, 773 (2005).
- [102] H. Naoi, F. Matsuda, T. Araki, A. Suzuki, and Y. Nanishi, *J. Cryst. Growth*, **269**, 155 (2004).
- [103] Y. Hayakawa, D. Muto, H. Naoi, A. Suzuki, T. Araki, and Y. Nanishi, *Jpn. J. Appl. Phys.* **45**, L384 (2006).
- [104] T. D. Veal, P. D. C. King, P. H. Jefferson, L. F. J. Piper, and C. F. McConville, *Phys. Rev. B* **76**, 075313 (2007).
- [105] D. Briggs and J. T. Grant, “Surface Analysis by Auger and X-Ray Photoelectron Spectroscopy”, IMPublications (2003).
- [106] F. Bechstedt, F. Fuchs, and J. Furthmüller, *Phys. Stat. Solidi A* **207**, 1041 (2010).
- [107] L. Ley, R. A. Pollak, F. R. McFeely, S. P. Kowalczyk, and D. A. Shirley, *Phys. Rev. B* **9**, 600 (1974).
- [108] R. Di Felice and J. E. Northrup, *Appl. Phys. Lett.* **73**, 936 (1998).
- [109] J. E. Northrup, R. Di Felice, and J. Neugebauer, *Phys. Rev. B* **55**, 13878 (1997).
- [110] V. Yu. Davydov and A. A. Klochikhin, *Semiconductors* **38**, 861 (2004).
- [111] N. Wiesera, M. Klosea, R. Dassowa, F. Scholzb, and J. Off, *J. Cryst. Growth* **189/190**, 661 (1998).

## BIBLIOGRAPHY

---

- [112] V. Darakchieva, P. P. Paskov, E. Valcheva, T. Paskova, B. Monemar, M. Schubert, H. Lu, and W. J. Schaff, [Appl. Phys. Lett.](#) **84**, 3636 (2004).
- [113] G. Kaczmarczyk, A. Kaschner, S. Reich, A. Hoffmann, C. Thomsen, D. J. As, A. P. Lima, D. Schikora, K. Lischka, R. Averbeck, and H. Riechert, [Appl. Phys. Lett.](#) **76**, 2122 (2000).
- [114] C. Piquier, F. Demangeot, J. Frandon, O. Briot, B. Maleyre, S. Ruffenach, B. Gil, J. Pomeroy, M. Kuball, H. Hubel, N. van Uden, and D. Dunstan, [Superlattices and Microstructures](#) **36**, 581 (2004).
- [115] K. Kim, W. R. L. Lambrecht, and B. Segall, [Phys. Rev. B](#) **53**, 16310 (1996).
- [116] T. Hino, S. Tomiya, T. Miyajima, K. Yanashima, S. Hashimoto, and M. Ikeda, [Appl. Phys. Lett.](#) **76**, 3421 (2000).
- [117] A. Jain, X. Weng, S. Raghavan, B. L. VanMil, T. Myers, and J. M. Redwing, [J. Appl. Phys.](#) **104**, 053112 (2008).
- [118] C. Meissner, S. Ploch, M. Pristovsek, and M. Kneissl, [Phys. Stat. Solidi C](#) **6**, S545 (2009).
- [119] T. Zywietz, J. Neugebauer, and M. Scheffler, [Appl. Phys. Lett.](#) **73**, 487 (1998).
- [120] L. Lymperakis and J. Neugebauer, [Phys. Rev. B](#) **79**, 241308(R) (2009).
- [121] A. Aliano, A. Catellani, and G. Cicero, [Appl. Phys. Lett.](#) **99**, 193106 (2011).
- [122] V. A. Vilkotskhii, D. S. Domanevskii, R. D. Kakanakov, V. V. Krasovskii, V. D. Tkachev, [Phys. Stat. Solidi B](#) **91**, 71 (1979).
- [123] N. R. Yogamalar and A. C. Bose, [Appl. Phys. A](#), **103**, 33 (2011).
- [124] C. H. Swartz, R. P. Tompkins, N. C. Giles, T. H. Meyers, H. Lu, W. J. Schaff, and L. F. Eastman, [J. Cryst. Growth](#) **269**, 29 (2004).
- [125] N. Ma, X. Q. Wang, S. T. Liu, L. Feng, G. Chen, F. J. Xu, N. Tang, L. W. Lu, and B. Shen, [Appl. Phys. Lett.](#) **99**, 182107 (2011).
- [126] T. L. Tansley and R. J. Egan, [Phys. Rev. B](#) **45**, 10942 (1992).
- [127] S. Ruffenach, M. Moret, O. Briot, and B. Gil, [App. Phys. Lett.](#) **95**, 042102 (2009).
- [128] V. Darakchieva, K. Lorenz, M. Y. Xie, E. Alves, C. L. Hsiao, L. C. Chen, L. W. Tu, W. J. Schaff, T. Yamaguchi, and Y. Nanishi, [J. Appl. Phys.](#) **110**, 063535 (2011).
- [129] G. Pettinari, F. Masia, M. Capizzi, A. Polimeni, M. Losurdo, G. Bruno, T. H. Kim, S. Choi, A. Brown, V. Lebedev, V. Cimalla, and O. Ambacher, [Phys. Rev. B](#) **77**, 125207 (2008).

- [130] M. Moret, S. Ruffenach, O. Briot, and B. Gil, *Appl. Phys. Lett.* **95**, 031910 (2009).
- [131] C. P. Kuo, S. K. Vong, R. M. Cohen, and G. B. Stringfellow, *J. Appl. Phys.* **57**, 5428 (1985).
- [132] B. V. Zeghbroeck, “Principles of semiconductor devices and heterojunctions”, Prentice Hall (2009).
- [133] T. V. Shubina, S. V. Ivanov, V. N. Jmerik, D. D. Solnyshkov, V. A. Vekshin, P. S. Kopév, A. Vasson, J. Leymarie, A. Kavokin, H. Amano, K. Shimono, A. Kasic, and B. Monemar, *Phys. Rev. Lett.* **92**, 117407 (2004).
- [134] S. Z. Wang, S. F. Son, Y. X. Xia, and S. W. Xie, *J. Appl. Phys.* **95**, 7998 (2004).
- [135] D. N. Zakharov, Z. Liliental-Weber, B. Wagner, Z. J. Reitmeier, E. A. Preble, and R. F. Davis, *Phys. Rev. B* **71**, 235334 (2005).
- [136] J. Smalc-Koziorowska, G. Tsiakatouras, A. Lotsari, A. Georgakilas, and G. P. Dimitrakopoulos, *J. Appl. Phys.* **107**, 073525 (2010).
- [137] Y. A. R. Dasilva, M. P. Chauvat, P. Ruterana, L. Lahourcade, E. Monroy, and G. Nataf, *J. Phys.: Condens. Matter* **22**, 355802 (2010).
- [138] G. P. Dimitrakopoulos, *J. Phys.: Conf. Ser.* **281**, 012012 (2011).
- [139] F. Wu, A. Tyagi, E. C. Young, A. E. Romanov, K. Fujito, S. P. DenBaars, S. Nakamura, and J. S. Speck, *J. Appl. Phys.* **109**, 033505 (2011).
- [140] B. W. Dodson, D. R. Myers, A. K. Datye, V. S. Kaushik, D. L. Kendall, and B. Martinez-Tovar, *Phys. Rev. Lett.* **61**, 2681 (1988).
- [141] H. Nagai, *J. Appl. Phys.* **45**, 3789 (1974).
- [142] M. A. Moram and M. E. Vickers, *Rep. Prog. Phys.* **72**, 036502 (2009).
- [143] T. Wernicke, C. Netzel, M. Weyers, and M. Kneissl, *Phys. Stat. Solidi C* **5**, 1815 (2008).
- [144] S. Ploch, M. Frentrup, T. Wernicke, M. Pristovsek, M. Weyers, and M. Kneissl, *J. Cryst. Growth* **312**, 2171 (2010).
- [145] M. Frentrup, S. Ploch, M. Pristovsek, and M. Kneissl, *Phys. Stat. Solidi B* **248**, 583 (2011).
- [146] H. C. Cho, M. Suematsu, H. Murakami, Y. Kumagai, R. Tob, and A. Koukitu, *Phys. Stat. Solidi C* **8**, 2025 (2011).
- [147] H. Murakami, H. C. Cho, M. Suematsu, K. Inaba, Y. Kumagai, and A. Koukitu, *Phys. Stat. Solidi C*, **9** 677 (2012).

## BIBLIOGRAPHY

---

- [148] G. Koblmüller, C. S. Gallinat, and J. S. Speck, *J. Appl. Phys.* **101**, 083516 (2007).
- [149] C. S. Gallinat, G. Koblmüller, J. S. Brown, and J. S. Speck, *J. Appl. Phys.* **102**, 064907 (2007).
- [150] K. Shiraishi, *Appl. Phys. Lett.* **60**, 1363 (1992).
- [151] T. Zywiets, J. Neugebauer, and M. Scheffler, *Appl. Phys. Lett.* **73**, 487 (1998).
- [152] N. Takeuchi, A. Selloni, T. H. Myers, and A. Doolittle, *Phys. Rev. B* **72**, 115307 (2005).
- [153] M. Moret, S. Ruffenach, O. Briot, and B. Gil, *Phys. Stat. Solidi A* **207**, 24 (2010).
- [154] G. Koblmüller, A. Hirai, F. Wu, C. S. Gallinat, G. D. Metcalfe, H. Shen, M. Wraback, and J. S. Speck, *Appl. Phys. Lett.* **93**, 171902 (2008).
- [155] R. Liu, A. Bell, F. A. Ponce, C. Q. Chen, J. W. Yang, and M. A. Khan, *Appl. Phys. Lett.* **86**, 021908 (2005).
- [156] S. Ploch, J. B. Park, J. Stellmach, T. Schwaner, M. Frentrup, T. Niermann, T. Wernicke, M. Pristovsek, M. Lehmann, and M. Kneissl, *J. Cryst. Growth* **331**, 25 (2011).
- [157] See <http://www.laytec.de/> for LayTec AnalysR version 5.27.
- [158] C. Cobet, “Linear optical properties of III-nitride semiconductors between 3 and 30 eV”, *PhD thesis*, Technical University of Berlin (2005).
- [159] P. Schley, J. Räthel, E. Sakalauskas, G. Gobsch, M. Wieneke, J. Bläsing, A. Krost, G. Koblmüller, J. S. Speck, and R. Goldhahn, *Phys. Status Solidi A* **207**, 1062 (2010).
- [160] T. Wernicke, C. Netzel, M. Weyers, and M. Kneissl, *Phys. Status Solidi C* **5**, 1815 (2008).
- [161] S. Ploch, J. B. Park, J. Stellmach, T. Schwaner, M. Frentrup, T. Niermann, T. Wernicke, M. Pristovsek, M. Lehmann, and M. Kneissl, *J. Cryst. Growth* **331**, 25 (2011).
- [162] D. V. Dinh, M. Pristovsek, R. Kremzow, and M. Kneissl, *Phys. Status Solidi RRL* **4**, 127 (2010).
- [163] M. Moret, S. Ruffenach, O. Briot, and B. Gil, *Phys. Status Solidi A* **208**, 1183 (2010).
- [164] A. Tyagi, F. Wu, E. C. Young, A. Chakraborty, H. Ohta, R. Bhat, K. Fujito, S. P. DenBaars, S. Nakamura, and J. S. Speck, *Appl. Phys. Lett.* **95**, 251905 (2009).

- [165] E. C. Young, F. Wu, A. E. Romanov, A. Tyagi, C. S. Gallinat, S. P. DenBaars, S. Nakamura, and J. S. Speck, *Appl. Phys. Exp.* **3**, 011004 (2010).
- [166] A. E. Romanov, E. C. Young, F. Wu, A. Tyagi, C. S. Gallinat, S. Nakamura, S. P. DenBaars, and J. S. Speck, *J. Appl. Phys.* **109**, 103522 (2011).
- [167] M. A. Moram and M. E. Vickers, *Rep. Prog. Phys.* **72**, 036502 (2009).
- [168] M. A. Moram, C. F. Johnston, J. L. Hollander, M. J. Kappers, and C. J. Humphreys, *J. Appl. Phys.* **105**, 113501 (2009).
- [169] S. Ploch, T. Wernicke, D. V. Dinh, M. Pristovsek, and M. Kneissl, *J. Appl. Phys.* **111**, 033526 (2012).
- [170] D. V. Dinh, M. Pristovsek, S. Solopow, D. Skuridina, and M. Kneissl, *Phys. Status Solidi C* **9**, 977 (2012).
- [171] J. E. Northrup, *Appl. Phys. Lett.* **95**, 133107 (2009).
- [172] A. Das, S. Magalhães, Y. Kotsar, P. K. Kandaswamy, B. Gayral, K. Lorenz, E. Alves, P. Ruterana, and E. Monroy, *Appl. Phys. Lett.* **96**, 181907 (2010).
- [173] G. Koblmüller, G. D. Metcalfe, M. Wraback, F. Wu, C. S. Gallinat, and J. S. Speck, *Appl. Phys. Lett.* **94**, 091905 (2009).
- [174] G. Koblmüller, A. Hirai, F. Wu, C. S. Gallinat, G. D. Metcalfe, H. Shen, M. Wraback, and J. S. Speck, *Appl. Phys. Lett.* **93**, 171902 (2008).
- [175] F. Ivaldi, C. Meissner, J. Domagala, S. Kret, M. Pristovsek, M. Högele, and M. Kneissl, *Jpn. J. Appl. Phys.* **50**, 031004 (2011).
- [176] P. D. C. King, T. D. Veal, and C. F. McConville, *Phys. Rev. B* **77**, 115213 (2008).
- [177] K. Wang, C. Lian, N. Su, and D. Jena, *Appl. Phys. Lett.* **91**, 232117 (2007).
- [178] R. Zhang, P. Zhang, T. Kang, H. Fan, X. Liu, *Appl. Phys. Lett.* **91**, 162104 (2007).
- [179] S. A. Chambers, T. Droubay, T. C. Kaspar, and M. Gutowski, *J. Vac. Sci. Technol. B* **22**, 2205 (2004).
- [180] P. D. C. King, T. D. Veal, and C. F. McConville, *Appl. Phys. Lett.* **91**, 092101 (2007).
- [181] C. G. Van de Walle and D. Segev, *J. Appl. Phys.* **101**, 081704 (2007).
- [182] D. Segev and C. G. Van de Walle, *J. Cryst. Growth* **300**, 199 (2007).
- [183] I. Mahboob, T. D. Veal, C. F. McConville, H. Lu, and W. J. Schaff, *Phys. Rev. Lett.* **92**, 036804 (2004).

## BIBLIOGRAPHY

---

- [184] S. Sonoda, *J. Phys.: Condens. Matter* **20**, 475201 (2008).
- [185] P. Kempisty, P. Strak, S. Krukowski, *Surf. Sci.* **605**, 695 (2011).
- [186] M. Silver, W. Batty, A. Ghiti, and E. P. O'Reilly, *Phys. Rev. B* **46**, 6781 (1992).
- [187] L. Vegard, *Z. Phys.* **5**, 17 (1921); *Z. Kristallogr.* **67**, 239 (1928).
- [188] A. R. Denton and N. W. Ashcroft, *Phys. Lett. A* **43**, 3161 (1991).
- [189] A. B. Chen and A. Sher, "Semiconductor alloys: physics and materials engineering", Plenum Press, New York, p. 68 (1995).
- [190] C. Caetano, L. K. Teles, M. Marques, A. Dal Pino Jr., and L. G. Ferreira, *Phys. Rev. B* **74**, 045215 (2006).
- [191] B. D. Cullity and S. R. Stock, "Elements of X-Ray Diffraction", 3<sup>rd</sup> Ed., Prentice-Hall Inc., p. 167-171 (2001).
- [192] E. Dimakis, E. Iliopoulos, K. Tsagaraki, Th. Kehagias, Ph. Komninou, and A. Georgakilas, *J. Appl. Phys.* **97**, 113520 (2005).
- [193] F. K. Yam and Z. Hassan, *Superlattices Microstruct.* **43**, 1 (2007).